Institute for Plasma Focus Studies

Melbourne, Kuala Lumpur, Singapore

Study of Plasma Focus

Enhancing Knowledge and Applications Potential

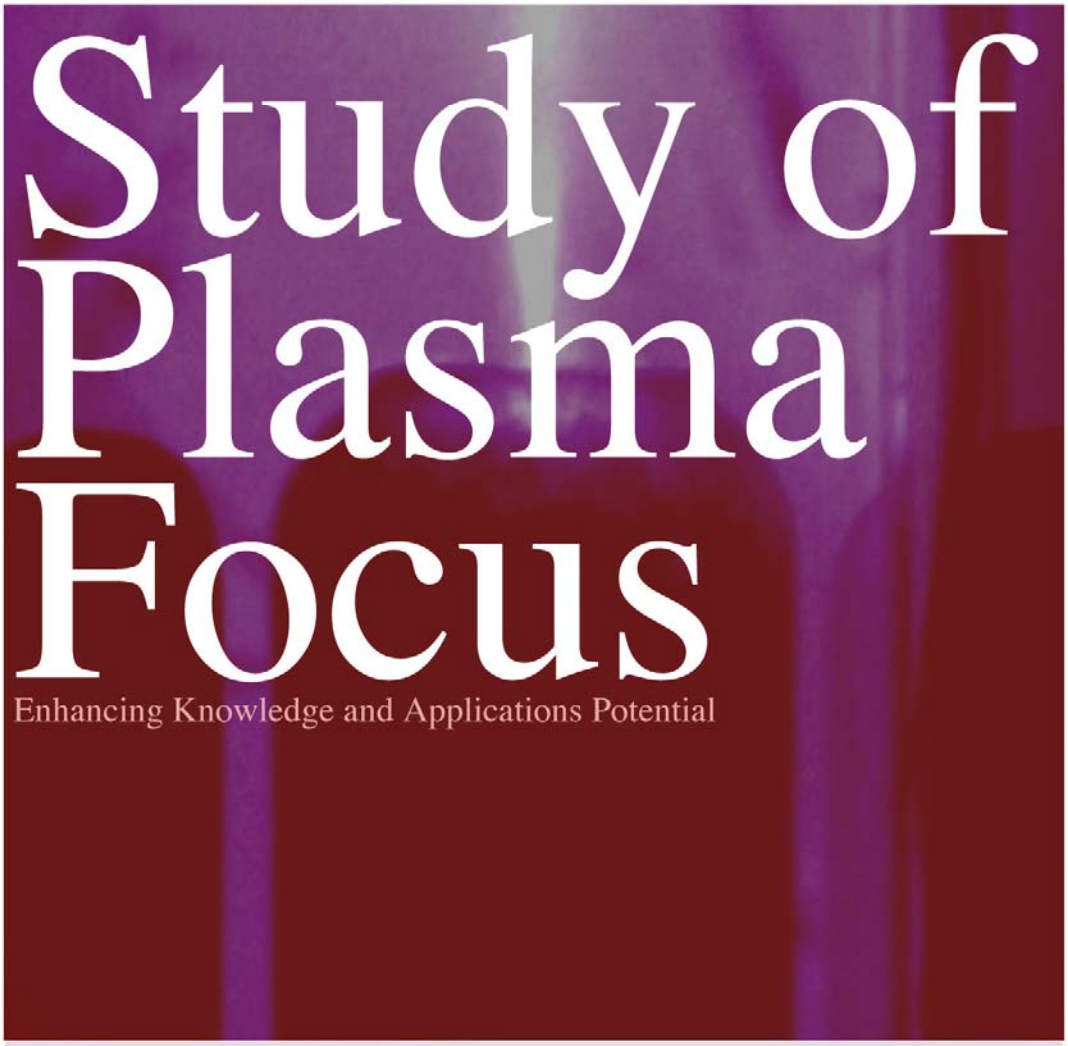

Bangkok, Thailand

30 March to 1 April 2012

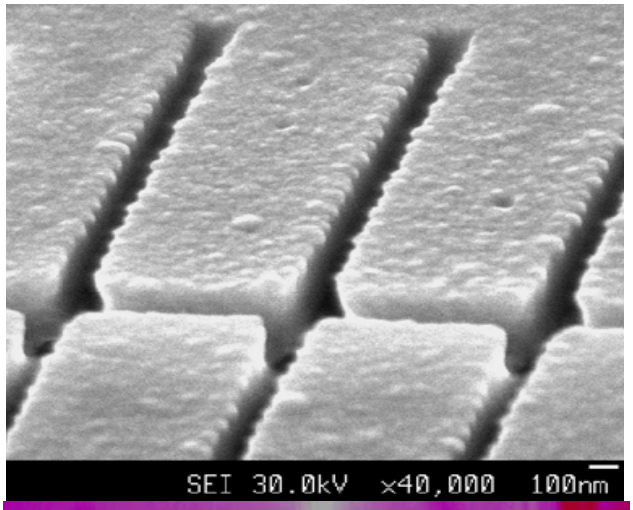
SEI 30.0kV x40,000 100nm

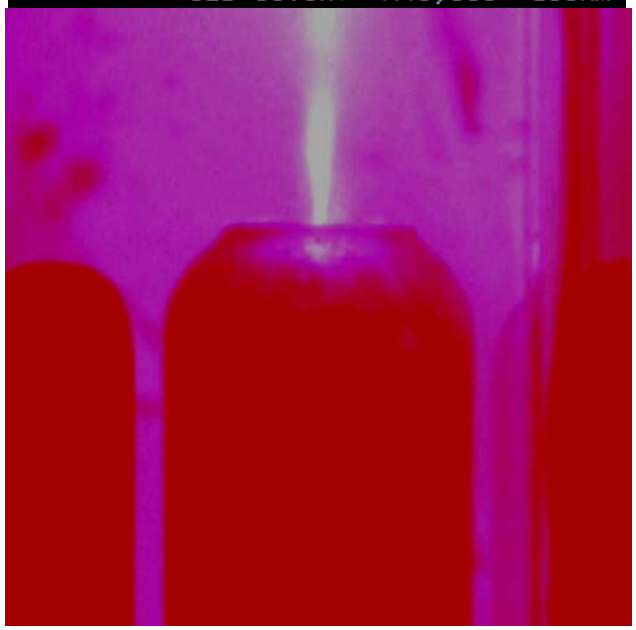

The Proceedings

Papers for the IPFS Conference

Opening Paper

From Electric Birth to Streaming Death of the Plasma Focus Knowledge and Applications

S LEE
Institute for Plasma Focus Studies, 32 Oakpark Drive, Chadstone, VIC 3148, Australia

e-mail: leesing@optusnet.com.au

Abstract
The plasma focus is a copious source of multiple radiation and highly energetic particles: hard and soft x-rays, electromagnetic radiation, fusion neutrons, relativistic electron beams, fast ion beams and highly energetic plasma streams with shock fronts exceeding Mach 1000. All these complex interactive radiation and particle streams are generated from a device which typically could be table-top located. It is a triumph of modern science and technology that we can now present a complete picture of the plasma focus in the lifetime of its dynamic evolution. That lifetime typically occupies all of 10 microseconds; from the time a spark starts the electric current which rises to 100 kA within a microsecond, driving a shock wave to Mach 100 straight down the fairway; to the radial compression phase when increasing electromagnetic forces doubles the speed of the hot plasma shock waves; before the final focusing action; squeezing the plasma into a superheated highly dense 'pinch' with temperatures exceeding that of the centre of the sun. From this minute cauldron of 'solar' 'stellar' matter comes forth the rich explosion of multiple radiation and energetic particles and beams. In a typical device this tremendous explosion lasts less than 0.1 microsecond. This introduction will use sequences of detailed nanosecond-exposure pictures to show the evolution of the plasma pinch, conveying the idea of the very high speeds and hence high temperatures involved. Although detailed knowledge of many specific areas within the lifetime of the plasma focus is still lacking so that the microscopic view in many areas need to be filled in; yet from the mid-distance there is a satisfactory picture of the whole processes linking the plasma focus as it evolves from stage to stage. Particularly exciting are the many applications that have been demonstrated using the multiple radiation and energetic particles for micro-lithography, micro-machining, advanced materials manipulation and fabrication down to nano-levels. Work is on-going for materials interrogation and identification with security implications; and generation of complex radiation and particle pulses of relevance to nuclear fusion reactors. Numerical experiments gain valuable insights that guide future developments and applications, suggesting new devices for compression and yield enhancements. An integrated hardware and numerical experiment package can also be profitably developed to train manpower and generate applications for the dawning of the Fusion Age.

1. Introduction

The Plasma Focus is a compact powerful pulsed source of multi-radiation [1]. Even a small table-top sized 3 kJ plasma focus produces an intense burst of radiation with extremely high powers. For example when operated in neon, the x-ray emission power peaks at 10^9 W over a period of nanoseconds. When operated in deuterium the neutron burst produces rates of neutron typically 10^{15} neutrons per second over burst durations of tens of nanosecond. The emission comes from a point source making these devices among the most powerful laboratory pulsed radiation sources in the world. These sources are plasma-based.

When matter is heated to a high enough temperature, it ionizes and becomes plasma. It emits electromagnetic radiation. The spectrum depends on the temperature and the material. The higher the temperature and the denser the matter, the more intense is the radiation. Beams of electrons and ions may also be emitted. If the material is deuterium, nuclear fusion may take place if the density and temperature are high enough. In that case neutrons are also emitted. Typically the temperatures are above several million K and compressed densities above atmospheric density starting with a gas a hundredth of an atmospheric density.

One way of achieving such highly heated material is by means of an electrical discharge through gases. As the gas is heated, it expands, lowering the density and making it difficult to heat further. Thus it is necessary to compress the gas whilst heating it, in order to achieve sufficiently intense conditions. An electrical discharge between two electrodes produces a constricting magnetic field which pinches the column. In order to 'pinch', or hold together, a column of gas at about atmospheric density at a temperature of 1 million K, a rather large pressure has to be exerted by the pinching magnetic field. Thus an electric current of at least hundreds of kA are required even for a column of small radius of say 1 mm. Moreover the dynamic process requires that the current rises very rapidly, typically in under 0.1 μs in order to have a sufficiently hot and dense pinch. Such a pinch is known as a super-fast super-dense pinch; and requires special MA fast-rise (ns) pulsed-lines. These lines may be powered by capacitor banks, and suffer the disadvantage of conversion losses and high cost due to the high technology pulse-shaping line, in addition to the capacitor banks.

A superior method of producing the super-dense and super-hot pinch is to use the plasma focus. Not only does this device produce superior densities and temperatures, moreover its method of operation does away with the extra layer of technology required by the expensive and inefficient pulse-shaping line. A simple capacitor discharge is sufficient to power the plasma focus.

2 The plasma focus

The plasma focus is divided into two sections. The first is a pre-pinch (axial) section. The function of this section is primarily to delay the pinch until the capacitor discharge (rising in a damped sinusoidal fashion) approaches its maximum current. This is done by driving a current sheet down an axial (acceleration) section until the capacitor current approaches its peak. Then the current sheet is allowed to undergo transition into a radial compression phase. Thus the pinch starts and occurs at the top of the current pulse. This is equivalent to driving the pinch with a super-fast rising current; without necessitating the fast line technology. Moreover the intensity which is achieved is superior to the line driven pinch.

The two-phase mechanism of the plasma focus [2] is depicted in Fig 1. The inner electrode (anode) is separated from the outer concentric cathode by an insulating backwall (see

Fig 2). The electrodes are enclosed in a chamber, evacuated and typically filled with gas at about 1/100 of atmospheric pressure. When the capacitor voltage is switched onto the tube, breakdown

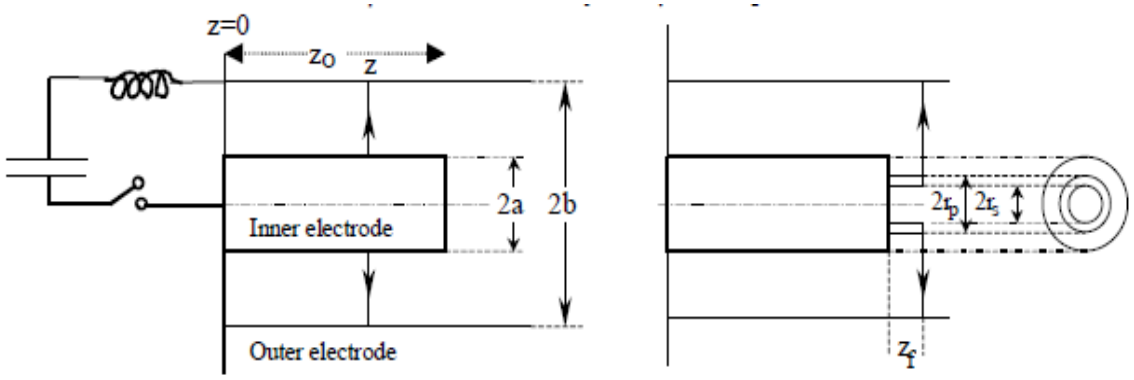

Fig 1. Schematic of the axial and radial phases. The left section depicts the axial phase, the right section the radial phase. In the left section, z is the effective position of the current sheath-shock front structure. In the right section r_s is the position of the inward moving shock front driven by the piston at position r_p. Between r_s and r_p is the radially imploding slug, elongating with a length z_f. The capacitor, static inductance and switch powering the plasma focus is shown for the axial phase schematic only.

occurs axisymmetrically between the anode and cathode across the backwall. The 'sheet' of current lifts off the backwall as the current rises to a sufficient value.

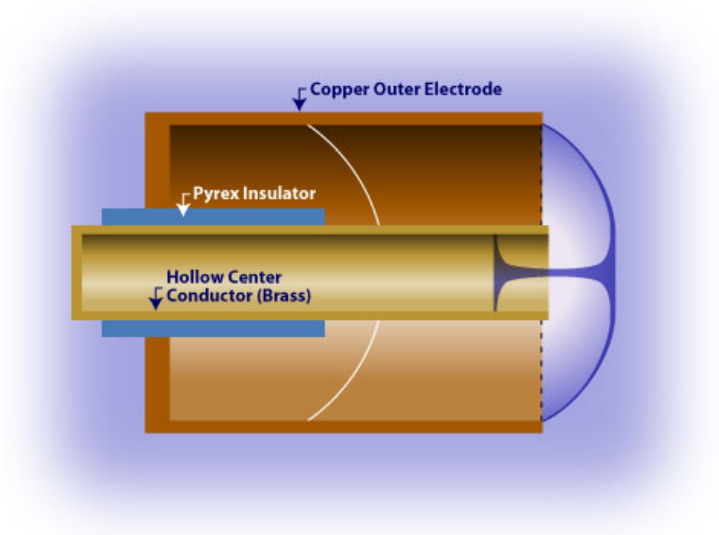

Fig 2. Dense plasma focus device. Image from Glenn Millam. Source: Focus Fusion Society [3]

Axial phase: The self-magnetic force of the current then pushes the current sheet, accelerating it supersonically down the tube. This is very similar to the mechanism of a linear motor. The speed of the current sheet, the length of the tube and the rise time of the capacitor discharge are matched so that the current sheet reaches the end of the axial section just as the discharge reaches its peak value. This phase typically lasts 1-3 μs for a plasma focus of several kJ.

Radial Phase: The part of the current sheet in sliding contact with the anode then 'slips' off the end 'face' of the anode forming a cylinder of current, which is then pinched inwards. Imploding inwards at higher and higher speeds, the shock front coalesces on-axis and a super-dense, super-hot plasma column is pinched onto the axis (see Fig 2). This column stays super-hot and super-dense for typically ten ns for a small focus. The column then breaks up and explodes. For a small plasma focus of several kJ, the most intense emission phase lasts for the order of several ns. The radiation source is spot-like (1mm diameter) when viewed end-on.

3. The Pinch phase of the plasma focus

3.1 A filtered photo of the million K pinch

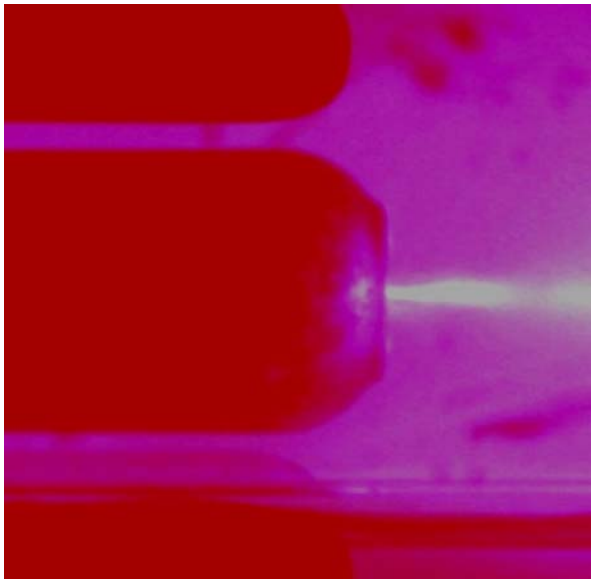

Fig 3. A still photo of the million C plasma pinch produced in the INTI PF (taken by Paul Lee) Using suitably chosen filters, the most intense optical radiation is shown, which turns out to be the pinch; all other phases of dynamics, being less optically intense, are filtered away.

Fig 3 shows a photograph of the INTI PF [4,5] pinch taken with an ordinary digital camera. The long-exposure allows light from all the phases of the PF device to be incident on the recording CCD. But the combination of filters allows only the brightest part of the discharge dynamics to be shown; hence the pinch (the brightest part of the column) is recorded. The more diffuse part of the column at the right edge of the photo is the post-pinch plasma stream.

3.2 Nanosecond shadowgraphs of the plasma focus pinch and post-pinch

To capture time-resolved images of the focus pinch an exposure time of 1 ns is necessary to freeze the motion to less than 0.3 mm (since the highest speed of the current sheet is expected to be around 30 cm/μs (or 0.3 mm/ns). A collimated laser beam with an exposure time of 1 ns is shone through the plasma focus (side-on) and the shadow of the moving plasma is cast onto a recording CCD. The plasma self light is filtered away. The time of the laser pulse is adjustable. A composite sequence of shots is obtained [6] as shown in Fig 4. The time of the image is

recorded on top of the image with t=0 being the time when the plasma focus pinch is judged to be at its most compressed state.

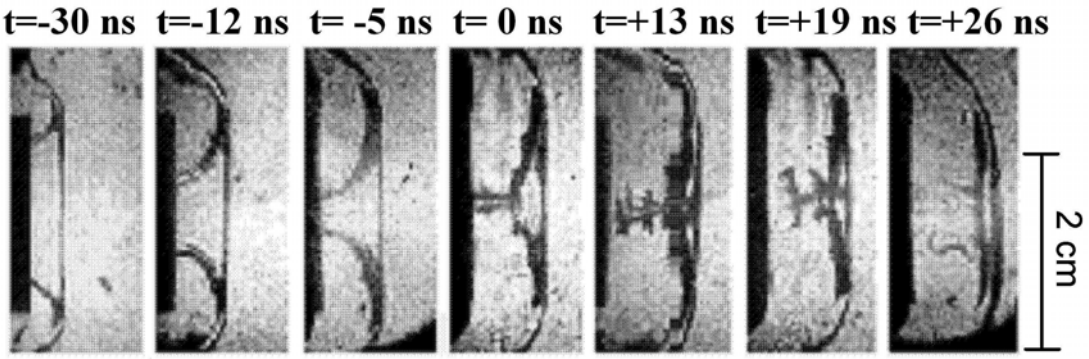

Fig 4. A composite sequence [6] of the radial implosion dynamics of the plasma focus (anode shown pointing sideways- left to right)

From this sequence the average speed of implosion from a=8mm (t=-30 ns) to a~0.5 mm (t=0) is found to be 0.25 mm/ns or 25 cm//μs. The peak speed is more as the current sheet is accelerating as it speeds inwards. Taking the speed of 25 cm/μs, due to the equipartition of energy in a shock the on-axis temperature is immediately found to be 1.5×10^6K; and on shock reflection, all the kinetic energy is stagnated causing the column to reach a temperature of 3×10^6K. The instability break-up of the column is seen in the last 3 frames.

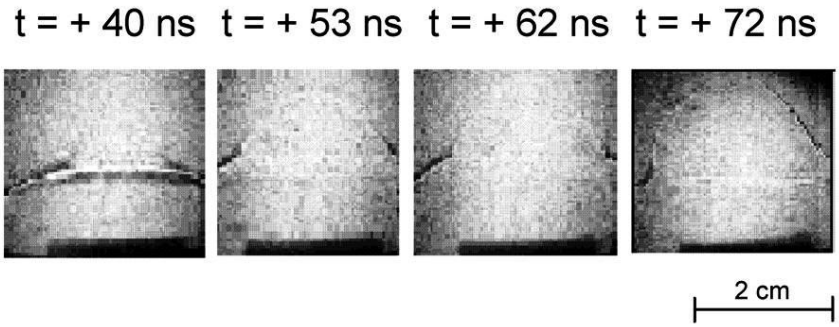

Fig 5. A sequence showing post focus axial shock waves blown out from the pinch [6] (anode shown pointing up)

In Fig. 5 the anode is shown pointing upwards (whereas in Fig 4 the anode is pointing left to right). The sequence [6] follows that of the inward implosion and instability break-up of the pinch. This post-focus sequence shows that 14 ns after the break-up (shown in the sequence of Fig 4) a fast shock wave is shot out from the focus region traversing 9 mm in 22 ns or 40 cm/μs.

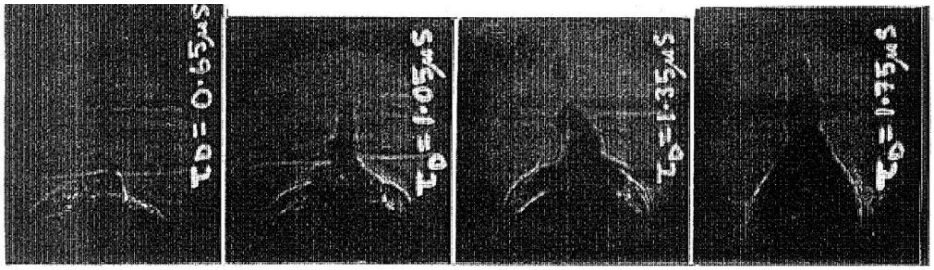

Fig 6 Composite sequence [7] showing anode-sputtered copper plasma jet occurring at a later time (anode shown pointing up)

Fig 6 shows a sequence of shadowgraphs taken at a much later time from 0.65 μs (t=+650 ns) to 1.75 μs. Measurements [7] show that this copper jet comes from material sputtered from the anode by the electron beam. This copper jet travels much more slowly at 2 cm/μs containing ¼ mg of copper carrying 50 J of kinetic energy

The radiations from the plasma focus are produced for the 3 kJ PF from -5ns to +26 ns (Fig 4). First the soft x-rays which is characteristic of the gas (particularly in gases from nitrogen upwards in atomic number) start to be emitted just before t=0; the ion beams emitted in a downstream direction and the electron beam in the opposite direction towards the anode; and the neutrons (from deuterium pinches) are emitted just after t=0; as are the hard x-rays. The high speed axial shock waves (Fig 5) carrying considerable energy and the associated post-pinch plasma streaming and then the slower jet from anode sputtered materials (see Fig 6) constitute the final products of the plasma focus phenomenon. The use and control of these 'streaming death' products are proving of importance for plasma focus materials modification, fabrication and deposition as thin films.

3.3 From electrical birth to streaming death of the Plasma Focus

The above images reveal detailed dynamics of the radial phases of the 3 kJ plasma focus, from the compression to the pinch and instability break-up to the subsequent fast plasma streaming, these processes taking just over 100 ns extending another microsecond or so to the anode-sputtered copper jet. Many other diagnostics are used to find more information for all the phases of the plasma focus. At the same time a comprehensive and complete numerical experiment code is available to be configured to run as any plasma focus in the world. This code [8] needs only one measurement from the selected plasma focus namely the current waveform. With this current waveform fitted to the computed waveform the code outputs all the dynamics from axial to radial phase and pinch phase giving speeds, times and dimensions of the pinch, condition of the plasma, radiation and neutron yields, and the numbers and energetics of the ion beam, electron beams, post-pinch fast plasma stream and the anode-sputtered copper jet. An example is shown in Fig 7 of the simplest measurement requiring only a current coil. All the information of that plasma focus shot – from electrical birth (start of axial phase) through the pinch (end of radial phase) to the streaming death- is contained in the current waveform and to some extent in the voltage waveform, also shown in Fig 7.

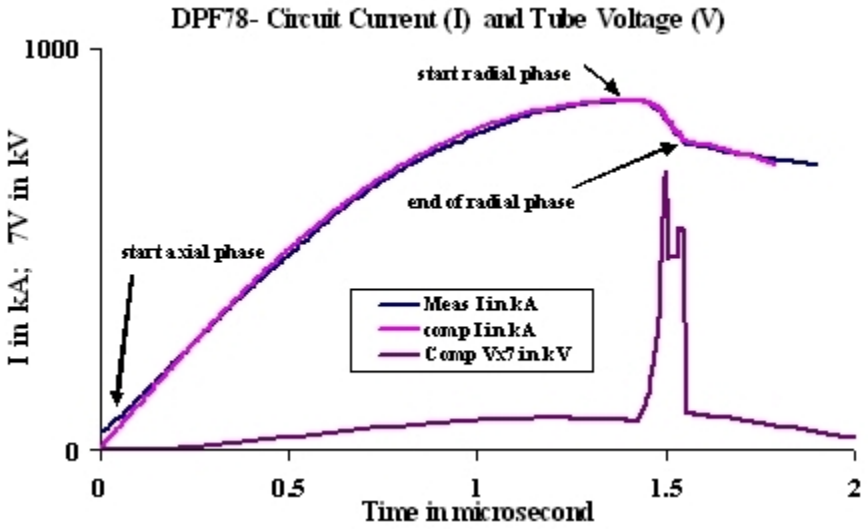

Fig 7 Computed current waveform fitted to the measured current waveform. Indicated on the current trace are the start and end of axial phase, start and end of radial phase. This fitting of the computed current calibrates the code configured as the DPF78 for this figure. The code then outputs realistic dynamics, lifetime and dimensions of the pinch and yields and energetics for this shot.

4. Research towards applications

The small group of plasma focus experts gathered here today to review the research conducted in our institutions have researched on the following applications to various levels of success. The list is not exhaustive but is a useful guide. More details will be added as our conference proceeds.

1. Microelectronics lithography towards nano-scale using focus SXR, EUV and electrons
2. Micro-machining
3. Surface modification and alloying, deposition of advanced materials: superconducting films, fullerenes, DLC films, TiN, ZrAlON, nanostructured magnetic CoPt thin films
4. Surface damage for materials testing in high-radiation and energy flux environment
5. Diagnostic systems of commercial/industrial value: CCD-based imaging, multi-frame ns laser shadowgraphy, pin-hole and aperture coded imaging systems, neutron detectors, diamond and diode x-ray spectrometer, vacuum uv spectrometer, ccd-based electron energy analyser, Faraday cups, mega-amp current measurement, pulsed magnetic field measurement, templated SXR spectrometry, water-window radiation for biological applications; neutron activation and gamma ray spectroscopy'
6. Pulsed power technology; capacitor discharge, Pulsed power for plasma, optical and lighting systems, triggering technology, repetitive systems, circuit manipulation technology such as current-steps for enhancing performance and compressions; powerful multi-radiation sources with applications in materials and medical applications
7. Plasma focus design; complete package integrating hardware, diagnostics and software.
8. Fusion technology and fusion education, related to plasma focus training courses

5 Conclusion: Presenting some products

5.1 Micro-lithography and micro-machining towards nano-scale

Fig 8 shows the NX2 (2 kJ, 400 kA, 16 shots per second, 300 W neon SXR per shot, 10 minute burst duration) in its original set-up for micro-lithography. Fig 8(a) is a schematic of the 1-tonne (1.4 m high) structure with the focus chamber surrounded by the capacitor bank and raised above the ground on pillars made up of ALE chargers, gas distributors and trigger sub-

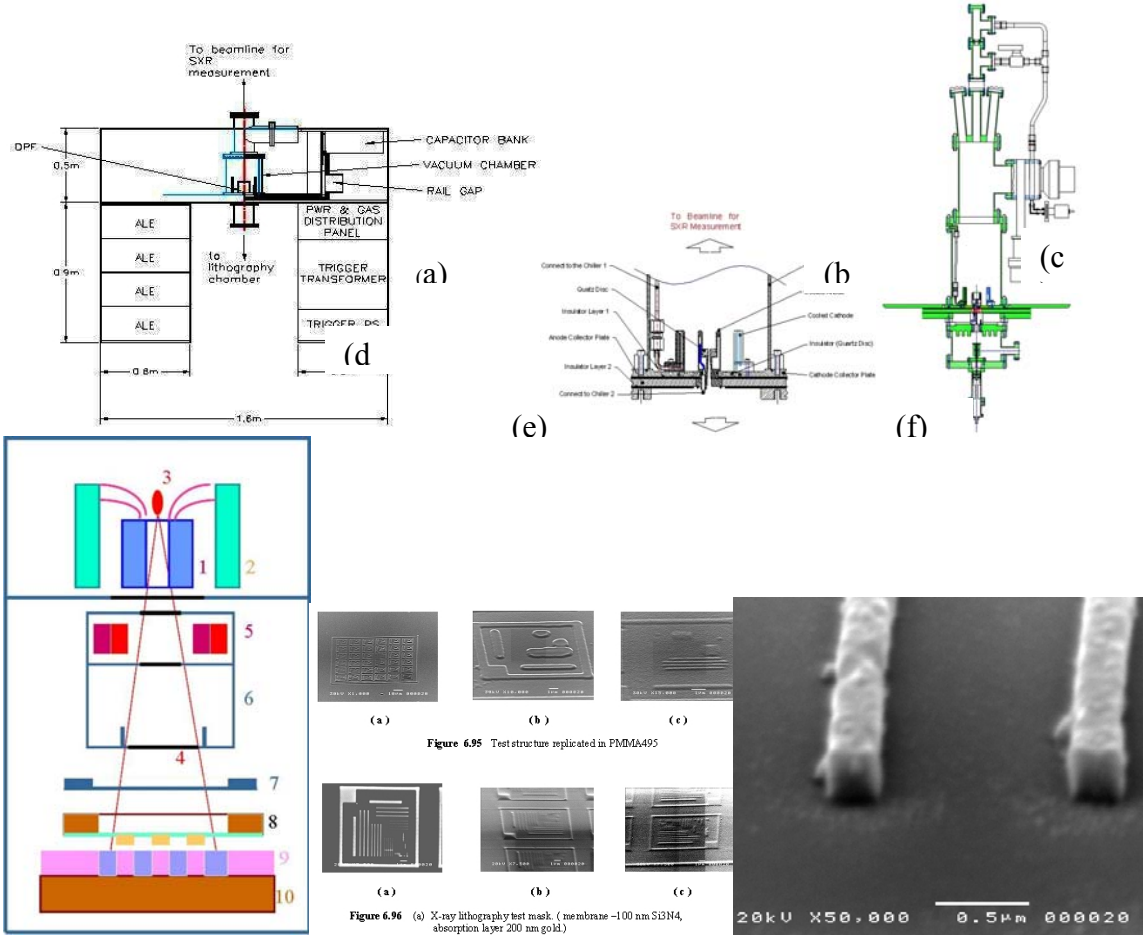

Fig 8 NX2 (Singapore) Lithographic machine, duplicated test structures and sub-micron lines [9]

systems.The lithography assembly is suspended below (behind) the focus electrodes platform see also Fig 8(d) which shows clearly the extraction of the neon SXR though the rear of the anode.
Fig 8(b) shows some details of the water-cooled anode and cathode structures. Fig 8(c) shows the m-high beamline for monitoring the SXR mounted above the plasma focus chamber. Fig 8(d) shows the details of the lithography beamline 1=hollow anode; 2= cathode; 3=focus pinch; 4= SXR beam extracted with a diverging angle; 5= magnets for deflecting electron beam; 6= holder with 3 in-line apertures extracting the SXR beam but reducing the shock/blast waves from the discharge; 7= berylium window; 8= SXR mask with pattern to be lithographed; 9= SXR resist on which lithograph pattern is formed; 10= substrate holding the SXR resist. Fig 8(e) shows 6 small squares in two rows. The top row are test structures replicated in resist of PMMA495. The left square of the second row is the SXR lithography test mask consisting of 200 nm gold features

placed on a supporting100 nm membrane of Si3N4. The other two squares are test structures replicated in ERP40 positive resist. Fig 8(f) shows details of two sub-micron replicated lithographed structures.
The NX2 is also used in repetitive mode for the related application of micro-machining, producing sub-micron high aspect ratio trenches; very well defined and with a much greater depth than the width. Figure 9 is a SEM image of a 100 nm trench micro-machined with neon SXR.

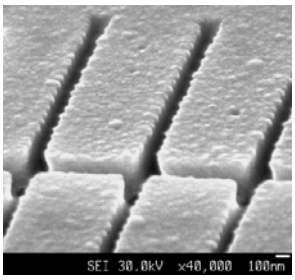

Fig 9 The NX2 producing micro-machined samples [9]

5.2 Materials deposition and advanced materials fabrication

A simple set-up for depositing thin films is shown in Fig 10. The centre of the anode is inserted with a cylinder of chromium and argon may be used as the operating gas. The electron

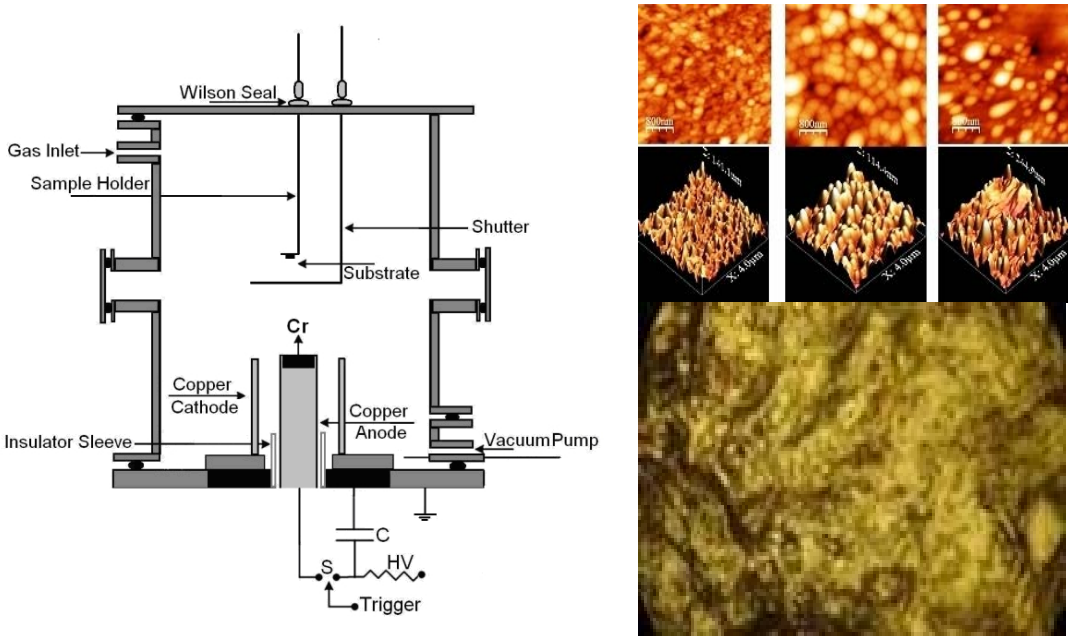

Fig 10. 2 kJ plasma focus for thin film deposition [10]; and samples of deposited chromium (Right side, top 2 rows) & TiN films (right side, bottom image)

beam from the pinch impacts on the chromium producing a post pinch chromium jet which moves to the sample, coating it within 20-30 shots. The shutter is opened for the process to begin only when the device is focussing strongly. For coating a sample surface with TiN the

chromium is replaced with titanium, and nitrogen is used as the operating gas. After the pinch the fast nitrogen plasma stream impacts the sample followed microseconds later by the anode-sputtered titanium plasma.

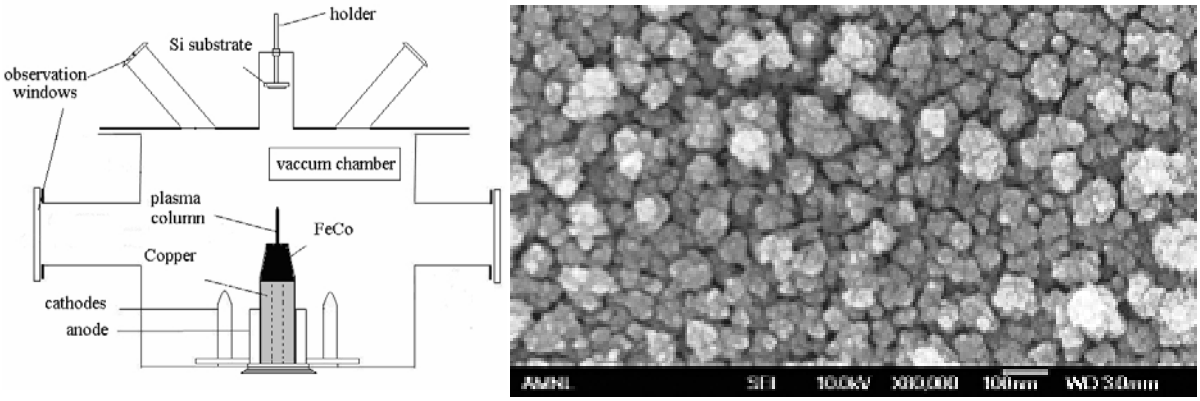

Fig 11 NX2 set-up for depositing thin films; deposited thin films with 100nm FeCo agglomerates [11]

Fig 11 shows the NX2 set-up for fabricating advanced nano-materials. In this set-up 100 nm agglomerates of FeCo are deposited consisting of grains typically 20 nm across. This material has potential for the next generation of ultra-high density of magnetic data storage. Other possible candidates are nano-structured materials like CoPt and FePt which are are also deposited.

5.3 A world-class product: Integrating a proven hardware package with a proven numerical experiments package: Developing the most powerful training and research system for the dawning of the Fusion Age.

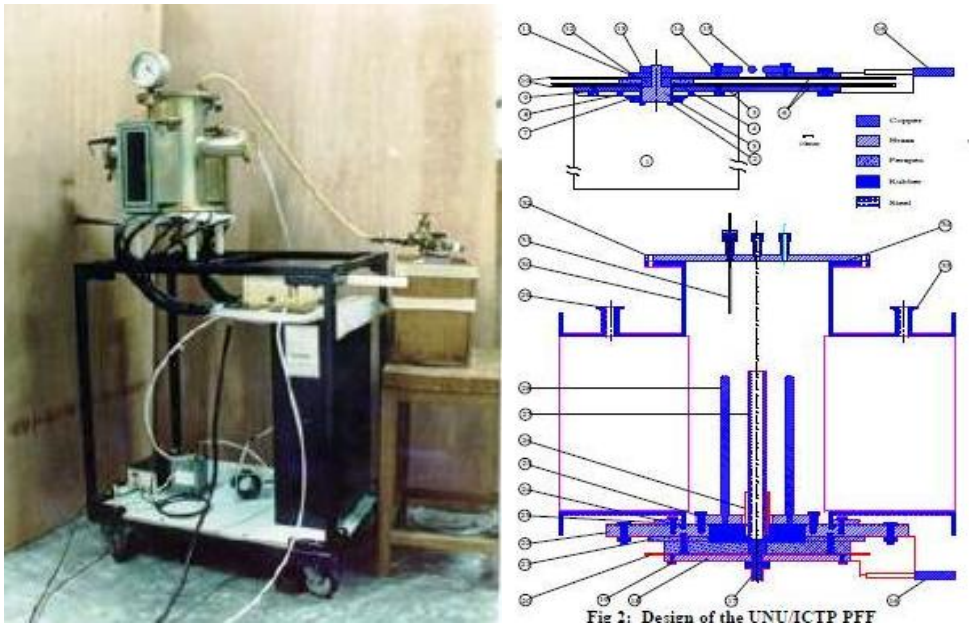

Fig 12. The trolley based UNU/ICTP PFF 3 kJ plasma focus training and research system [12]

Fig 12 shows the UNU/ICTP PFF 3 kJ system, already acknowledged as a very successful training and research package. It is ready to be updated technologically and then integrated to the Lee Model code with emphasis on dynamics, radiation and materials applications.

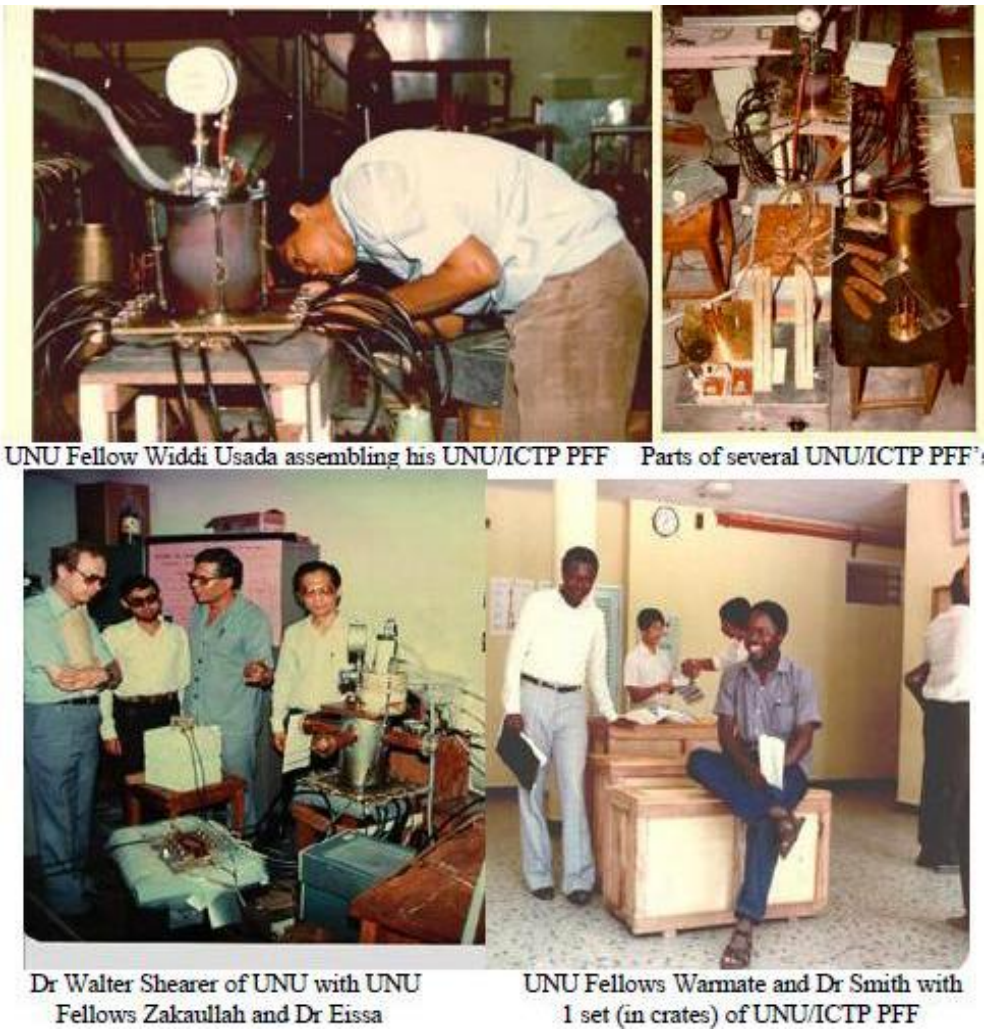

Fig 13 Building on a tradition (shown in this pictoral record) [12-14] the small plasma focus is ready to be developed into the world's most effective training and research package when integrated with the Lee model code [2.8] with emphasis on dynamics, radiation and materials applications.

It will draw on the spirit and tradition of the UNU/ICTP PFF (shown in the pictoral record of Fig 13) and the Lee model code. It will be the world's most effective training and research package developed to help meet the needs of scientific and engineering manpower for the inevitable dawning of the Fusion Energy Age [15].

References

[1] A Bernard, H Bruzzone, P Choi, H Chuaqui, V Gribkov, J Herrera, K Hirano, A Krejci, S Lee, C Luo, F Mezzetti, M Sadowski, H Schmidt, K Ware, C S Wong, V Zoita *Scientific Status of Plasma focus Research*. J Moscow Physical Society, 8, 93-170 (1998) .

[2] S Lee *Plasma focus model yielding trajectory and structure*. In Radiations in Plasmas, McNamara, B., Ed.; World Scientific, Singapore: Volume II, pp. 978–987 (1984)

[3] Glenn Millam Focus Fusion Society

[4] S H Saw, S Lee, F Roy, PL Chong, V Vengadeswaran, ASM Sidik, YW Leong & A Singh- In-situ determination of the static inductance and resistance of a plasma focus capacitor bank – Rev Sci Instruments 81, 053505 (2010)

[5] S Lee, S H Saw, R S Rawat, P Lee, R Verma, A.Talebitaher, S M Hassan, A E Abdou, Mohamed Ismail, Amgad Mohamed, H Torreblanca, Sh Al Hawat, M Akel, P L Chong, F Roy, A Singh, D Wong, K Devi. *Measurement and Processing of Fast Pulsed Discharge Current in Plasma Focus Machines*- J Fusion Energy DOI: 10.1007/s10894-011-9456-6 Online First™ 28 July 2011

[6] Muhammad Shahid Rafique. *Compression Dynamics and Radiation Emission from a Deuterium Plasma Focus* PhD thesis Nanyang Technological University, Singapore (2000).

[7] S. Lee, Harith Ahmad, T.Y. Tou, K.H. Kwek and C.S. Wong. *Dynamics of REB-sputtered copper plasma jets*. J. Fiz. Mal., Malaysia 6: 23-28 (1985)

[8] S Lee Radiative Dense Plasma Focus Computation Package: RADPF http://www.plasmafocus.net/IPFS/modelpackage/File1RADPF.htm (2012) http://www.intimal.edu.my/school/fas/UFLF/File1RADPF.htm (2019)

[9] G.X.Zhang. *Plasma Soft x-ray source for Microelectronics lithography*. PhD thesis, Nanyang Technological University Singapore (1999).

[10] M. Ghoranneviss*, S. Javadi, M. Habibi, Z. Abdolahi, S. Lee, S.H. Saw *Investigation of Structural Properties of Chromium Thin Films Prepared by Plasma Focus Device* (submitted for publication)

[11] R S Rawat, Z Ahang, J J Lin, Z Y Pan and P Lee *Application of Plasma Focus Device for Deposition of Nanostructured Magnetic Thin Films and Ion-irradiation Induced Nanostructuring of PLAD Grown Magnetic Thin Films* Proceedings of International Workshop On Plasma Computations & Applications Ed S H Saw et al 23-32 (2008)

[12] S.Lee, S.P.Moo, C.S.Wong, A.C.Chew. Twelve Years of UNU/ICTP PFF- A Review. IC/98/231, ICTP Preprint, International Centre for Theoretical Physics, Trieste, Italy (1998), 101 pages.

[13] S.Lee, T.Y.Tou, S.P.Moo, M.A.Eissa, A.V.Gholap, K.H.Kwek, S.Mulyodrono, A.J. Smith, Suryadi, W.Usala, M. Zakaullah. A simple facility for the teaching of plasma dynamics and plasma nuclear fusion. Amer J. Phys., USA, 1988, 56: 62-68.

[14] S Lee and S H Saw. J Fusion energy 30, 398-403 (2011)

[15] Sing Lee & Chiow San *Wong Initiating and Strengthening Plasma Research in Developing Countries* Physics Today pg 31-36 May 2006

Invited Review Paper

Commercial Applications

Applications Experts

Invited Review Paper

Basis and Results of Research at the IPFS

S LEE

Institute for Plasma Focus Studies, 32 Oakpark Drive, Chadstone, VIC 3148, Australia

e-mail: leesing@optusnt.com.au

Abstract

The foundation of IPFS is grounded firmly on the international collaboration that was successfully implemented by the AAAPT in the development of the 3kJ UNU ICTP PFF system and the intensive training of research scientists from 10 countries. Together with the hardware systems a model and code was developed for the description of the plasma focus as a total system. This code has been continuously developed over the past 28 years and now constitutes a unique universal plasma focus numerical experiment facility. The code is configured to run any Mathers plasma focus in the world, connected to the reality of the machine by fitting the computed current to the measured current waveform. The computed results include the gross dynamics, the pinch dimensions and lifetimes, temperatures and densities and the yields of neutrons and soft x-rays. In its latest forms the code also estimates ion beam yields and plasma stream fluences and the post-pinch energetics in terms of these fluences, available for materials fabrication and modification applications. Numerical experiments carried out with the code have provided ground-breaking insights including: 1) the futility of further inductance reduction (a very expensive technology) of the PF1000 - this concept of optimum inductance generalizable to all PF devices; 2) putting yield scaling laws on a firm footing with extension beyond experimental range; and 3) isolating the physical cause of 'neutron saturation' attributing it to the dynamic resistance; in the process also suggesting that 'yield saturation' is a misnomer for a mechanism more properly described as 'scaling deterioration' and applicable not only to neutrons but to all yields. More advanced variants of the code are continuously being developed e.g. to include current-stepping and radiation cooling and collapse to enhance compressions. With this code as a versatile numerical experimental facility adaptable to all machines the IPFS carries out research projects on an academic as well as consultative basis with research groups and activities in countries including Bulgaria, Chile, Egypt, India, Iran, Libya, Malaysia, Pakistan, Poland, Russia, Serbia, Singapore, South Korea, Syria, Thailand, US and Zimbabwe. With its tradition and experience the IPFS is uniquely positioned to coordinate and spearhead the development of a training and research package integrating hardware and numerical experiments for manpower training in fusion energy technology and applications.

1. Introduction

The Institute for Plasma Focus Studies was founded to promote the understanding of plasma focus devices. The power of the internet is utilised. The main instrument is the plasma focus numerical experiments package based on the Lee model, the latest being the version RADPFV5.15 with extension to RADPFV6.1.

From the mid-Eighties to mid-Nineties and on to this Millennium a group of us assisted in the starting and strengthening of several laboratories on plasma focus studies [1], using a 3 kJ plasma focus the UNU/ICTP PFF [2], specially designed for that purpose. More than 20 Fellows were trained to build, use and maintain this plasma focus through intensive hands-on training programmes sponsored by UNU, ICTP, UNESCO and TWAS and the AAAPT. This plasma focus, though low-cost, has proved very useful in the education of plasma focus scientists. It is now actively operated in 7 countries and research on it has produced more than 22 PhD theses, 50 Masters theses and 200 peer reviewed research papers [3]. It has developed into several modern variants (notably the KSU PF (USA) [4], and the USofia PF (Bulgaria) [5]; and many devices have been/are being built based on its design. The sub-systems are shown in Fig 1.

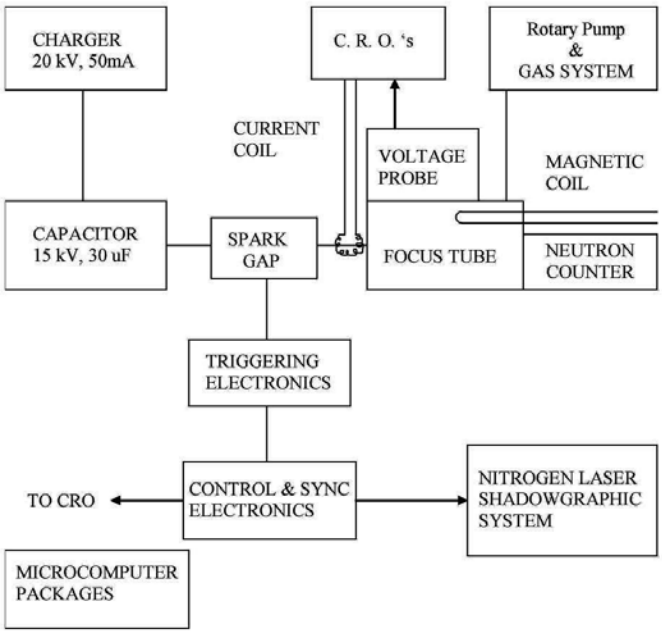

Fig 1. Sub-systems of the UNU/ICTPPFF

From the very beginning of that program it was realized that the laboratory work should be complemented by computer simulation. A 2-phase model was developed in 1984 [6,7]. Over the years we have developed the model until its present form [8-11]. It now includes thermodynamics data so the code can be operated in H_2, D_2, N_2, O_2, He, Ne, Ar, Kr, Xe. We have used it to simulate a wide range of plasma focus devices from the sub-kJ PF400J (Chile) [12] through the small 3kJ UNU/ICTP PFF (Network countries) [13], the NX2 3kJ Hi Rep lithographic focus (Singapore) [14], medium size tens of kJ DPF78 [15] and Poseidon (Germany) to the MJ PF1000 [16]. An Iranian Group has modified the model, giving it the name of Lee model, to simulate Filippov type plasma focus [10].

We are now confident that the Lee model code in its latest version the RADPFV6.1 [17]; realistically simulates all Mather plasma focus, small to large, high and low static inductance; and produce reliable results including axial and radial trajectories, speeds, pinch dimensions and lifetimes, circuit and plasma currents and energy distributions; and also gives a good representation of temperatures and densities, radiation and neutron yields [9]; ion beams number and energy fluences, post-pinch plasma and sputtered anode jet energetics. Although we can simulate any machine without any experimental input, our standard practice requires a measured

circuit current waveform from the specific machine together with bank parameters (capacitance, static inductance), tube parameters (cathode/anode radii, anode length) and operating parameters (voltage, pressure and gas). We configure the code with these parameters. We use 4 model parameters (a mass swept-up factor and a plasma current factor for each of axial and radial phases) to fit the computed to the measured current trace. The process, carried out sequentially for axial and radial phases, usually ends with an excellent fit for both shape and absolute magnitudes of the total current waveform [9,17-22].

The discharge current, particularly the fraction of it flowing in the plasma, drives all the electrodynamic processes in the axial and radial phases; even the plasma heating and radiation are coupled into the equation of motion. Conversely all these processes are reflected back in the profile of the plasma and circuit current. The circuit current carries in its profile and magnitudes the information of all processes that go on in the focus. Thus having fitted the computed with the measured I_{total} trace, we are confident that all processes are realistically simulated; and the numerical results are realistic representation of the actual properties of that particular plasma focus.

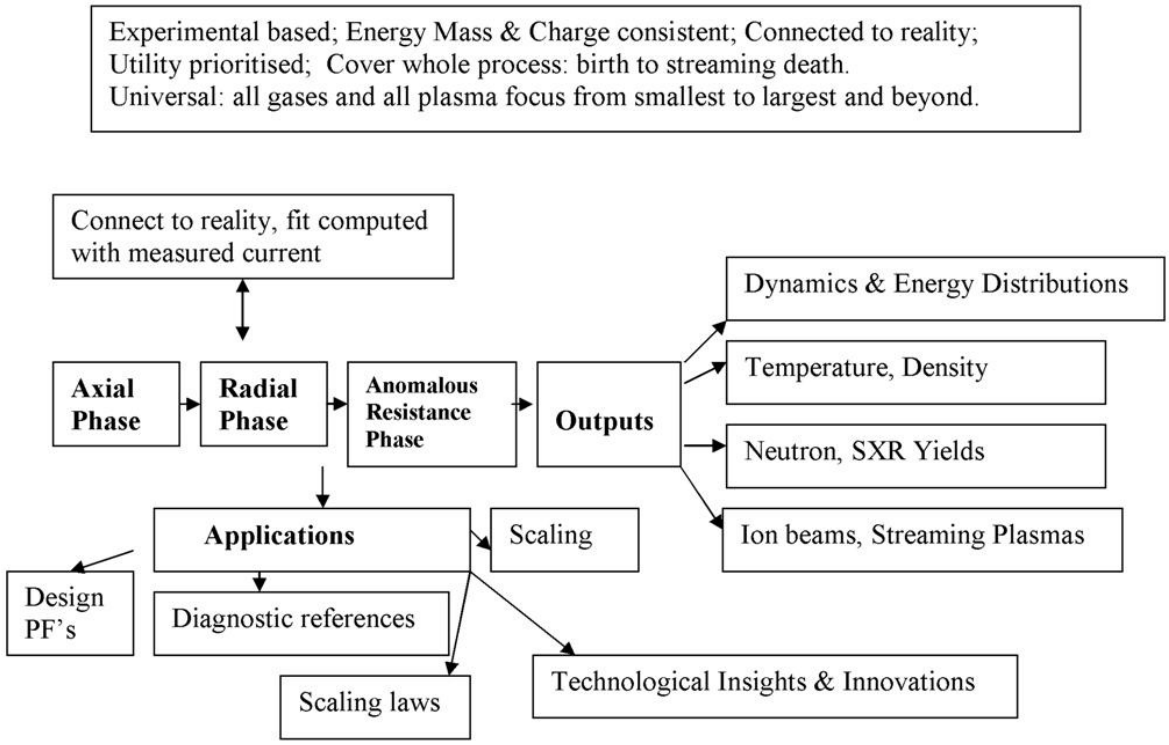

Fig 2. The philosophy, the phases, the outputs and applications of the Lee model code

The philosphy, the computation phases, the outputs and applications of the code is shown in Fig 2. The strength of the code is its rigorous basis in being energy, mass and charge consistent yet its flexibility in encompassing all machine effects including known effects and even unsuspected effects by adjusting (fitting) two factors, the mass swept-up factor and the current drive factor, in each phase so that the computed circuit current waveform agrees with the measured circuit current waveform in 5 critical features. When the computed waveform is properly fitted to the measured waveform, the code outputs the gross behaviour and properties of

the plasma focus from its electric birth through all its phases. The axial phase dynamics are presented. The lifetime and dimensions of the focus pinch are obtained and even the data of its streaming death in terms of the ion beam number and energy fluences and the energetics of the plasma stream and anode sputtered copper jet are presented; these latter data being of particular interest to materials applications. For a mid-distance view the model presents the complete life history and properties of any plasma focus operating with a choice of many gases. The versatility of the model is unmatched.

2. The Phases of the Plasma Focus

The five phases (*a-e*) are summarised [8,9, 11-22] as follows:

a.Axial Phase *(see Fig 3 left part):* Described by a snowplow model with an equation of motion which is coupled to a circuit equation. The equation of motion incorporates the axial phase model parameters: mass and current factors f_m and f_c [9,23,24]. The mass swept-up factor f_m accounts for porosity of the current sheet, inclination of the current sheet-shock front structure, boundary layer effects, and all other unspecified effects which are equivalent to increasing or reducing the amount of mass in the moving structure. The current factor f_c accounts for the fraction of current effectively flowing in the moving structure (due to all effects such as current shedding at or near the back-wall, and current sheet inclination). This defines the fraction of current effectively driving the structure, during the axial phase.

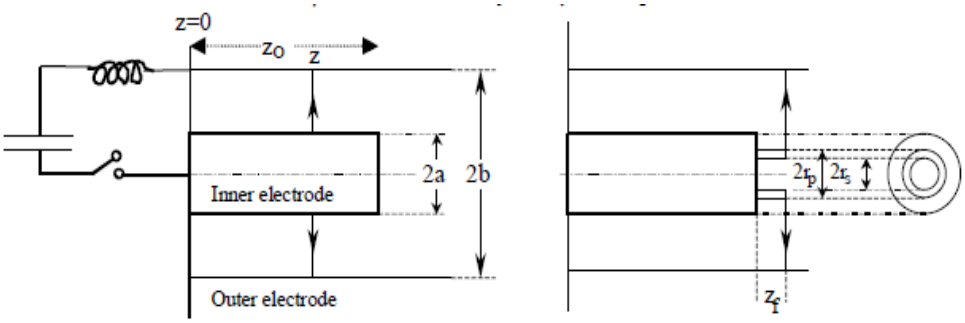

Fig 3. Schematic of the axial and radial phases. The left section depicts the axial phase, the right section the radial phase. In the left section, z is the effective position of the current sheath-shock front structure. In the right section r_s is the position of the inward moving shock front driven by the piston at position r_p. Between r_s and r_p is the radially imploding slug, elongating with a length z_f. The capacitor, static inductance and switch are shown for the axial phase schematic only.

b. Radial Inward Shock Phase *(see Fig 3 right part):* Described by 4 coupled equations using an elongating slug model. The first equation computes the radial inward shock speed from the driving magnetic pressure. The second equation computes the axial elongation speed of the column. The third equation computes the speed of the current sheath, (magnetic piston), allowing the current sheath to separate from the shock front by applying an adiabatic approximation [25]. The fourth is the circuit equation. Thermodynamic effects due to ionization and excitation are incorporated into these equations, being important for gases other than hydrogen and deuterium. Temperature and number densities are computed using shock-jump equations. A communication delay between shock front and current sheath due to the finite small disturbance speed [9,25] is crucially implemented. The model parameters, radial phase mass swept-up and current factors f_{mr} and f_{cr} are incorporated in all three radial

phases. The mass factor f_{mr} accounts for all mechanisms affecting the amount of mass in the moving slug. The current f_{cr} is the fraction of current effectively flowing in the moving piston forming the back of the slug (due to all effects).

c. Radial Reflected Shock (RS) Phase *:* When the shock front hits the axis, the focus plasma is collisional, a reflected shock develops which moves radially outwards, whilst the radial current sheath piston continues to move inwards. Four coupled equations are used to describe this phase, these being for the reflected shock moving radially outwards, the piston moving radially inwards, the elongation of the annular column and the circuit. The plasma temperature behind the reflected shock undergoes a jump by a factor close to 2. Number densities are also computed using the reflected shock jump equations.

d. Slow Compression (Quiescent) or Pinch Phase: When the out-going reflected shock hits the inward moving piston, the compression enters a radiative phase in which for gases such as neon, radiation emission may actually enhance the compression as we have included energy loss/gain terms from Joule heating and radiation losses into the piston equation of motion. Three coupled equations describe this phase; these being the piston radial motion equation, the pinch column elongation equation and the circuit equation. The duration of this slow compression phase is set as the small disturbance transit time across the plasma column.

e. Expanded Column Phase: To simulate the current trace beyond this point we allow the column to suddenly attain the radius of the anode, and use the expanded column inductance for further integration. In this final phase the snow plow model is used, and two coupled equations are used similar to the axial phase above.

3. Fitting the current trace

3.1 Configuring the code

To configure the code to any given machine we require the following parameters:

Bank parameters: capacitance C_0; (static inductance L_0 and stray resistance r_0 are not required, though would simplify the fitting procedure, if available)

Tube parameters: cathode radius b, anode radius a, anode length z_0, the latter may need adjustment during fitting

Operational parameters: Voltage V_0, pressure and gas type

Also required is a measured current waveform. A digital data file of rate of change of current with time *dI/dt* is preferred as typically the *dI/dt* signal contains less distortion than current waveform data which has been processed by a hardware integrator [26.27]. The current waveform only needs reliable frequency response and need not be calibrated. Once the current waveform shape is correctly fitted, the computed amplitude of current is the correct one. This is because the code is charge consistent.

3.2 Fitting

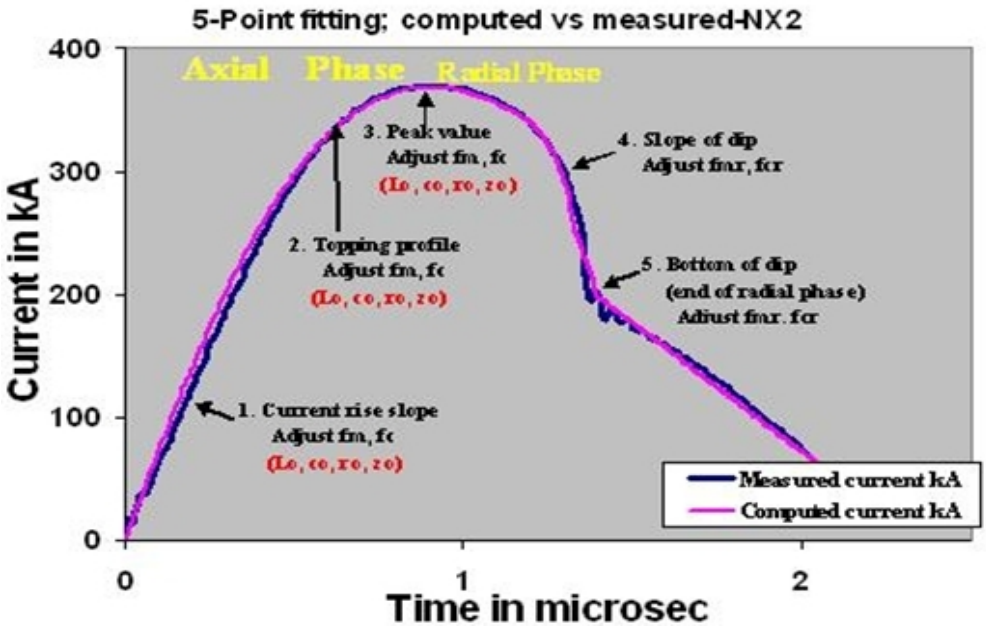

Fig 4. Illustraing 5 point sequential fitting procedure

The precedure for fitting is listed here:

1. The measured current waveform (numerically integrated if necessary) is placed on the same chart as the computed. An adjustable magnitude scaling factor is applied to the measured waveform. An adjustable time shift is also applied to shift the measured to allow correct time alignment.
2. Trial model parameters are chosen; typically f_m=0.05, f_c=0.7, f_{mr}=0.12 and f_{cr}=0.7. A shot is numerically fired. The computed waveform is compared with the measured.
3. Fitting points 1 and 2 (see Fig 4) need to be correctly fitted. Each time an adjustment is made to a parameter a shot is fired and comparison of the two waveforms is made visually. Then another adjustment and so on. Points 1 and 2 (Fig 4) cannot be fitted unless L_0 is correctly configured. The magnitude scaling factor is adjusted looking also at fitting Point 3; and time shift if necessary. Once fitted, L_0 is correctly given (or adjusted) and the meassured current waveform is also correctly calibrated using the computed values.
4. Whilst step 3 above is being carried out the value of f_m may also need to be adjusted so that the start of current dip (that is the part between Points 3 and 4) comes correctly.
5. When step 4 above has been completed as best as possible the axial phase fitting is tentatively completed and the fitting moves on to the radial phase. The value of f_{mr} is adjusted step be step, a shot is fired at each step and comparison of waveforms visually is made for best fit of Points 4 and 5 (Fig 4).
6. While step 5 is being carried out very small adjustments to f_m may be necessary.
7. Figure 4 illustrates the end product of a satisfactory fit for one of the measured current trace of NX2.

3.3 Results

On completion of fitting, realistic results are presented of dynamics, properties of pinch, energy distributions and yields. Some results for NX2, optimized for neon, are shown in Fig 5.

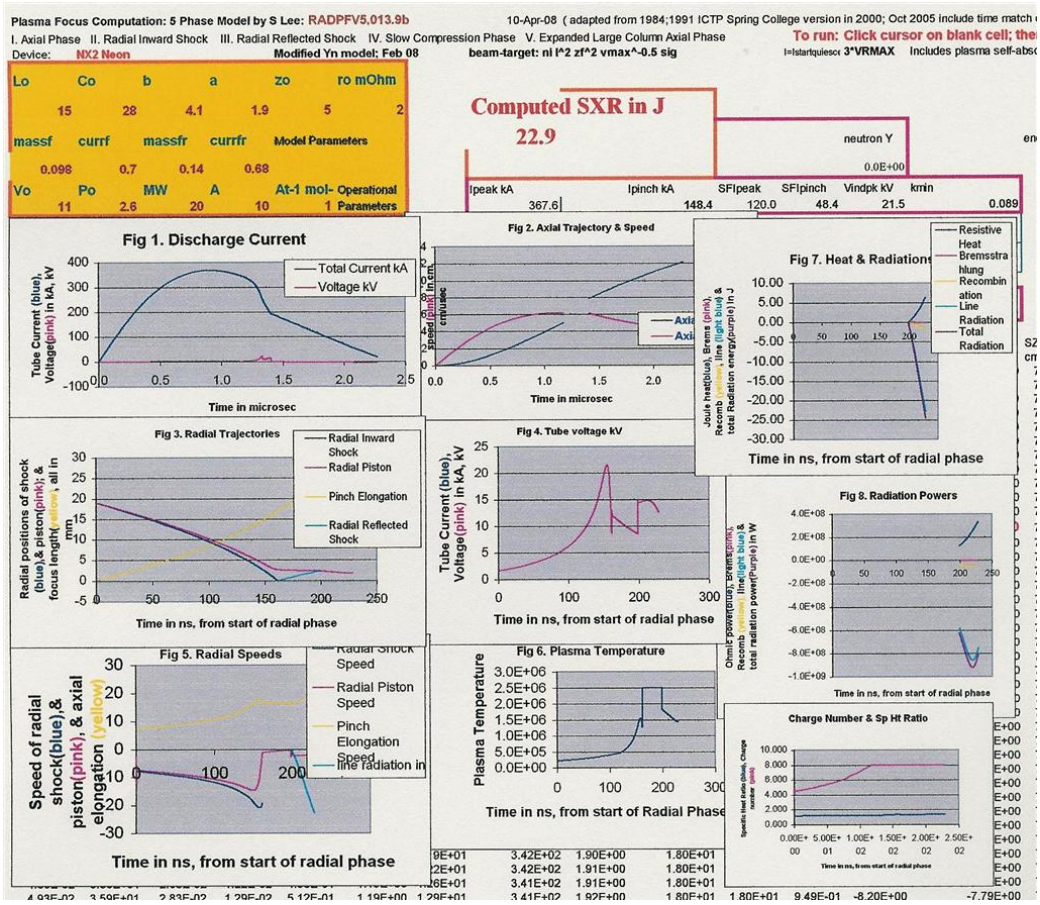

Fig 5. Some results of output of code at the end of the fitting process

4. Applications

4.1 Scaling Properties

From many numerical experiments the following rule-of-thumb scaling relationships are derived, subject to minor variations caused primarily by the variation in $c=b/a$.

Axial phase energy density (per unit mass)	constant
Radial phase energy density (per unit mass)	constant
Pinch radius ratio	constant
Pinch length ratio	constant
Pinch duration per unit anode radius	constant
Dynamic resistance, axial phase	constant

The dense hot plasma pinch of a small E_0 plasma focus and that of a big E_0 plasma focus have essentially the same energy density [6-8], the same mass density. The big E_0 plasma focus has a

bigger physical size and a bigger discharge current. The size of the plasma pinch scales proportionately to the current and to the anode radius, as does the duration of the plasma pinch. The bigger E_0, the bigger I_{peak}, the bigger 'a' has to be, correspondingly the larger the plasma pinch radius and the longer the duration of the plasma pinch. The larger size and longer duration of the big E_0 plasma pinch are essentially the properties leading to the bigger neutron yield compared to the yield of the small E_0 plasma focus. We have also included that the axial phase dynamic resistance is a constant as a rule-of thumb. This is related to the constant axial phase energy density but is listed here as it plays a predominant role in the physical mechanism of deterioration of yield scaling which we suggest has been mistaken as 'neutron saturation'.

4.2 Dimensions and Lifetimes of the plasma focus in D and Ne

Derived from numerical experiments these are listed in Table 1 and are consistent with laboratory observations [9,28].

Table 1 Plasma Focus dimensions and lifetime scaling with anode radius a; lifetime in s, when a is in m. **The units of the speed factor SF are**: (kA/cm)/(torr$^{0.5}$)

Plasma Focus Pinch Parameters		Deuterium	Neon (for SXR)
Minimum radius	r_{min}	0.15a	0.05a
Max length (hollow anode)	z	1.5a	1.6a
Radial shock transit	t_{comp}	5x10^{-6}a	4x10^{-6}a
Pinch lifetime	t_p	10^{-6}a	10^{-6}a
Speed Factor	S	90	

4.3 Scaling Laws

4.3.1 Neutron yield

Over wide ranges of energy, optimizing pressure, anode length and radius, the scaling laws for Y_n [16,21,22,29] obtained through numerical experiments are listed here:

Y_n=3.2x10$^{11}I_{pinch}^{4.5}$ and Y_n=1.8x10$^{10}I_{peak}^{3.8}$ with I_{peak} (0.3 to 5.7), I_{pinch} (0.2 to 2.4) in MA

$Y_n \sim E_0^{2.0}$ at tens of kJ to $Y_n \sim E_0^{0.84}$ at MJ level (up to 25MJ)

These laws provide useful references and facilitate the understanding of present plasma focus machines. More importantly, these scaling laws are also useful for design considerations of new plasma focus machines particularly if they are intended to operate as optimized neutron sources.

4.3.2 Neon SXR yield

Over wide ranges of energy, optimizing pressure, anode length and radius, the scaling laws for neon SXR are found [30] by numerical experiments to be:

Y_{sxr}=8.3x10^{3}x$I_{pinch}^{3.6}$

Y_{sxr}=600x$I_{peak}^{3.2}$; I_{peak} (0.1 to 2.4), I_{pinch} (0.07 to1.3) in MA.

$Y_{sxr} \sim E_0^{1.6}$ (kJ range) to

$Y_{sxr} \sim E_0^{0.8}$ (towards MJ).

These laws provide useful references and facilitate the understanding of present plasma focus machines. More importantly, these scaling laws are also useful for design considerations of new plasma focus machines particularly if they are intended to operate as neon SXR sources.

4.4 Insights derived from numerical experiments

4.4.1 The global neutron scaling law

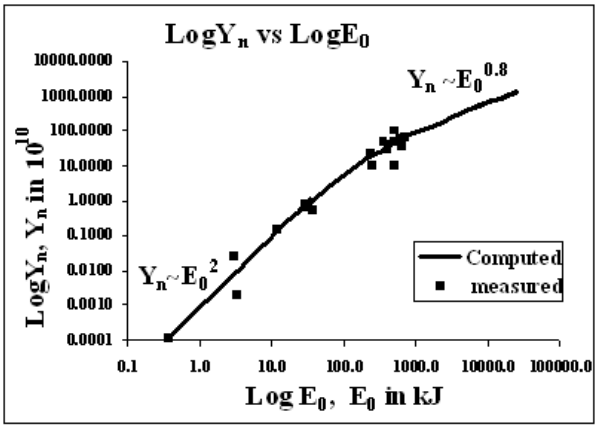

Fig 6 . The global scaling law, combining experimental and numerical data. The data illustrates Y_n scaling observed in numerical experiments from 0.4 kJ to 25 MJ (solid line) using the Lee code, compared to measurements compiled from publications (squares) of machines from 0.4 kJ to 1 MJ.

4.4.2 The cause of neutron saturation

Historically the most appealing quantity for use as the base for scaling is the stored energy used to drive the focus. Using the highest voltage technologically convenient, all one needs to do to scale up energy (E_0=0.5$C_0V_0^2$) is to put more capacitors in parallel, increasing the capacitance C_0 and decreasing the static inductance L_0 of the bank to some extent. Along these lines, early work has shown that Y_n~E_0^2. Under ideal conditions (minimized inductance L_0 and when the system is dominated by the generator impedance) the capacitor current I may have the relationship I~$E^{0.5}$, then it quickly follows that Y_n~I^4. However it was found that when the capacitor bank reached storage energies of only several hundred kJ the neutron yield no longer increased; the so-called neutron saturation effect [31]. Our numerical experiments showed that whilst the discharge circuit is indeed dominated by the generator impedance at low energies (i.e. low C_0) so that indeed I~$E^{0.5}$; at a certain point when the C_0 (i.e. E_0) gets sufficiently big, the generator impedance has dropped to the value of the load impedance, principally the axial dynamic resistance [29]. As E_0 is increased even further and further, the generator impedance eventually becomes negligible when compared to the dynamic resistance which remains relatively constant, hardly affected by the decreasing generator impedance [21,29]. Eventually at very large E_0, the constant load impedance completely dominates and the circuit current reaches an asymptotic value and hardly increases for any further increase in E_0. At this point which would be beyond the high tens of MJ, the capacitor current is saturated, leading to neutron saturation. What is observed at hundreds of kJ which has been termed neutron saturation is based on very limited data. When data from experiments is put together with data from rigorous systematic numerical experiments, the global picture shows the scaling deterioration very clearly (see Fig. 6) [21].

4.4.3 Pinch Current Limitation Effect as Static Inductance is Reduced Towards Zero

In a 2007 paper [32] there was expectation that the large MJ plasma focus PF1000 in Warsaw could increase its discharge current, and its pinch current, and consequently neutron yield by a reduction of its external or static inductance L_0. To investigate this point, experiments were carried out using the Lee model code. Unexpectedly, the results indicated that whilst I_{peak} indeed progressively increased with reduction in L_0, no improvement may be achieved due to a pinch current limitation effect [18,19]. Given a fixed C_0 powering a plasma focus, there exists an optimum L_0 for maximum I_{pinch}. Reducing L_0 further will increase neither I_{pinch} nor Y_n. The reason for this is that as L_0 decreases, I_{peak} increases leading to the necessity of bigger 'a' which leads to a longer pinch and hence a bigger pinch inductance. The tube inductance becomes smaller since the current risetime is reduced. Moreover reduction of L_0 decreases the interaction time between the pinch and the capacitor so that the pinch inductive voltage effectively drives more current back to the capacitor bank. The interplay of all these effects reduce the ratio of I_{pinch}/I_{peak} resulting in the pinch current limitation effect.

5. The best training and applications package in the world- Training scientific manpower for the dawning of the Fusion Age

From the successful experience of the research results produced by the 3.3 kJ UNU ICTP PFF, there is a case to be made for an updated slightly smaller version. A 1 kJ system consisting of a 10 kV fast capacitor, 20 μF in capacity switched by a psudo spark gap along the lines of the KSU plasma focus [4] is envisaged with the diagnostic subsystems[3] as shown in Fig 1 so that all basic measurements of electrical parameters, dynamics and neutron yield may be measured. In addition SXR spectrometry [33] could be introduced together with simple experiments for thin film fabrication and nano particle sythesis. This hardware package is complemented by the Lee model code [9] which will allow the detailed mechanisms of the 1 kJ focus to be fully explored using the combination of the hardware package. The code also allows the research to be extended for comparative studies with other machines since the code handles all machines and all gases. Whilst fixed firmly in research grounding with the experiments provided by the 1 kJ machine, the research may explore technology leading systems including the latest frontiers involving radiative cooling [34] and circuit manipulation [35] in the quest for compression enhancement. Such an integrated package will provide excellent training, research and applications in the coming age of nuclear fusion energy technology [36,37].

References

[1] Sing Lee & Chiow San Wong. Physics Today. May 2005 31-36

[2] Lee, S.; Tou, T. Y.; Moo, S. P.; Eissa, M. A.; Gholap, A. V.; Kwek, K. H.; Mulyodrono, S.; Smith, A. J.; Suryadi, S.; Usada, W.;. Zakaullah, M. *A simple facility for the teaching of plasma dynamics and plasma nuclear fusion*. Amer. J. Phys. *56,* no. 1, 62–68.(1988)

[3] Lee S *Twelve Years of UNU/ICTP PFF—A Review* IC, 98 (231) Abdus Salam ICTP, Miramare, Trieste; ICTP OAA: http://eprints.ictp.it/31/ (1998)

[4] M I Ismail, A E Abdou, A E Mohamed, S Lee, S H Saw- *Kansas State University Dense Plasma Focus (KSU-DPF) Initial Neutron Results*. IEEE 38th ICOPS, Chicago 26-30 June 2011 IP3F-35.

[5] S. Zapryanov, V. Yordanov, A. Blagoev. *Measurements of the Basic Characteristics of the Dense Plasma Focus Device*. Bulg. J. Phys. 38 184–190 (2011)

[6] Lee S in *Radiations in Plasmas* ed B McNamara (Singapore: World Scientific) pp 978–87 (1984)
[7] Lee S in *Laser and Plasma Technology*, edited by S. Lee, B. C. Tan, C. S. Wong, and A. C. Chew. World Scientific, Singapore, pp. 387–420. (1985)
[8] Lee S 2000/2007 http://ckplee.myplace.nie.edu.sg/plasmaphysics/
[9] Lee S *Radiative Dense Plasma Focus Computation Package: RADPF* www.plasmafocus.net www.intimal.edu.my/school/fas/UFLF/ (2012)
[10] Siahpoush V, Tafreshi M A, Sobhanian S & Khorram S. Plasma Phys Control. Fusion 47 1065 (2005)
[11] M. Akel, Sh. Al-Hawat, S. H. Saw and S. Lee. *Numerical Experiments on Oxygen Soft X-Ray Emissions from Low Energy Plasma Focus Using Lee Model*. J Fusion Energy 29: 223;231(2010)
[12] Lee S., Saw S. H., Soto L., Moo S. P., Springham S. V., *Numerical experiments on plasma focus neutron yield versus pressure compared with laboratory experiments*, *Plasma Phys. Control.Fusion*, *51* 075006 (2009)
[13] Saw S. H., Lee P. C. K., Rawat R. S. & Lee S. *Optimizing UNU/ICTP PFF Plasma Focus for Neon Soft X-ray Operatio.n IEEE Trans on Plasma Sc*, *37* 1276-1282. (2009)
[14] Lee S., Rawat R. S., Lee P., S H Saw S. H., *Soft x-ray yield from NX2 plasma focus*, *JOURNAL OF APPLIED PHYSICS*, *106*, 023309 (2009)
[15] Lee S., Saw S. H., Lee P. C. K., Rawat R.S., and Schmidt H., *Computing plasma focus pinch current from total current measurement, Appl. Phys. Lett*, *92*, no. 11, p. 111 501 (2008)
[16] Lee S. and Saw S. H. *Neutron scaling laws from numerical experiments,* J. Fusion Energy, *27*, no. 4, pp. 292–295 (2008)
[17] S Lee, S H Saw, A E Abdou & H Torreblanca *Characterizing plasma focus devices- role of static inductance-instability phase fitted by anomalous resistances* J Fusion Energy: 30 277-282 (2011)
[18] Lee S. & Saw S H *Pinch current limitation effect in plasma focus* Appl Phys Lett *92*, 021 503 *(2*008)
[19] Lee S., Lee P., Saw S. H., and Rawat R. S. *Numerical experiments on plasma focus pinch current limitation Plasma Phys. Control. Fusion 50*, no. 6, 065 012 (2008)
[20] Sing Lee and Sor Heoh Saw *Numerical Experiments Providing New Insights into Plasma Focus Fusion Devices* Energies *3*, 711-737; doi:10.3390/en3040711 (2010)
[21] S. Lee *Neutron Yield Saturation in Plasma Focus-A fundamental cause* Appl Phys Lett 95, 151503 93 (2009)
[22] S H Saw and S Lee, *Scaling the Plasma Focus for Fusion Energy Considerations*-, Int. J. Energy Res 35: 81–88 (2011)
[23] Chow S P, Lee S and Tan B C, J. of Plasma Phys 8: 21-31 (1972)
[24] Sh Al-Hawat, M. Akel , S. Lee, S. H. Saw *Model parameters vs. gas pressure in two different plasma focus devices operated in Argon and Neon* J Fusion Energy 31: 13–20 (2012)
[25] Potter, D. E. *The formation of high-density z-pinches*. Nucl. Fusion. *18*, 813–823 (1978)
[26] S H Saw, S Lee, F Roy, PL Chong, V Vengadeswaran, ASM Sidik, YW Leong & A Singh *In-situ determination of the static inductance and resistance of a plasma focus capacitor bank* Rev Sci Instruments 81, 053505 (2010)
[27] S Lee, S H Saw, R S Rawat, P Lee, R Verma, A.Talebitaher, S M Hassan, A E Abdou, Mohamed Ismail, Amgad Mohamed, H Torreblanca, Sh Al Hawat, M Akel, P L Chong, F Roy, A Singh, D Wong and K Devi. *Measurement and Processing of Fast Pulsed Discharge Current in Plasma Focus Machines*- J Fusion Energy DOI:10.1007/s10894-011-9456-6 Online First™ 27 July 2011
[28] Lee S and Serban A. *Dimensions and lifetime of the plasma focus.* IEEE Trans. Plasma Sci. 24 1101–5 (1996)
[29] S Lee. *Current and Neutron Scaling for Megajoule Plasma Focus Machines*, Plasma Phys. Control. Fusion, 50 105005 (2008)
[30] Lee S., Saw S. H., Lee P. & Rawat R. S. *Numerical Experiments on Neon plasma focus soft x-rays scaling* Plasma Physics and Controlled Fusion *51*, 105013 (2009).
[31] Bernard A et al *Scientific Status of Plasma focus Research* Moscow J Physical Soc 8, 93-170(1998)
[32] Gribkov V A *et al* J. Phys. D: Appl. Phys. 40 1977 (2007)
[33] S Lee, S H Saw, R S Rawat, P Lee, A.Talebitaher, P L Chong, F Roy, A Singh, D Wong and K Devi *Correlation of soft x-ray pulses with modeled dynamics of the plasma focus*- IEEE Trans on Plasma Sci Volume 39, No 11, 3196-3202 (2011)
[34] S Lee, S H Saw and Jalil Ali. *Numerical experiments on radiative cooling and collapse in plasma focus operated in krypton*. In production J Fusion Energy (2012)
[35] S Lee and S H Saw. *Current-Step Technique to Enhance Plasma Focus Compression and Neutron Yield.* J Fusion Energy DOI: 10.1007/s10894-012-9506-8 Published Online 31 January 2012

[36] S Lee and S H Saw, *The Plasma Focus- Trending into the Future*. International J of Energy Research; Article first published online: 9 SEP (2011)
[37] Sing Lee and Sor Heoh Saw. *Nuclear Fusion Energy- Mankind's Giant Step Forward* J Fusion Energy Volume 30, Number 5, 398-403 (2011)

Invited Review Paper

Plasma Focus Research at INTI-IU

S H SAW
INTI International University, Nilai, Malaysia
e-mail: sorheoh.saw@newinti.edu.my

Abstract
The INTI Plasma Focus (INTI PF) is one of the 3 kJ Plasma Focus known as the UNU ICTP PFF. It has been be operated at up to 15 kV (180 kA) in neon and deuterium with remarkable focusing consistency and yields of neutrons (10^8 per shot), neon SXR (4J), ion beam fluences of 10^{21} ions/m^2 per shot at 80 keV carrying ion energy fluence of 10^7 J/m^2 per shot with beam energy of 20 J per shot at pinch exit; together with plasma stream energy of 250 J per shot at speeds up to 50 cm/μs and anode sputtered materials carrying energy of 20J per shot (100 μg of 300 eV copper ions). These results are obtained from a combination of experiments and numerical experiments using the Universal Plasma Focus Laboratory Facility. We have developed important diagnostic systems including a standard current coil measurement system associated with an in-situ method for determining static inductance; a SXR spectrometric analysis template system for Neon soft x-rays and a magnetic probe analysis system. We have measured mass factors and anomalous resistances of our pinch plasmas under different discharge conditions and gases. We have led an international collaboration to standardize these diagnostic techniques and measurements so that the results of several machines are considered for comparison and consistency. Our studies include scaling properties and scaling laws; and pinch compression enhancement using current-stepping and radiation cooling. Among future directions of research we have identified are study of materials damage (of tungsten) and materials modification and coating such as titanium nitride film on stainless steel. Additional research equipment including a powerful optical microscope and access to a suite of materials characterization equipment are being arranged.

1. Introduction

The INTI-PF is a 3.3-kJ Mather-type plasma focus system powered by a single 15-kV 30-μF Maxwell capacitor switched on by a simple parallel-plate swinging cascade air gap [1]. The system was first installed in the Plasma Radiations Laboratory in NIE-NTU Singapore in 1991 and was donated to INTI-IU in 2007. It is now operated at 11-12 kV in neon, krypton and deuterium . The system produces remarkably consistent focusing actions and neutron yields of $0.5-1.0 \times 10^8$ neutrons per discharge at 3.0 Torr of deuterium operating at 15 kV and 180 kA [1,2], neon SXR yield of 0.3-3.7 J [3] per discharge at 1.6-3.3 Torr of neon operating at 12 kV; and ion beam fluences of 10^{21} ions/m^2 per shot at 80 keV carrying ion energy fluence of 10^7 J/m^2 per shot with beam energy of 20 J per shot at pinch exit; together with plasma stream energy of 250 J per shot at speeds up to 50 cm/μs and anode sputtered materials carrying energy of 20J per shot (if Cu 100 μg of 300 eV ions).

In addition to the INTI PF, the UFLF (Universal Plasma Focus Laboratory Facility) is used to study plasma focus scaling laws and innovative approaches to increase plasma current, density, temperature and radiations yield.

Areas of study currently being carried out at the Centre for Plasma Research are as follows:

Standard current coil measurement system
In-situ calibration system for static inductance of PF devices
Magnetic probes system to study axial speeds and current sheet structure
SXR spectrometer and analysis system for Neon plasma
Study of scaling properties and scaling laws
Determination of anomalous resistance in high inductance plasma focus from current signal
Study of pinch enhancement in plasma focus by current-stepping technique
Study of pinch enhancement in plasma focus by radiation cooling
Determination of ion beam flux of plasma focus from current signal

2. Standard current coil measurement system- combined with the Lee Model code produces all gross data of plasma focus a researcher would need

The discharge current drives all physical processes in the plasma focus device; in turn all physical processes in the focus affect the current waveform. Our recent work has established the central role of reliable current measurement to plasma focus diagnostics and understanding [4-6]. We have developed a simple robust reliable current measuring system to standardize collection of data on current for our collaborative projects with AECS, Syria and KSU, USA and other groups [7].

The current transformer with a large number of turns and a sub-1 Ohm terminator has good high frequency response, necessary for the sharp current dip region when *dI/dt* exceeds 2 x 10^{11} A/s. However the signal is ‘‘noisy’’ in the current dip region. The *dI/dt* coil, the Rogowski coil in ‘‘Idot’’ mode may have a few turns and is terminated by 50-Ohm. Integrating the 1 GSa/s digital waveform does remove the high frequency noise components, yet the extracted waveform shows sharp angular features indicative of the retention of short-time features. This makes the *dI/dt* coil superior to the current transformer. A 7-turn coil is tested against the Lee Model code and is found to be suitable to measure the plasma focus discharge current.

Figure 1 shows a schematic of the Rogowski coil in its location in the INTI PF set-up.

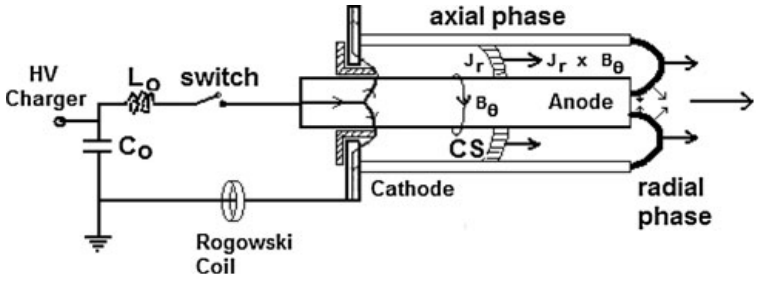

Fig 1. Showing the Rogowski coil placed around the discharge current to capture the current waveform.

Figures 2a shows the coil with its turns wrapped around the current to be measured whilst Fig 2b shows the equivalent circuit of the coil with coil inductance L_t and coil resistance r_c. The coil current i is induced by the discharge current I being monitored. The voltage V_0 is

developed across the terminating resistance r. The waveform of V_0 is recorded and is a measure of the discharge current I.

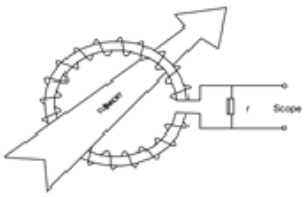

Fig 2a The Rogowski coil .

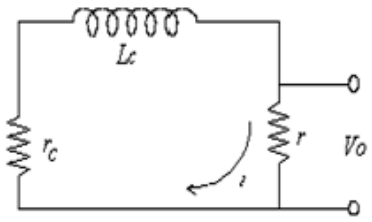

Fig 2b The equivalent circuit of the coil.

The circuit equation of the coil may be written as: $L_c(di/dt) + i(r+r_c) = kdI/dt$ where k is the coil constant coupling it to the discharge current I. Designing the coils so that $L_c(di/dt) << i(r+r_c)$, we have $i= (k/(r+r_c))dI/dt$ so that the measured voltage is $V_0 = (k/(r+r_c))rdI/dt$; that is measured voltage waveform is directly proportional to the rate of change of discharge current I.

We designed a 7-turn coil and find that by numerically integrating the output we are able to obtain current waveform compatible with that computed from the Lee Model code [8]. We experimented with several situations including situations where we deliberately distorted the measured waveform by positioning the coil in such a manner that it also picks up net external magnetic field. In all such distorted cases, the computed current waveforms could not be fitted to the 'deliberately distorted' measured waveform. Thus we also showed that if a measured current waveform of the plasma focus discharge could not be fitted to the computed waveform then the measured current waveform must be erroneous.

The combination of this 7-turn coil and the model code is a most powerful diagnostic technique. The code when configured as the particular plasma focus and then fitted to its correctly measured current waveform, then generates the dynamics, speeds, lifetime and dimensions and plasma properties of the pinch, the yields and also the energetics of the ion beam, the electron beam and the fast plasma stream including the anode jet; practically all the gross information a researcher would need for the plasma focus.

3. In-situ calibration system for static inductance of PF devices

The static inductance L_0 of a plasma focus circuit is important for consideration of its performance. It may be determined in a two-step method as follows. Assuming that the discharge current waveform is that from a lightly damped L_0-C_0-r_0 circuit, the waveform may be treated as sinusoid with period T, the following approximate equations hold [9]:

$$L_0 = T^2/(4\pi^2 C_0) \qquad r_0 = (-2/\pi)\ln(f)(L_0/C_0)^{0.5} \qquad I_0 = \pi C_0 V_0 (1+f)/T$$

where f is the reversal ratio obtained from the successive current peaks I_1, I_2, I_3, I_4, I_5 with $f_1=I_2/I_1, f_2=I_3/I_2, f_3 = I_4/I_3, f_4 = I_5/I_4$ and $f= (1/4)(f_1+f_2+f_3+f_4)$; and I_0 the highest peak current is written here as I_1, the peak current of the first half cycle.

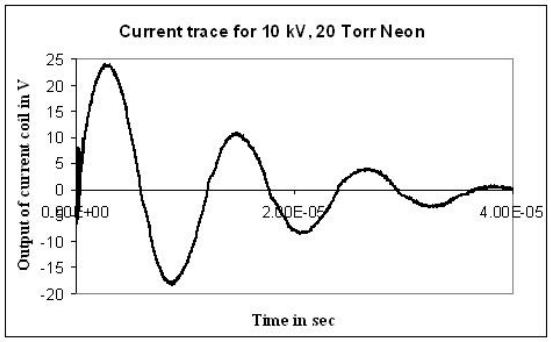

Fig 3 Measured discharge current waveform at high pressure so that the waveform is damped sinusoidal.

By measuring T and the reversal ratios, L_0 and r_0 are obtained; as well as I_0. This is Step 1 of the 2-step process. Step 1 assumes that at the high pressure there is no plasma or current sheet motion so the only inductance in the system is L_0. However, in reality there is still some motion which will introduce a time-varying inductance on top of L_0.

In Step 2 [9] the Lee model code [8] is configured as the plasma focus with the value of L_0 estimated in Step 1; and a shot is fired. Because of the high pressure, the current sheet does not complete the axial phase so there is no radial phase. The code is run only in the axial phase and the computed current trace is fitted to the measured current trace. To get a good fit not only the axial model parameters f_m and f_c have to be fitted but is found that L_0 (with value taken from Step 1) has to be reduced to get a good fit, and r_0 correspondingly. This completes Step 2 and the correct values of L_0 and r_0 are thus obtained.

4. Magnetic probes system to study axial speeds and current sheet structure

A magnetic probe relies on magnetic flux from the current inducing a voltage on a coil, similar in principle but topologically different to the current coil discussed in Section 2 above. The magnetic probe may consist of a small short coil of hair-thick enameled wire wrapped a few turns around a tiny insulating former and inserted into a glass jacket to protect it from the plasma and electric currents. The ends of the coil are taken in a twisted pair (see Fig 4) out to a coaxial cable thence to the DSO.

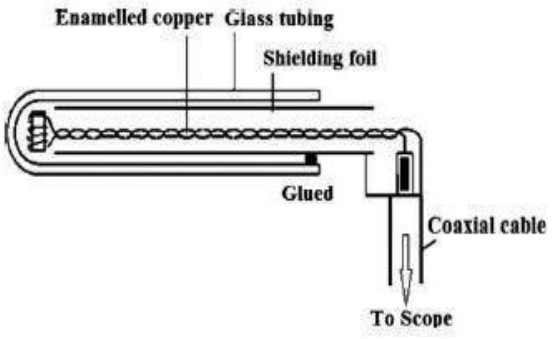

Fig 4 Construction of a magnetic probe

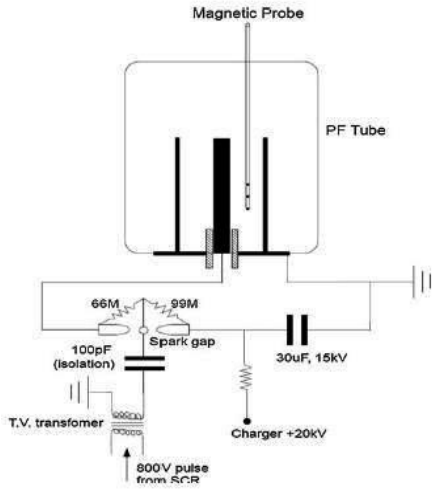

Fig 5 Showing a 3-channel magnetic probe inserted into the axial phase of INTI PF

Fig 5 shows a 3-channel magnetic probe (3 separate coils each at a different axial position along a single glass jacket) inserted into the axial phase of the INTI PF [10]. When the plasma focus is fired in the first 1 or 2 μs the current sheet sweeps past the coils arriving first at the coil closest to the starting (insulator) end, then a little later it arrives at the second coil and so on. The waveform recorded on the DSO is a function of the rate of change of magnetic field *dB/dt*. We numerically integrate each of the 3 signals and these are displayed in Fig.6 together with the current waveform [11]. From the time of arrival and the axial position of each probe the trajectory of the current sheet and speed profile are determined.

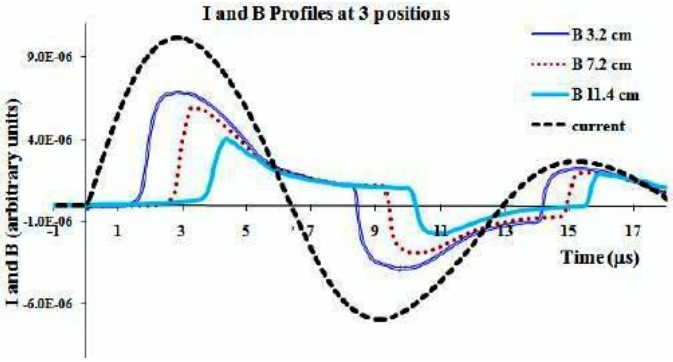

Fig 6 Integrated Signals from the 3 magnetic probes (grey, dotted brown and blue) shown together with the integrated current waveform.

From the rise time of the signal some information of the current sheet structure is also obtained. The probes are calibrated so information on the current sheet density is also available.

To present the results as shown in Fig 6 several steps have to be taken, integration and correction for baseline shift. A template has been designed so that once the raw data from the DSO (4 channels including the *dI/dt* data) is uploaded onto the template the integration and baseline shift correction are automatically done and Fig 6 is displayed.

5. SXR spectrometer and analysis system for Neon plasma

We have developed a template-based system for analyzing characteristic neon SXR (soft x-rays) from the plasma focus for yield and also for correlation studies of the SXR with pinch dynamics [3] when used in conjunction with the Lee Model code. We use a BPX65 pin diode with its glass window removed. The diode and its circuit is shown in Fig 7 with the response curves of the BPX65 (windowless, covered with different designed filters) shown in Fig 8. A 5-channel SXR spectrometer was constructed, each channel consisting of a BPX65 with a different specifically designed filter.

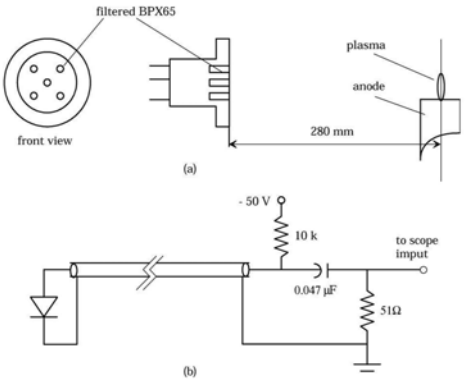

Fig 7 BPX pin diode and biasing circuit.

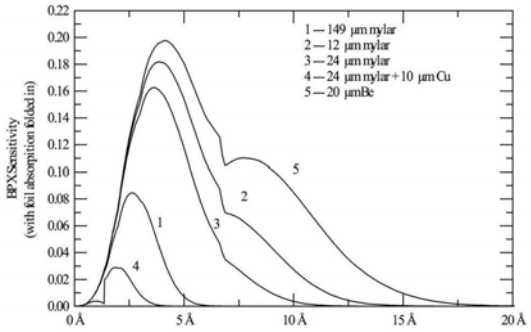

Fig 8 Response curves of BPX65 with designed filters.

For the neon studies, two channels are used; one filtered with 13 μ Al and the second with 125 μ clear mylar combined with 3 μ Al. The response (sensitivity) curves of the 2 channels are shown in Fig 9.

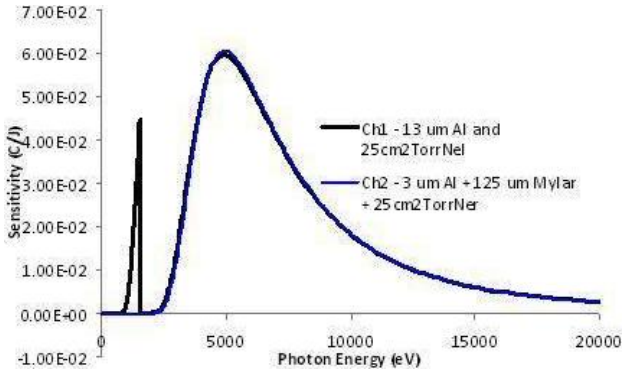

Fig 9 The two channels Ch1 and Ch2 are designed to have identical sensitivity curves for the region from around 1550 eV upwards to 20000 eV and beyond. The only difference in the two curves is that Ch1 has an additional region of sensitivity from 900 eV to 1550 eV (the spike-like feature between 0 and 2500 eV in the figure above belongs to Ch1 only). In the other spectral (or photon energy) regions the two response curves are exactly superposed, so the two curves are seen as one.

The two channels Ch1 and Ch2 are designed so that subtracting the Ch2 signal from Ch1 signal, any difference from the signals subtraction (refers to as the difference signal) then lies within the spectral window of 900 eV to 1550 eV (8-13.5 A) which is the spectral window of the characteristic neon SXR (H-like and He-like). If the neon plasma radiation incident on the two channels gives a positive difference signal, the difference signal is due to characteristic neon SXR. Its yield and time correlation may be obtained. If there is a zero difference signal and each channel does not register a signal, then there is no x-rays detected. If each channel registers a signal and there is a zero difference signal then the channels are detecting neon x-rays harder than the characteristic neon SXR. Typical results from one INTI PF shot are shown in Fig 9a. In Fig 9b, the current dip region is expanded to show correlation of focus dynamics (from the code) to the characteristic neon SXR and harder (Bremsstrahlung) neon x-rays.

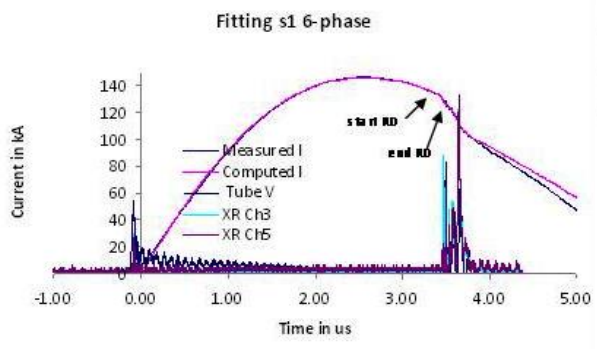

Fig 9a Current, voltage and SXR Ch1 & Ch2.

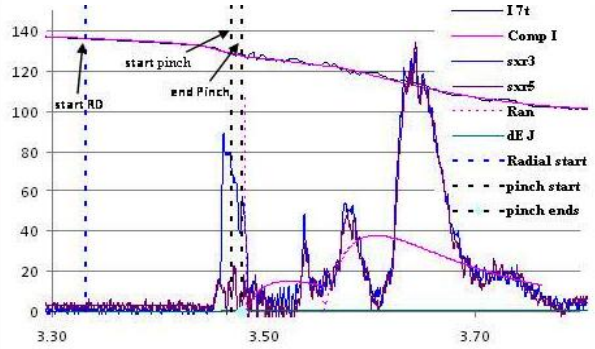

Fig 9b Current dip region is expanded to carry out fitting of computed current to measured current and also correlate pinch dynamics with characteristic neon SXR and harder neon SXR.

Fig 9b shows the crucial 200 ns region from start of radial phase through the pinch period and beyond to the anomalous resistance region modeled by the latest 6-phase Lee model code. The conclusion is that the characteristic He-like and H-like neon line SXR pulse straddles the pinch phase emitting strongly before; during; and a little after the pinch phase of the focusing action. After the pinch phase follows the anomalous resistance phase during which several harder SXR pulses are emitted of primarily non-characteristic neon SXR, possibly Bremsstrahlung.

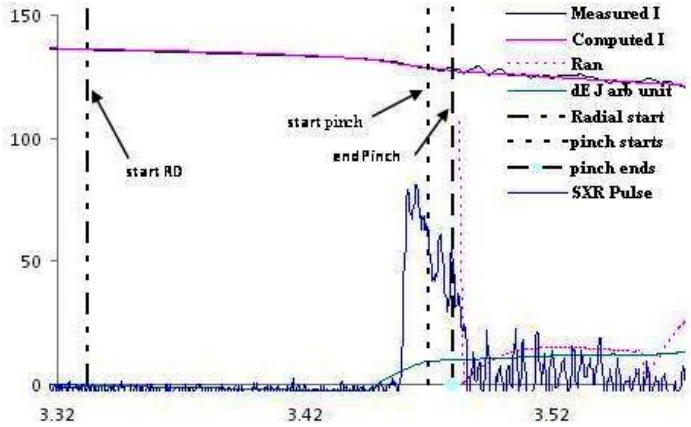

Fig 9c Expanded further covering 200 ns to show clearly the correlation of pinch dynamics with characteristic neon SXR; combining experimental results with the latest 6-phase Lee model code.

To facilitate the fitting and correlating process, a template has been developed that enables the results to be speedily displayed once the 4 data columns of *time t*, *dI/dt* and *SXR Ch1* and *SXR Ch2* are uploaded. The template integrates the data for current, SXR1 and SXR2, obtains the characteristic SXR yield. Once the current fitting is done, it displays the time positions of start of radial phase, start of pinch and end of pinch and the fitted anomalous resistance regions. This technique illustrates the advantages of integrating laboratory measurements with numerical experiments with so much more results obtained; more than the sum of the parts.

6. Scaling Laws

The important scaling properties of the plasma focus were observed in both laboratory as well as numerical experiments. The most important property is the energy (per unit mass) which appears to be a constant for all machines from very small to very large. This implies that the anode radius scales with the discharge current whilst the anode length scales as the characteristic time constant of the discharge circuit. The constancy of energy (per unit mass) also implies a constancy of dynamic resistance. These scaling properties conspire to ultimately determine the way neutron and radiation yields scale with currents and storage energies. The interplay of these simple scaling properties lead to rather more subtle non-linear scaling tendencies which have escaped the linear expectations evolved within necessarily limited laboratory measurements, limited in range and scales. However there is no such limitations with numerical experiments in range and scales. The Lee model code has built in the basic attributes of energy, mass and charge consistency; hence the scaling properties are built in as are the interplays of these scaling properties and all consequential subtle non-linear tendencies; to the extent that the continuity laws of energy, mass and charge are correctly built into the code and the configured code is connected to reality through the fitting of a reliable current trace in each shot of each machine. Then in a series of numerical experiments covering a whole range of machines, the intricacies of relationships are revealed in the compilation of the results.

We have carried out extensive systematic series of numerical experiments [12-20] with the Lee model code, integrating wherever available (but not limited by, indeed extending boldly) the results of world-wide measurements to obtain scaling laws and insights into plasma focus experiments.

Numerical experiment data of neutron yield Y_n against pinch current I_{pinch} is assembled and calibrated at one experimental point to produce a more global scaling law than available.

$Y_n = 3.2\text{x}10^{11} I_{pinch}^{4.5}$ I in MA (0.2-2.4 MA)
$Y_n = 1.8\text{x}10^{10} I_{peak}3^{.8}$ I in MA (0.3 to 5.7 MA)

Yield deterioration of energy scaling is observed:
$Y_n \sim E_0^{2.0}$ at tens of kJ whilst $Y_n \sim E_0^{0.8}$ at MJ level

The following scaling laws were obtained for characteristic SXR yield of neon plasma focus.

$Y_{sxr} = 8.3\text{x}10^3 I_{pinch}^{3.6}$ (0.07 to 1.3 MA)
$Y_{sxr} = 6\text{x}10^2 I_{peak}^{3.2}$ (0.1 to 2.4 MA),
$Y_{sxr} \sim E_0^{1.6}$ (kJ range) whilst $Y_{sxr} \sim E_0^{0.8}$ (towards MJ); evidence again of yield deterioration.

7. Determination of anomalous resistance in high inductance plasma focus from current signal

Our collaboration with several groups to standardize current measurements and to integrate numerical experiments with hardware experiments led to the observation that whilst a low inductance L_0 plasma focus has a predominant regular dip RD that is completely fitted by the code (Fig 10), a high L_0 machine has a small RD which is fitted by the code but the dip extends

into a predominant ED (extended dip) which cannot be fitted by the code (Fig 11). We classify the former as T1 the latter as T2 [21].

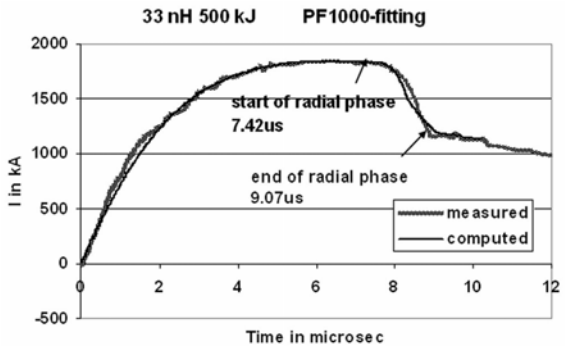

Fig 10 Type 1 PF; computed RD is completely fitted part of

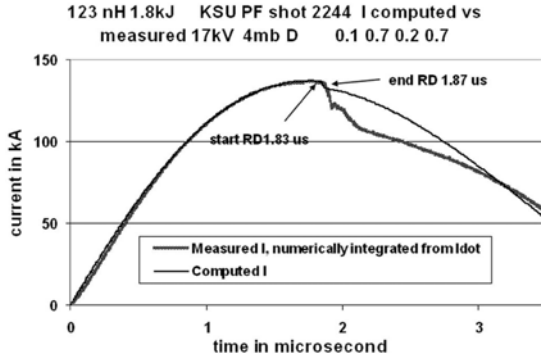

Fig 11 Type 2 PF, computed RD fits only small measured dip, which is dominated by large ED

This classification has extended the Lee model code to the 6-phase version with an additional post-pinch anomalous resistance (AR) phase, fitted AR terms with the form $R=R_0[exp(-t/t_2)-exp(-t/t_1)]$. Fig 12 shows the measured extended current dip of Fig 11 (expanded) fitted very well by the computed current dip using 3 AR terms. The fitted R_0 values are 1.0, 0.2 and 0.5 Ω respectively.

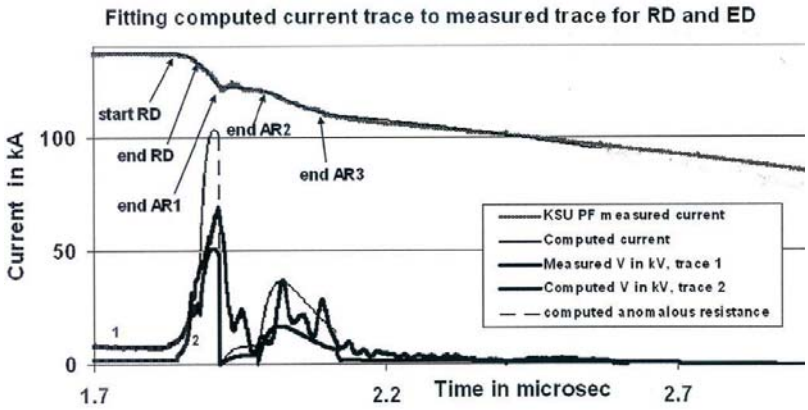

Fig 12 Computed current trace(dip region only and expanded to see details) fitted to measured current trace with inclusion of Phase 4a. Note that the computed current trace is fitted so well to the measured current trace that the two traces lie very closely on top of each other, these being the topmost traces (overlapping). Note also that the computed trace is stopped at t=2.6 μs which is beyond the end of the AR.

Such fitting provides valuable experimental data of instability processes going on during the post-pinch period. This demonstrates once more the valuable information contained in the current trace waiting to be extracted.

8. Study of pinch enhancement in plasma focus by radiation cooling

Our work with the INTI PF operating in krypton (Fig 13) shows a bigger dip with a shape characteristic of a more severe than normal compression [22]. This has stimulated renewed interest in compression enhancement using: 1) radiation collapse and 2) current-step technique.

Radiative cooling and the possibility of line radiative collapse are built into the Lee model code with the coupling of radiation rate (opposed by Joule heating rate) into the piston motion equation. Plasma self-absorption is also included in the code. Our computation (Fig 14) shows that at 0.1 Torr Kr the INTI PF operated at 12 kV starts to experience radiative cooling of a sufficient extent as to affect the dynamics. The severity of the dynamics increases until at 0.4 Torr to 1.2 torr when the compression has reached one-tenth the normal compression governed by the specific heat ratio of Kr. However it is expected that the line collapse that is modeled in the code will settle very quickly into a line of separated hot-spots. This process will be modeled in the future.

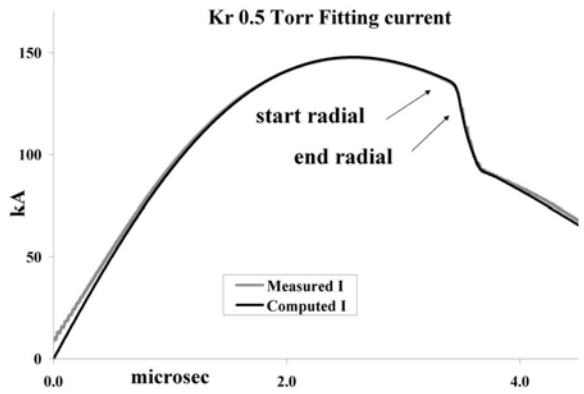

Fig 13 Measured Current trace fitted with computed trace ; INTI PF: Kr 12 kV 0.5 Torr; fitted model parameters: f_m=0.035, f_c=0.7, f_{mr}=0.09 f_{cr} = 0.7

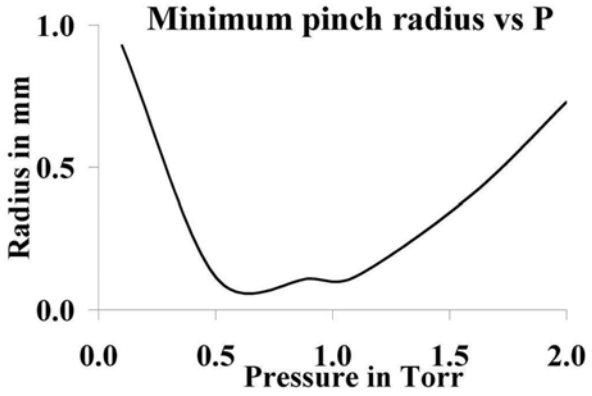

Fig 14 Computed pinch radius vs pressure INTI PF; Kr 12 kV using model parameters of Fig 13

Current-step compression enhancement is also [23] modeled in a specialized code which has been written. A second circuit (Fig 16) is added to provide a current step of shorter duration than the main discharge at a time selected by switching S2 typically at a time between the end of the axial phase and the radial phase but before the time of maximum compression.

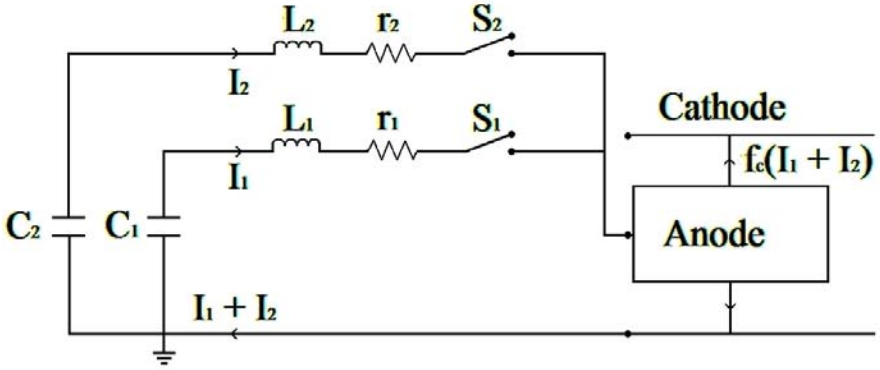

Fig 15 Plasma Focus with an additional circuit to provide a current step.

An example is selected as follows: Capacitor bank 1 (0.97MJ): L_0=36 nH, C_0=777 μF, V_0=50 kV, r_0=0.83 mΩ matched to the following PF tube combination: b=23.44 cm, a=16.86 cm, z_0=35 cm operated at P_0=10 Torr with the following model parameters: f_m=0.13, f_c=0.65, f_{mr}=0.35 and f_{cr}=0.65. Capacitor bank 2 (the current-stepping bank, 0.4MJ): L_0=10 nH, C_0=20 μF, V_0=200 kV, r_0=2.2 mΩ stepped at time during the radial phase when the piston has reached r_p=0.34 ie close to the maximum compression.

The resulting current in the pinch is shown (curve *I*) in Fig 16, showing that the current at the critical time before and during the pinch compression is significantly increased. Fig 17 shows the enhanced compression with the piston achieving a smaller radius when current-stepped. The neutron yield is increased 4-times from 2.5×10^{12} to 1.02×10^{13}. End state energy analysis shows that the enhanced compression of 1.9 times in density and the neutron yield enhancement is not so much due to the increase in current but rather due to the shift in end state of the governing energy and pressure balance.

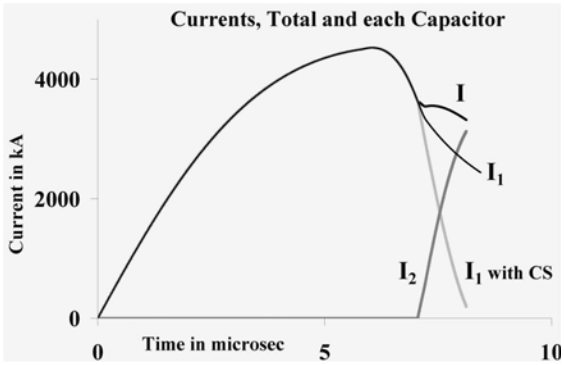

Fig 16 Comparing the current waveforms of main bank (I_1 with CS), current-step bank (I_2) and the combined current (I). Also shown for comparison is the current when the current-step is not switched on (I_1).

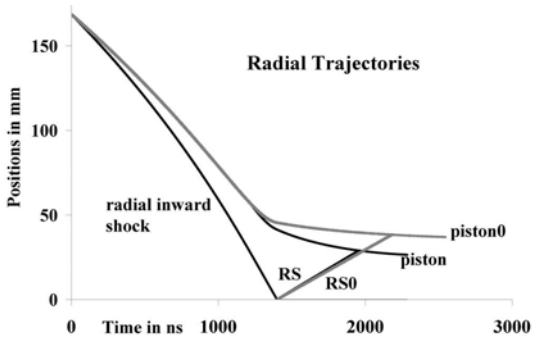

Fig 17 Comparing radial trajectories with and without current step.

9. Determination of ion beam flux of plasma focus from current signal

We have recently started numerical experiments that estimate for the INTI PF ion beam fluences of 10^{21} ions/m^2 per shot at 80 keV carrying ion energy fluence of 10^7 J/m^2 per shot with beam energy of 20 J per shot at pinch exit; together with plasma stream energy of 250 J per shot at speeds up to 50 cm/μs and anode sputtered materials carrying energy of 20J per shot (100 μg of 300 eV copper ions). These results are obtained from a combination of experiments and numerical experiments using the Universal Plasma Focus Laboratory Facility. The effect on a target placed several cm away from the anode is due to fast ion beams striking the target followed by fast axial shock waves and streaming plasma and finally by a slower moving copper jet sputtered from the anode by the action of an electron beam. Controlling these sequential effects may improve the quality of thin-film deposition or fabrication at the target. Moreover damage on the targets may be used to simulate the effect of plasmas and beams on the walls of fusion reactors.

10. Conclusion

This paper has discussed the projects that are currently being carried out at INTI International University using INTI-PF and UFLF in collaboration with IPFS, NIE-NTU Singapore; AEC Syria, AZAD University, Iran, the IAEA and ICTP. The experimental work that is carried out on the INTI PF is integrated with numerical experiments to enhance results and interpretation and in many cases the numerical experiments also integrates our experiments to experiments world-wide and to larger scale as yet non-existing experiments in order to obtain more comprehensive pictures for insights and scaling laws. Moreover recent numerical experiments enable us to obtain a more comprehensive picture on the ion beams and plasma streaming of importance to materials related applications. Materials related studies and applications using the plasma focus are expected to increase in importance as the world moves inexorably towards the dawning of the Age of Fusion Energy [24].

References

1. S.Lee, T.Y.Tou, S P Moo, M A Eissa, A V Gholap, K H Kwek et al Amer J. Phys. 1988, **56**: 62-68.
2. Saw S. H., Lee P. C. K., Rawat R. S. & Lee S *IEEE Trans on Plasma Sc*, 2009, ***37***, 1276-1282.
3. S Lee, S H Saw, R S Rawat, P Lee et al IEEE Trans on Plasma Sci **39**, No 11, 3196-3202 (2011)
4. S. Lee and S. H. Saw. Applied Physics Letters **92**, 021503 (2008)
5. S. Lee, S. H. Saw, P. C. K. Lee, R. S. Rawat and H. Schmidt. Applied Physics Letters **92**, 111501 (2008)
6. S.Lee, S.H.Saw, L..Soto, S V Springham, S P Moo. Plasma Phys Control. Fusion, **51** 075006 (2009)
7. S Lee, S H Saw, R S Rawat, P Lee et al J Fusion Energ DOI: 10.1007/s10894-011-9456-6 Online First™ 28 July 2011
8. S.Lee. (online) Radiative Dense Plasma Focus Computation Package: RADPF, 2012 http://www.plasmafocus.net
9. S H Saw, S Lee, F Roy, PL Chong, V Vengadeswaran, , et al Rev Sci Instruments (2010) **81**, 053505
10. S. H. Saw, M. Akel, P. C. K. Lee, S. T. Ong, S. N. Mohamad, F. D. Ismail, N. D.Nawi, K. Devi, R. M. Sabri, A. H. Baijan, J. Ali and S. Lee. J Fusion Energ DOI 10.1007/s10894-011-9487-z Online First™ 17 Nov 2011
11. S Lee, S H Saw, P C K Lee, R S Rawat, K Devi. Accepted for publication J Fusion Energ (2012)
12. S Lee and S H Saw. J of Fusion Energy, **27,** 292-295 (2008)
13. S Lee. Plasma Physics Controlled Fusion, **50** 10500 (2008)
14. S. Lee. Appl. Phys. Lett. **95** 151503 (2009)
15. S. Lee, R. S. Rawat, P. Lee and S. H. Saw J. Appl. Phys. **106**, 023309 (2009) (6 pages)
16. S.Lee, S.H.Saw, P.Lee and R.S.Rawat. Plasma Physics and Controlled Fusion, **51**, 105013 (8pp) (2009)
17. S. Lee. Appl. Phys. Lett. **95** 151503 (2009)
18. S H Saw and S Lee. *Energy and Power Engineering*, 2010, 65-72 doi:10.4236/epe.2010.21010,
19. S H Saw and S Lee. Int. J. Energy Res. **2011**; **35**: 81-88
20. M. Akel and S. Lee. J Fusion Energy (Online First 24 June 2011) doi:10.1007/s10894-011-9445-9
21. S Lee, S H Saw, A E Abdou and H Torreblanca. J Fusion Energy Volume **30**, Issue 4 (2011) 277-282
22. S Lee, S H Saw and Jalil Ali. In production J Fusion Energy DOI: 10.1007/s10894-012-9522-8(2012)
23. S Lee and S H Saw. In production J Fusion Energy DOI: 10.1007/s10894-012-9506-8 (2012)
24. S Lee and S H Saw. J Fusion energy **30**, 398-403 (2011)

Invited Review Paper

Industrial Applications of Plasma Focus

M. Ghoranneviss*, S. Javadi, M. Habibi, M. T. Hosseinnejad, A. Ghorbani
Plasma Physics Research Center, Science and Research Branch, Islamic Azad University, Tehran, Iran
E-mail: ghoranneviss@pprc.srbiau.ac.ir

Abstract
This paper reports the deposition of Ti, Cr and WN thin films, using a low energy (2kJ) plasma focus device. The Ti and Cr films are deposited by using axially varying distances from the anode tip and the WN films are synthesized using different numbers of plasma focus deposition shots. The structural properties have been studied using X-ray diffractometer (XRD) and the surface morphology of the deposited films has been investigated using Atomic Force Microscope (AFM). These results are justified on the basis of the energy density of ions in the PF device.

1. Introduction

The dense plasma focus (DPF) device [1,2] is a magneto-hydro-dynamic coaxial plasma accelerator, which utilizes self-generated magnetic field for efficiently compressing the gas to a high density ($n_e \sim 10^{25}$-$10^{26} m^{-3}$) and high temperature ($T_e \sim 1$-2 keV) pinched plasma for a short duration. It is an excellent source for the generation of high energy high density ions [3], relativistic electrons [4,5], X-rays [6] and neutrons [7]. The dense plasma focus was invented independently by Filippov in Russia and by Mather in USA in two different geometries. The Mather type and Filippov type geometries differ from each other on the basis of aspect ratio. The aspect ratio is less than one in the Mather type design and is greater than one in the Filippov type design. Although both the devices behave identically, the Mather type is preferred due to its simple design, convenient access to various diagnostics, distinguishable phases of current sheath dynamics. When compared with other surface modification techniques, plasma processing with dense plasma focus has several attractive features. It is an inherently dry process; the reactants are generally inexpensive gases (e.g. nitrogen, methane, oxygen, argon etc.) and the gas consumption is appreciably small as compared with that in the conventional techniques, the nitrogen ions coming from the focus region are much more energetic than the nitrogen ions present in other processing reactors, so that the specimens are heated during ion beam treatment. Plasma focus assisted modification of a few microns thick layer of a material specimen can be performed within several minutes, which represents very good time savings compared to DC pulse or RF glow discharge and plasma focus device is operated under pressure conditions which can easily be maintained. Recently, this device has been used for the deposition of thin films [8,9]. Hussain et al. [8] have successfully deposited thin films of TiN on silicon wafers using a low energy PF. Rawat et al. [9] used a 3.3 kJ plasma focus device to deposit the TiN thin films on the stainless steel substrates, In this paper, we have deposited various types of thin films on different substrates by a low energy plasma focus device. Then the deposited films are investigated structurally and morphologically by X-ray diffraction (XRD) and Atomic Force Microscopy (AFM) analysis.

2. Experimental setup

In this paper, we have used Mather type plasma focus device that constructed at Plasma Physics Research Center (PPRC) to deposit Ti, Cr and WN thin films. This device is energized by a 10 μF, 25 kV low inductance capacitor. It consists of a cylindrical copper rod that functions as an anode that is surrounded by twelve copper electrodes as a cathode. The central electrode is made of a 160 mm long and 20 mm diameter oxygen free high conductivity copper rod. Step anode is used instead of usual anode in this research. The copper anode is inserted with 7 mm long and 9 mm diameter pure metal at the top. The schematic of the system has shown in Fig 1. Argon is used as working gas to deposit Ti and Cr but nitrogen is used to deposit WN thin films; however the chamber pressure is kept at a steady 1Torr. To reach this pressure a rotary pump is used to evacuate the chamber up to 1×10^{-3} mbar, and then the working gas is injected into the chamber to increase the pressure to 1 Torr. The charging voltage is kept at 18 kV throughout the experiment. The strong focusing action is illustrated by a steep dip in the current coil signal (Tektronix TDS 2014B) from the plasma focus device. The substrates used in this experiment are high-polished $10\times10\times1$ mm^3 stainless steel-AISI 304. Before the substrates were mounted on the holder, they were cleaned in ultrasonic-bath using organic solvent. A shutter is placed between substrates and anode tip to prevent energetic ions from striking on the samples, before the strong focusing action occurs. These deposited thin films were characterized structurally with X-ray diffractometer (XRD) and surface morphologically by Atomic Force Microscope (AFM).

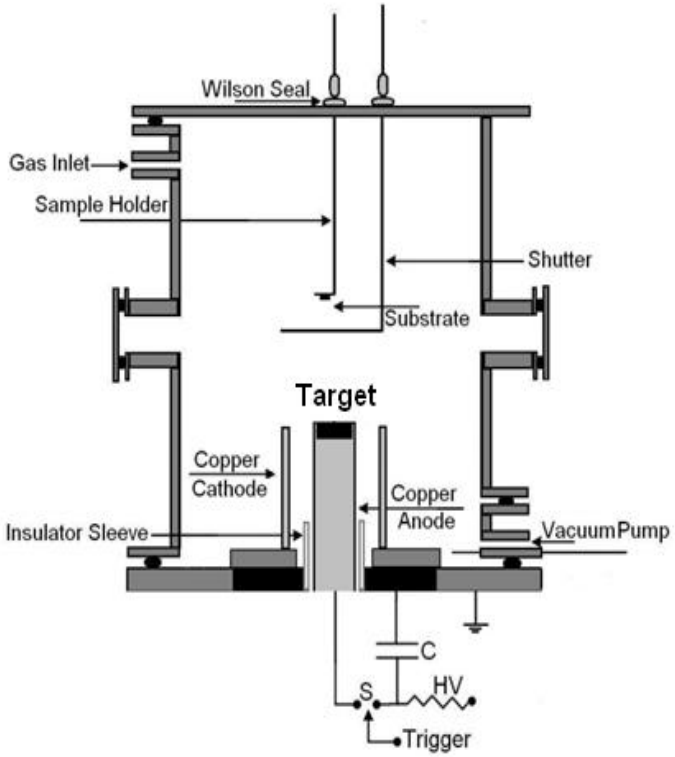

Fig 1. The schematic of plasma focus device for deposition

3. Results and Discussion

3.1.1 XRD Results

XRD Patterns of Ti films deposited at the distance of 3 cm and 5 cm from the anode tip by using constant number of focus shots (25 shots) are shown in Fig. 2. Diffraction peaks corresponding to (200), (220), (222) Ti crystalline planes are observed. With increasing the distance from 3 to 5 cm the intensity of diffraction peaks are decreased, due to decrease in ion flux [10]. At these samples because of high thickness, the peaks of stainless steel are not observed.

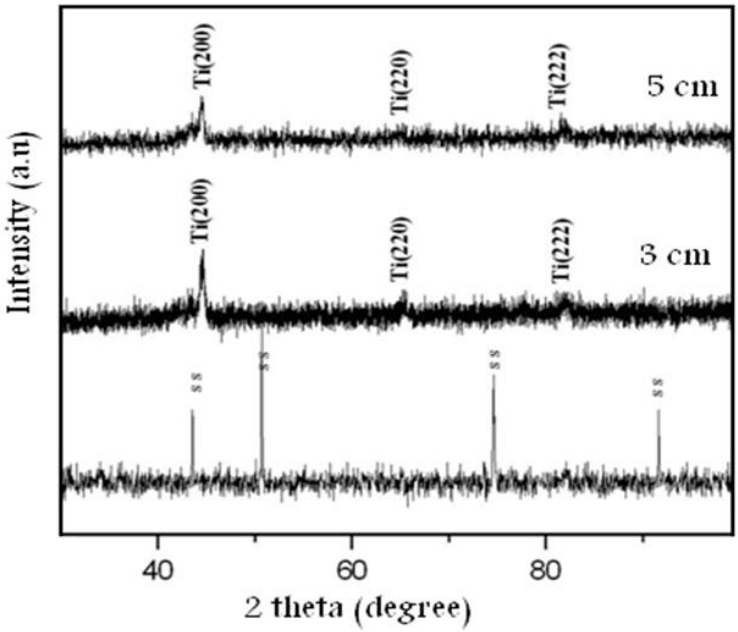

Fig 2. XRD patterns of the film deposited for 3 and 5 cm distances from the anode tip

3.1.2 AFM results

The AFM micrographs of deposited titanium thin films illustrate that deposited Ti thin film at 3 cm from top of the anode shows almost uniform and smooth surface. Also by increasing the distance from top of the anode to 5 cm, the surface are seen to compose of much bigger sized grains.

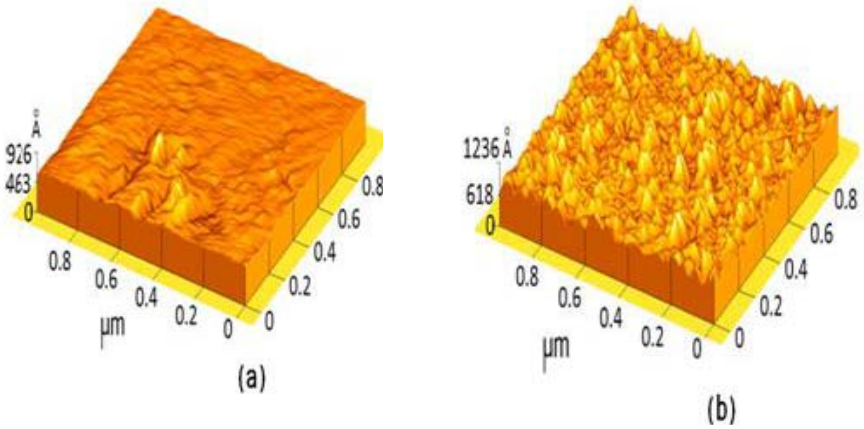

Fig 3. AFM micrographs of samples placed at (a) 3 and (b) 5 cm from the anode tip

3.2.1 XRD results

The Cr thin films deposited on stainless steel AISI-304 substrates are investigated by using X-ray diffraction (XRD) analysis. The XRD patterns of deposited chromium thin films at different axial distances from the anode tip (3 and 5 cm) by using constant number of focus shots (25 shots) are shown in Fig. 4. These patterns show that the deposited films are crystalline and have diffraction peak for (111) Cr plane. The Cr diffraction peak intensity for (111) plane at axial distance of 5 cm has increased as compared to that of 3 cm position due to good crystalinity of chromium films in this distance. The XRD patterns also show that the films at axial distance of 3 cm contain a new induced chromium-iron nickel phase [11]. Due to the high energy ions striking the substrates, stoichiometric changes occur in stainless steel substrates. For the sample placed at 5 cm distance from the anode tip, no diffraction peaks corresponding to induced chromium-iron-nickel are observed.

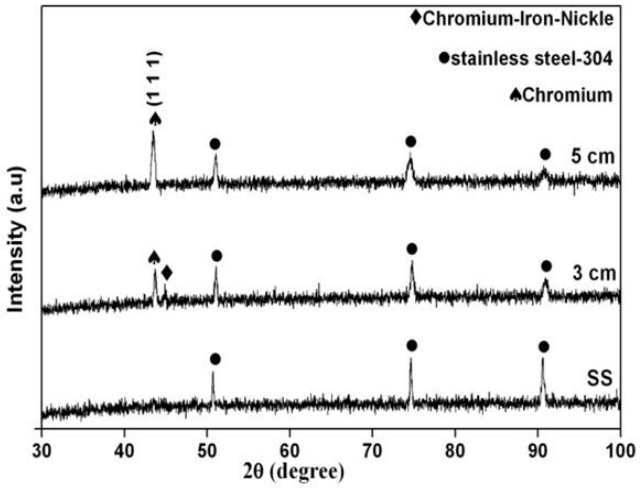

Fig 4. XRD patterns of the film deposited for 3 and 5 cm distances from the anode tip

3.2.2 AFM results

The AFM micrographs of deposited chromium thin films are shown in Fig. 5. For the sample placed at 3 cm distance from the top of the anode; the ion flux transferred more energy to the surface and damaged it. By increasing the distance to 5 cm and thus decreasing ion flux, the surface is composed of smaller sized grains and it is completely uniform with no cracks. By increasing the distance from the top of the anode thus decreasing ion flux, the transferred energy to the surface is decreased. Consequently the conglomeration of the grains is reduced.

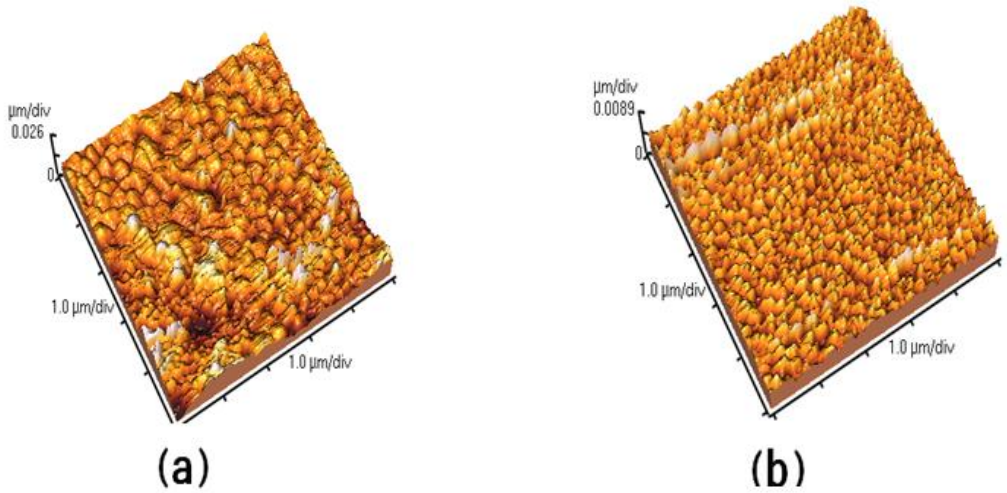

Fig 5. AFM micrographs of samples placed at (a) 3 and (b) cm distances from the anode tip

Table 1 show the roughness measurement of chromium thin films at various distances from the anode tip. These results show that by increasing the distance from top of the anode, the surface roughness is decreased.

Table 1. RMS Roughness for deposited Cr thin films at different distances from the anode tip.

Distance from the top of the anode	3 cm	5 cm
RMS Roughness (nm)	3.877	1.387

3.3.1 XRD results

Fig. 6 shows the XRD patterns of an unexposed film compared to the patterns of the films deposited with various focus shots (10, 20 and 30 shots) at 0° angular position and all 80 mm away from the anode tip.

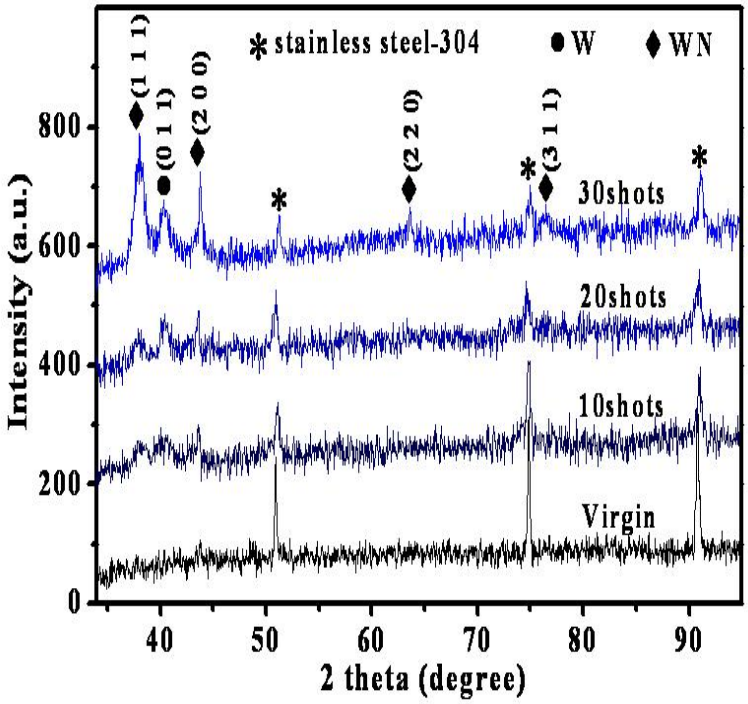

Fig 6. XRD patterns of the films deposited for 10, 20 and 30 focus shots

The results show that the WN crystalline layers deposited on stainless steel 304 substrates grow as they are exposed to more focus shots. From Fig. 6, we observe that exposition to 10 and 20 focus deposition shots results in substrate diffraction peaks as well as diffraction peaks of (111) WN, (200) WN and (011) W crystalline planes; whilst for 30 deposition shots, diffraction peaks of WN (311) and WN (220) crystalline planes also appear in the XRD patterns. These extra diffraction peaks of WN crystalline planes are the results of the proper phase induction caused by the additional focus shots. The relative locations of all W and WN diffraction peaks are consistent with the Inorganic Crystal Structure Database (ICSD). Another observation from Fig. 6 is that the intensity of WN diffraction peaks increases with the number of focus shots when 10, 20 and 30 shots are applied. This phenomenon can be explained by noticing that for the samples treated by 10, 20 and 30 focus shots, the thickness of the crystallite phase of Tungsten Nitride grows with the number of focus shots [12]. Also in Fig. 6, the intensity of the diffraction peak for the (011) W crystallite plane increases with the number of focus shots which shows a growth in Tungsten crystalline.

3.3.2 AFM results

Using the images acquired by an Atomic Force Microscope (AFM), we have analyzed the surface morphology of the films deposited with various numbers of focus shots (10, 20 and 30. shots). The images have been obtained with a scanning area of 5μm × 5μm. Fig. 7 shows an increase in the size of the deposited particles when the number of focus shots is increased from 10 to 20 and 30 shots. This growth in particle size is caused by the increased strength of the annealing of deposited layer with more focus shots.

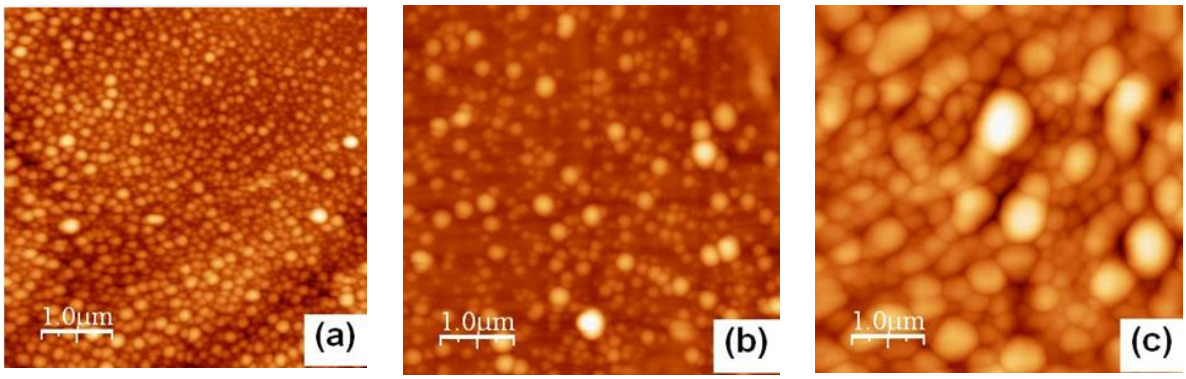

Fig 7. AFM micrographs of samples exposed to (a) 10, (b) 20 and (c) 30 shots

To analyze and compare the surface roughness of the deposited films, in each experiment, we measured the root mean square (rms) value of roughness. The recorded rms value of the roughness measurements are presented in Table 2. We observe that as the number of focus shots increase, more roughness is observed on the surface of the films.

Table 2. rms roughness for deposited WN thin films with different number of focus shots.

Number of Focus Shots	10 shots	20 shots
RMS Roughness (nm)	3.8	17.8

4. Conclusions

In this paper, we deposited Ti, Cr and WN thin films on stainless steel AISI-304 substrates by using the dense plasma focus device (2 kJ). For the Cr and Ti films we used different distances from the anode tip. We used different number of focus shots to deposit WN films. To characterize the structural properties and surface morphology of thin films we used XRD and AFM analysis, respectively. For deposited Ti films we observed (200), (220) and (222) Ti crystallization planes and by increasing the distance from the top of the anode, all the diffraction peaks of Ti are decreased. The XRD results of Cr thin films show the presence of crystallization Chromium phase. The peak intensity for (111) Cr plane is increased by increasing the distance from the top of the anode. The WN deposited films illustrate that by increasing the number of focus shots from 10 to 20 and 30; all diffraction peaks of WN are increased. Also the AFM results show that for Cr films by increasing the distance from 3 to 5 cm we observe the surface is quite uniform and crack-free, and the grain sizes are decreased. The AFM micrographs for deposited WN films show that by increasing the number of focus shots, the particle sizes are increased.

References

[1] J.W. Mather, Phys. Fluids 7 (1964) 5
[2] S. Lee, T.Y. Tou, S.P. Moo, et al., Am. J. Phys. 56 (1988) 62
[3] H. Bhuyan, H. Chaqui, M. Favre, I. Mitchell, E. Wyndham, J. Phys. D Appl. Phys. 38, 1164 (2005)
[4] L. Soto, Plasma Phys. Control Fusion 47, A361 (2005)
[5] M. Zakaullah, A. Waheed, S. Ahmad, S. Zeb, S. Hussain, Plasma Sources Sci. Technol. 12, 443 (2003)
[6] M. Shafiq, A.A. Khan, S. Hussain, M. Sharif, R. Ahmad, S.H. Bhatti, A. Waheed, M. Zakaullah, Plasma Devices Operations 12, 305 (2004)
[7] M.J. Koh, R.S. Rawat, A. Patran, T. Zhang, D. Wong, S.V. Springham, T.L. Tan, S. Lee, P. Lee, Plasma Sources Sci. Technol. 14, 12 (2005)

[8] T. Hussain, R. Ahmad, I.A. Khan, J. Siddiqui, N. Khalid, A.S. Bhatti, S. Naseem, Nucl. Instrum. Methods Phys. Res. B 267 (2009) 768–772.
[9] R.S. Rawat, W.M. Chew, P. Lee, T. White, S. Lee, Surf. Coat. Technol. 173, 276 (2003)
[10] M. Hassan, A. Qayyum, R. Ahmad, G. Murtaza, M. Zakaullah, J. Phys. D Appl. Phys. 40, 769 (2007)
[11] R.S. Rawat, P. Lee, T. White, S. Lee, Conf on Contr. Fusion and Plasma Phys. 24B, 484 (2000)
[12] R. Sagar, M.P. Srivastava, Phys. Lett. A 183 (1993) 209–213

Invited Review Paper

Plasma Focus as a Multiple Radiation Source

P LEE

Plasma Radiation Sources Laboratory, National Institute of Education, Nanyang Technological University, 1 Nanyang Walk Singapore 637616

Abstract

The plasma focus is well known for its ability to produce a copious yield of various type of radiation. This paper summarizes the attempts to measure, optimize and document the EUV, x-rays, electrons, ions and neutrons from the plasma focus devices in the plasma and radiation sources laboratory in Singapore. The plasma focus devices range from 100J-10kJ. Some highlights are the high efficiency of keV x-ray production, ~100J of x-rays from 2kJ capacitor bank energy, high neutron yield ~10^9 n short pulse ~ ns time scales, extremely high current yet low energy electron beams, beyond space charge limitations.

1. Introduction

The plasma focus was invented in the 1960s by J.W. Mather and N.V. Filipov. Research on the plasma focus was started in the 90s in Nanyang Technological University by S. Lee. The plasma focus produces a dense cylindrical plasma column called “pinch” or “focus” as a result of a large current driven in a suitable set of electrodes. When the dense plasma column is formed, the plasma focus behaves like a z-pinch where a cylinder of plasma is compressed and confined by an azimuthal magnetic field generated by an axial current. Many interesting phenomena can be observed from the pinch. This paper reviews the work done in Singapore over the last 20 years to document and understand the various radiation emitted by the plasma focus. Some possible applications have also been investigated. The plasma focus available in our laboratory is summarized in Table 1. Not all devices have been fully investigated and optimized for all possible radiation.

Machine	Energy / kJ	Current/kA
MPF, FMPF 1,2,3	0.1-0.2	50-100
UNU-ICTP	3	170
NX1	2-3	300
NX2	1-3(mostly 2)	400
NX3	10	500

Table 1. Summary of plasma focus devices at Plasma Radiation Sources Laboratory at NIE

2. Review of results from Plasma Radiation Sources Laboratory(PRSL)

The mechanism for the production of the various forms of radiation from the plasma focus is sufficiently well understood for the purpose of optimizing the device for specific applications by changing the geometry and construction of the plasma focus head system [1-5] [6-8]or gas mixture[9, 10] although much research can be done to further understand the finer details of the plasma focus.

Soft x-ray ~1-10keV is produced by the plasma focus in the pinch region and is emitted almost isotropically. X-rays are generated due to the interaction between free electrons and the ions or atoms. The main mechanism for efficient soft x-ray production is through recombination and line radiation within the dense plasma region although bremstrahlung plays a significant role when operated in low atomic number(Z) gases. In a typical x-ray tube, the kinetic energy of the electrons can be used to produce x-rays or to give energy to the atoms in the target. For soft x-rays, the probability of producing x-rays is very small, less than 0.01%, so that even if we produce the electrons with 100% efficiency, the efficiency for production of x-rays is less than 0.01%. In the case of plasma, the same low probability of producing x-rays does not imply low efficiency. Since all the plasma is at about the same temperature, electrons lose and gain energy equally through collisions with atoms in the plasma target. Therefore the efficiency of producing x-rays from plasma can be close to 100%. With the plasma focus, producing plasma from electrical energy can be as high as ~5% for a 3kJ device and may be slightly higher for higher energy devices. For reference a typical "small" synchrotron light source delivers 0.9W of 2-10keV x-rays onto a 4 inch target, source: http://ssls.nus.edu.sg/facility/limint.html.

The results [11-16] from various devices are summarized in Table 2.

Machine	Gas	Photon energy/ keV	Yield Per shot/ J	Projected X-ray power at 8kW input/W	Wall Plug efficiency /%
FMPF	D2	~1	0.1	4	0.05
UNU-ICTP	Ne	~1	6	16	0.2
NX1	Ne	~1	100	260	4
NX2	Ne	~1	80	320	4
NX2	Ar	~4	0.3	1.2	0.02

Table 2. Summary of x-ray yield from various devices.

Possible applications for the soft x-rays are microlithography[17, 18], micromachining [19], micro-radiography[20]. The plasma focus is particularly suitable to be used as a soft x-ray source due to the particular matching of the temperature to the x-ray photon energy thus giving rise to a high efficiency as compared to traditional x-ray tubes. The average ~1keV x-ray power from the dense plasma focus also far exceeds that of small synchrotron sources. For micro-radiography, the dense plasma focus has the ability to expose film within 1 shot ~ 10 ns such that there is no motion blurring of radiographs e.g compare blurred photographs of moving people without flash and clear ones with flash. Furthermore the cylindrical geometry of the plasma gives

a small circular source end-on. A small circular source avoids penumbral blurring e.g. compare the blurred shadow from a fluorescent ring tube as compare to the clear shadow from a small bulb.

Fast Electrons are produced in the plasma focus due to the generation of high electric fields in the plasma focus related to the fast changing magnetic field. The particular advantage of generating the electrons in a plasma focus is the possibility for extremely high currents to be generated in a short time duration as compared to a typical field or thermionic emission cathode in a vacuum tube. This is due to two main points. Firstly, the fact that there is no lack of electrons from the plasma source where almost every atom has been ionized. Furthermore the electrons stream within a plasma so the space charge effects which normally places and limits on the maximum current due to the electrons repulsion of each electron is reduced as the plasma shields the electrons from each other.

We have reported that high energy electron beams are produced from the plasma focus. A spectral analysis [21] shows that there are electrons with tens of keV to hundreds of keV. High energy electron spectrum may show peaks indicative of an accelerating mechanism like a LINAC or cyclotron where electrons move through several accelerating regions while the overall potential difference across the device may remain below the value expected from the maximum electron energy. We have also reported [21, 22] that the electrons beam is affected by the use of different gasses. And medium energy x-ray data allows us to infer that the e-beam energy can be tuned using different gasses as well.

Possible applications that have been investigated by us are flash electron lithography [23], materials ablation [22]. We currently are also investigating the possibility of materials testing one example of which is the testing of possible wall materials in tokamaks which may be subject to intense radiation. This work is supported by a grant from the International Atomic Energy Agency(IAEA).

Medium energy x-rays ~10-100keV are produced in the plasma focus by electron bombardment of the anode and is thus related to the electron measurements. The efficiency of medium energy x-rays is not significantly different from conventional x-ray tubes but due to the extremely high currents, it is possible to produce a large number of medium energy x-ray photons in a short pulse.

We have reported that medium energy x-rays are emitted over the surface of the anode[24]. This suggests that the mechanism is an electron beam bombarding the anode material. This makes it possible to tune the x-ray energy by using different materials as anode or as inserts in the anode including non-conducting materials. Non-conducting materials cannot be used in conventional x-ray tubes. However due to the presence of a plasma, current flow can occur on the material surface.

Possible applications that have been investigated by us as student projects are: radiography of “soft” materials, high speed video radiography. These applications are possible due to a high peak power where single shots can produce good images. This avoids motion blurring and thus makes it possible to take radiographs of moving objects.

Hard x-rays ~0.1-10MeV are also produced by electron bombardment of anode. For such high energies, there is no advantage in terms of efficiency and pulse duration in comparison with high voltage pulsed x-ray tubes as space limitations are not very restrictive at very high voltages. However the plasma focus device [25] can be made considerably simpler and smaller than equivalent conventional devices which require ~MV high voltage generators as the accelerating voltages are self generated within the plasma and therefore does not present insulation

difficulties. Furthermore hard x-rays are produced just before neutrons and may be used in dual X-ray and neutron radiography applications. Dual X-ray and neutron radiography may be useful to detect illicit materials as it can show the forms of both high –Z heavy metals and low-Z hydrogen containing compounds clearly.

Extreme Ultraviolet can be produced during the pinch as well as before and after. As plasma focus optimised for neutrons and x-rays operate at a much higher plasma temperature than is efficient for EUV production, some additional work may be required to understand how to operate the plasma focus at lower speeds and temperature to enhance EUV yield. It may be possible to puff in a gas in the pinch region to reduce the temperature while enhancing source density while maintaining ambient gas pressure to avoid re absorption. Another possibility is to maintain an external magnetic field. This will reduce compression and thus temperature and simultaneously improve stability of the plasma column. Enhancing in band radiation rate and prolonging radiation duration. Initial work done and reported in S.M Hassan's PhD thesis shows that fairly high EUV yields may be produced by a miniature plasma focus even without clear signs of the traditional focus event.

Fast Ions can be produced for the same reason as fast electrons, by the self generated electric fields in the plasma. There are some important differences, in that the ions are slower due to their higher mass. Measurements of deuterium ions in NX2 show that there is significant number of ions in the 100keV range. This implies that either the electric fields must exist for more than ~ 10ns for the ions to gain the energy within the length of the plasma or that the electric fields are much higher. In addition fast ions may also be produced by nuclear reactions [26-28]. For example D-D reactions produce mono-energetic protons in addition to mono-energetic neutrons. Fast ions may be used to produce neutrons and isotopes which will be discussed later. The low-medium energy ions have been investigated using Faraday cups and the highest energy ions by nuclear track detectors and activation methods [29-31]. Applications for materials testing has also been reported [32]

Neutrons can be produced when the plasma focus is with an appropriate gas. Typically deuterium is used to produce mono-energetic 2.5 MeV neutrons. It is possible to obtain neutrons using other gases. Some examples are deuterium–tritium(DT) mixture, or hydrogen, with lithium target. Using DT mixture will produce 100x more neutrons and each neutron be 13MeV instead of 2.5MeV. We have investigated the plasma focus as a neutron source [33-39] using DD and the yields are summarized in table 3. For reference the record yield per shot from the national ignition facility (NIF) is 3×10^{14} neutrons per shot with 121kJ of laser light using DT mixture source: https://www.llnl.gov/news/newsreleases/2010/Nov/NR-10-11-02.html. With an input power of ~8kW, the shot rate for NIF would be about one shot per 1000s and correcting for DD instead of DT NIF would produce 3×10^9 DD neutrons per second.

Machine	Yield Neutrons/shot	Projected yield rate at 8kW input power Neutrons/s
FMPF3	10^6	4×10^7
UNU-ICTP	10^8	2×10^8
NX2	10^8	4×10^8
NX3	10^9	8×10^9

Table 3. Summary of DD neutron yield from various plasma focus devices in Singapore.

Short Half-life Isotopes may be produced when appropriate targets are placed in front of the fast ion beam. We have investigated the production of short lived isotopes with possible application in PET [40]. The results are promising in that a 3kJ device properly engineered can produce sufficient activity for clinical use.

3. Discussion and Conclusion

For the purpose of using the plasma focus as a radiation source, there are a number of advantages listed below:

- Elegance and simplicity
- High efficiency
- Short pulse, high brightness
- Possibility of more than 1 type of radiation at the same time.

Not all advantages are important for all applications. Neither is it available for all types of radiation.

Proposals for the future:

1) Scaling of radiation yield (scientific): The scaling of neutron yield and soft x-ray yield is very well described by the Lee model. The neutron scaling being based on beam target mechanism implies that the scaling for ion production can also be well described by the Lee model and thus also the short lived isotope productions as well as e-beam and hard x-ray generation. There is little comparable experimental data for various machines to confirm this. This would thus make a good project to investigate and confirm the mechanisms of the other radiations
2) Plasma and fusion studies (scientific): The International Center for Dense Magnetised Plasmas(ICDMP) houses the world's largest non-military plasma focus for scientific research. The multi mega-amp megajoule plasma focus, PF1000, has been operational for the last decade. Several issues have already been investigated and understood. One example of which is the effect of "neutron yield saturation". With more modern technology, it is interesting to propose a new facility to investigate scaling beyond megajoule. It would be interesting to study plasmas with sufficiently high energy comparable to the National Ignition Facility's (NIF) 2 megajoule laser, with possible outcomes of proposing new fusion energy schemes which so far is dominated by tokamaks (ITER) and laser fusion (NIF). A 10 megajoule plasma focus facility would

cost significantly less than an equivalent laser fusion facility, yet be able to deliver 2 megajoule on target. In addition the research can be used to understand plasma wall interactions and neutron wall interactions, both of which cannot be studied well on actual current laser fusion facilities and tokamaks as they do not give sufficient flux comparable to that expected for future fusion power sources. The new facility should at the same time have several small dense plasma focus devices for scientific experiments for example to try out novel electrode geometries, pulsed power drivers and novel fuels.

3) Development of nuclear coursework without a nuclear reactor (educational/ commercial): Nuclear medicine, nuclear engineering and nuclear physics in general have great relevance in society. Many countries need to make decisions to either build or dismantle nuclear power plants, both with implications which are not easily understood without significant background knowledge of nuclear science. The decision to build is particularly difficult as there are no local experts with significant knowledge of nuclear science. Using the plasma focus as a multiple radiation source, one could design experiments for a laboratory based module for nuclear medicine, nuclear engineering and nuclear (fission/fusion) physics. Some examples are listed:
    - Proportional counter basics
    - Photomultiplier basics
    - Scintillator basics
    - Measuring the half life of neutron activated silver/indium..etc
    - Neutron attenuation using various materials
    - Hard x-ray attenuation using various materials
    - Gamma spectroscopy
    - Neutron activation analysis
    - Measurement of neutron energies using time of flight method.
    - Finding the optimum moderator size for neutron detector
    - Using Monte Carlo codes to calculate detector efficiency
    - Space resolved positron detection
    - Using CR39 for detection of charged particles
    - Neutron induced nuclear reactions

The dense plasma focus still has many areas open for investigation. At the same time sufficient work has been done on the plasma focus as a multiple radiation source for us to say confidently that it will be possible to build plasma focus devices which operates reliably and consistently enough as a tool for education and research.

Acknowledgements

This paper reviews the work done on the plasma focus since 1991 in Singapore. The author would like to thank all staff, students and collaborators who have contributed to the data and results

References

[1] Rawat, R.S., et al., Effect of insulator sleeve length on soft x-ray emission from a neon-filled plasma focus device. Plasma Sources Science & Technology, 2004. **13**(4): p. 569-575.
[2] Koh, J.M., et al., Optimization of the high pressure operation regime for enhanced neutron yield in a plasma focus device. Plasma Sources Science & Technology, 2005. **14**(1): p. 12-18.
[3] Zhang, T., et al., Current sheath curvature correlation with the neon soft x-ray emission from plasma focus device. Plasma Sources Science & Technology, 2005. **14**(2): p. 368-374.
[4] Malik, F., et al. Effect of anode shapes on neutron emission from a repetitive plasma focus device. in 16th IEEE International Pulsed Power Conference. 2007. Albuquerque, NM.
[5] Mohanty, S.R., et al., Effect of anode designs on ion emission characteristics of a plasma focus device. Japanese Journal of Applied Physics Part 1-Regular Papers Brief Communications & Review Papers, 2007. 46(5A): p. 3039-3044.
[6] Zhang, T., et al., Optimization of a plasma focus device as an electron beam source for thin film deposition. Plasma Sources Science & Technology, 2007. 16(2): p. 250-256.
[7] Mohammadi, M.A., et al., The effect of anode shape on neon soft x-ray emissions and current sheath configuration in plasma focus device. Journal of Physics D-Applied Physics, 2009. 42(4).
[8] Verma, R., et al., Effect of cathode structure on neutron yield performance of a miniature plasma focus device. Physics Letters A, 2009. 373(30): p. 2568-2571.
[9] Verma, R., et al., Order of magnitude enhancement in neutron emission with deuterium-krypton admixture operation in miniature plasma focus device. Applied Physics Letters, 2008. 93(10).
[10] Verma, R., et al., Order of magnitude enhancement in x-ray yield at low pressure deuterium-krypton admixture operation in miniature plasma focus device. Applied Physics Letters, 2008. 92(1).
[11] Lee, S., et al. Compact plasma focus soft x-ray source with high repetition and high intensity. in Conference on Microlithographic Techniques in IC Fabrication. 1997. Singapore, Singapore.
[12] Lee, S., et al., High rep rate high performance plasma focus as a powerful radiation source. Ieee Transactions on Plasma Science, 1998. 26(4): p. 1119-1126.
[13] Gribkov, V.A., et al., Operation of NX2 dense plasma focus device with argon filling as a possible radiation source for micro-machining. Ieee Transactions on Plasma Science, 2002. 30(3): p. 1331-1338.
[14] Wong, D., et al., Soft X-ray optimization studies on a dense plasma focus device operated in neon and argon in repetitive mode. Ieee Transactions on Plasma Science, 2004. 32(6): p. 2227-2235.
[15] Wong, D., et al. Repetitive operation of a dense plasma soft X-ray source for micromachining. in 6th International Conference on Dense Z-Pinches. 2005. Oxford, ENGLAND.
[16] Lee, S., et al., Soft x-ray yield from NX2 plasma focus. Journal of Applied Physics, 2009. **106**(2).
[17] Bogolyubov, E.P., et al., A powerful soft X-ray source for X-ray lithography based on plasma focusing. Physica Scripta, 1998. **57**(4): p. 488-494.
[18] Lee, S., et al. High energy photon lithography for fabrication of photonic device. in SPIE Conference on Photonics Technology into the 21st Century - Semiconductors, Microstructures, and Nanostructures. 1999. Singapore, Singapore.
[19] Kudryashov, V. and P. Lee. Deep x-ray lithography for MEMS photoelectron exposure of the upper and bottom resist layers. in International MEMS Workshop. 2001. Singapore, Singapore.
[20] Rawat, R.S., et al., Soft X-ray imaging using a neon filled plasma focus X-ray source. Journal of Fusion Energy, 2004. **23**(1): p. 49-53.
[21] Patran, A., et al., Spectral study of the electron beam emitted from a 3 kJ plasma focus. Plasma Sources Science & Technology, 2005. **14**(3): p. 549-560.
[22] Zhang, T., et al. Electron beam emission characteristics from plasma focus devices. in 6th International Conference on Dense Z-Pinches. 2005. Oxford, ENGLAND.

[23] Lee, P., et al. Lithography using a compact plasma focus electron source. in Conference on Microlithographic Techniques in IC Fabrication. 1997. Singapore, Singapore.
[24] S. M. Hassan, T.Z., D. Wong, H. M. Saw, M. W. C. Yap Wan, K. L. Long, Y. R. I. Lim, and R.S.R. J. H. Low, A. Patran, S. V. Springham, T. L. Tan and P. Lee, Spatially and spectrally resolved hard x-ray camera for dense plasma focus diagnosis. Jurnal Fizik Malaysia, 2005. **26**(3 & 4): p. 153-155.
[25] Verma, R., et al., Miniature Plasma Focus Device as a Compact Hard X-Ray Source for Fast Radiography Applications. Ieee Transactions on Plasma Science, 2010. **38**(4): p. 652-657.
[26] Springham, S.V., et al. Fusion reactions in a plasma focus operated with He-3-D-2 and He-4-D-2 gas mixtures. in 5th International Workshop and Summer School on Plasma Physics. 2005. Poland.
[27] Springham, S.V., et al. Studies of fusion protons from a He-3-D-2 plasma focus using nuclear track detectors. in 16th IAEA Technical Meeting on Research Using Small Fusion Devices. 2005. Mexico City, MEXICO.
[28] Springham, S.V., et al. D(He-3,p)He-4 and D(d,P)H-3 fusion in a small plasma focus operated in a deuterium helium-3 gas mixture. in 2nd Meeting on Dense Magnetized Plasma. 2005. Kudowa Zdroj, POLAND.
[29] Roshan, M.V., et al., Intense deuteron beam investigation by activation yield-ratio technique. Physics Letters A, 2009. **373**(41): p. 3771-3774.
[30] Roshan, M.V., et al., Nuclear activation measurements of High energy deuterons from a small plasma focus. Physics Letters A, 2009. **373**(8-9): p. 851-855.
[31] Roshan, M.V., et al., Magnetic spectrometry of high energy deuteron beams from pulsed plasma system. Plasma Physics and Controlled Fusion, 2010. **52**(8).
[32] Roshan, M.V., et al., High energy ions and energetic plasma irradiation effects on aluminum in a Filippov-type plasma focus. Applied Surface Science, 2008. **255**(5): p. 2461-2465.
[33] Rafique, M.S., et al. On the dependence of the plasma focus neutron yield on the forward-emitted fast deuteron population. in 20th Symposium on Plasma Physics and Technology. 2002. Prague, Czech Republic.
[34] Springham, S.V., et al., Imaging of fusion protons from a 3 kJ deuterium plasma focus. Japanese Journal of Applied Physics Part 1-Regular Papers Short Notes & Review Papers, 2005. **44**(6A): p. 4117-4121.
[35] Roshan, M.V., et al., Neutron and high energy deuteron anisotropy investigations in plasma focus device. Physics of Plasmas, 2009. **16**(5).
[36] Verma, R., et al., Experimental study of neutron emission characteristics in a compact sub-kilojoule range miniature plasma focus device. Plasma Physics and Controlled Fusion, 2009. **51**(7).
[37] Verma, R., et al., Realization of enhancement in time averaged neutron yield by using repetitive miniature plasma focus device as pulsed neutron source. Journal of Physics D-Applied Physics, 2009. **42**(23).
[38] Roshan, M.V., et al., Absolute measurements of fast neutrons using yttrium. Review of Scientific Instruments, 2010. **81**(8).
[39] Talebitaher, A., et al., Beryllium neutron activation detector for pulsed DD fusion sources. Nuclear Instruments & Methods in Physics Research Section a-Accelerators Spectrometers Detectors and Associated Equipment, 2011. **659**(1): p. 361-367.
[40] Roshan, M.V., et al., Short-Lived PET Radioisotope Production in a Small Plasma Focus Device. Ieee Transactions on Plasma Science, 2010. **38**(12): p. 3393-3397.

Invited Review Paper

Dense Plasma Focus: Novel Tool for Plasma Nanotechnology

R. S. Rawat

Natural Sciences and Science Education, National Institute of Education, Nanyang Technology University, Singapore 637616

Abstract

This paper critically reviews the application of dense plasma focus device as a novel source of pulsed high energy density pinch plasmas along with instability accelerated energetic ion beams for nanophase material synthesis; particularly for hard tribological coatings and magnetically hard nanoparticle thin films with possible applications in high density magnetic data storage. The plasma focus device, a non-cylindrical z-pinch device, being a multiple radiation source of ions, electron, soft and hard x-rays, and neutrons, has routinely been used for several applications such as lithography, radiography, imaging, activation analysis, radioisotopes production and more recently for material processing and thin films depositions. The key features and traits of plasma focus device are critically discussed to understand the novelties, opportunities and mechanisms of processing and synthesis of nanophase material synthesis. The results of various experimental investigations (i) for synthesis of nanostructured hard coatings, (ii) the modification of various physical properties of PLD grown thin films of FePt by energetic ion exposure in plasma focus device and (iii) the deposition of nanostructured CoPt thin films in plasma focus device are reviewed.

1. Introduction

The plasma focus device is a non-cylindrical z-pinch device which belongs to the category of pulsed-power devices where high current electrical discharge efficiently heat and compress the plasmas in a pinched plasma column. The Dense Plasma Focus (DPF) device was developed independently in variant forms by J. W. Mather in US [1] and by Filippov et al. in erstwhile USSR [2] during 1960s. It involves a powerful electrical discharge at the closed end of a coaxial electrode system following current sheath formation and acceleration in axial phase during which the magnetic energy is stored behind a moving current sheath and finally the pumping of this energy into pinched plasma column during the rapid radial collapse phase. This results in production of short duration (~10 to 50 ns), high temperature (~1 keV) and high density plasma (~10^{19} cm^{-3}). This hot dense plasma is a rich source of energetic and multiple radiations like relativistic electrons, soft/hard X-rays, fast ions and neutrons [3]. The energy density parameter, which is defined as the ratio of the electrical energy stored in the device to the volume of cylindrical pinched plasma column at the radial collapse of various dense plasma focus devices, are reported to be in the range of (1.2-9.5) $\times 10^{10}$ J/m^3 [4] making it a high energy density plasma facility.

The DPF attracted much attention from the scientific community during the 1960s as it was considered as an efficient fusion device, producing an intense burst of neutrons when operated with Deuterium/ Deuterium-Tritium as filling gas. The essential problem to be resolved in DPF research has always been to discover the physics, which dominates the neutron yield limitation/saturation at higher bank energies [5]. It has been commonly accepted that the neutrons are not of purely thermonuclear origin rather they are mainly due to beam target mechanism [6]. The better physical understanding and viability of other fusion technologies such

as tokamaks and high-power laser driven fusion experiments downgraded the importance of plasma focus devices as controlled thermonuclear fusion device. But nevertheless, this device was soon recognized as a powerful and compact source of energetic radiations producing fast neutrons, intense X-rays, energetic ions and electrons. These intrinsic, energetic and abundant multiple radiations from the plasma focus device set it apart from other devices as a prime candidate for various applications, such as (i) a neutron source for pulsed activation analysis [7], (ii) an X-ray source for lithography, radiography and imaging [8] (iii) an electron beam source microlithography [9] and (iv) an energetic ion source for short lived radioisotope production [10].

The most important and extensive use of DPF device, in the recent time however, is the increasing applications of instability generated energetic pulses of ions and electrons from this device for the modification/processing of bulk and thin film materials and the deposition/synthesis of various thin films. This paper reviews the application of plasma focus device, as one of the novel high energy density plasma processing tools offering extremely non-equilibrium conditions, in emerging field of plasma nanoscience and nanotechnology for the synthesis of nanostructured materials such as nanoparticles, nanoclusters or nanoparticle agglomerates, specifically of magnetic materials and hard coatings.

2. Dense Plasma Focus: Principle of Operation, Key Characteristics & Applications

The plasma focus is a simple device with complex physical phenomena and multiple dynamic processes. This section provides the details of: (i) brief description of the physical layout, operational principle, and key characteristics of DPF device, (ii) characteristics of hot dense pinch plasma and energetic charged particle of interest in DPF device and (iv) applications of this device for bulk/thin film processing and/or synthesis.

2.1 Physical Layout, Operational Principle and Key Characteristics of DPF Device

The schematic of the high performance 3.2 kJ (28.8 μf, 450 kA @ 15 kV) repetitive NX2 DPF at Plasma Radiation Source Lab (PRSL) of Nanyang Technological University, Singapore, depicting the physical layout and the key subcomponents, is shown in figure 1. A central anode surrounded by multiple cathode rods forms a coaxial system which is closed and electrically insulated at one end and open at the other end. The electrode assembly is placed inside a vacuum chamber. The central electrode (*i.e.* anode) of this device is connected to the high voltage terminal of an energy storage capacitor or capacitor bank through a low inductance fast high current switch and the outer electrode (*i.e.* cathode) is grounded. The NX2 is a 4-module system with 4 capacitor banks (each having 12 capacitors of 0.6 μF) with each capacitor bank connected to the DPF, as a load, through 4 pseudo spark gap (PSG) switches which are synchronously activated through a master trigger system as shown in figure 1. The other plasma focus systems housed at Plasma Radiation Source Laboratory, NIE/NTU, Singapore are two units of 3.0 kJ UNU-ICTP (United Nations University – International Centre for Theoretical Physics) plasma focus facility, two units of 200 J Fast Miniature Plasma Focus (FMPF-1 & FMPF-3) and a 20 kJ NX-3 plasma focus device.

The operational principle and plasma dynamics in DPF device is as follows: when the electrical energy stored in the capacitor bank is rapidly transferred to the electrodes by means of a fast switch; an electrical over-volt filamentary discharge is initiated across the insulator sleeve at the closed end of the electrode assembly which rapidly develops into a sheath of plasma, which evolves axially along the electrode assembly under the effect of $\vec{J} \times \vec{B}$ force. Due to this Lorentz

force action, the conducting plasma sheath accelerates towards the open end of electrode assembly *i.e.* from position 1 through position 2 shown in figure 2. In the final phase (*i.e.* from position 3 to position 4), the sheath collapses on axis with a zippering action forming the pinch plasma column. The pinch has duration of a few to several tens of nanoseconds. The pinch column then disrupts due to the growth of the $m = 0$ mode instabilities in the pinch, or from radiative collapse. The $m = 0$ mode instabilities enhances the induced electric field locally, which, coupled with the magnetic field, breaks the focused plasma column by accelerating the ions of the filling gas species, to very high energies, towards the top of the chamber and electrons to relativistic energies (100 keV and above) towards the positively charged anode.

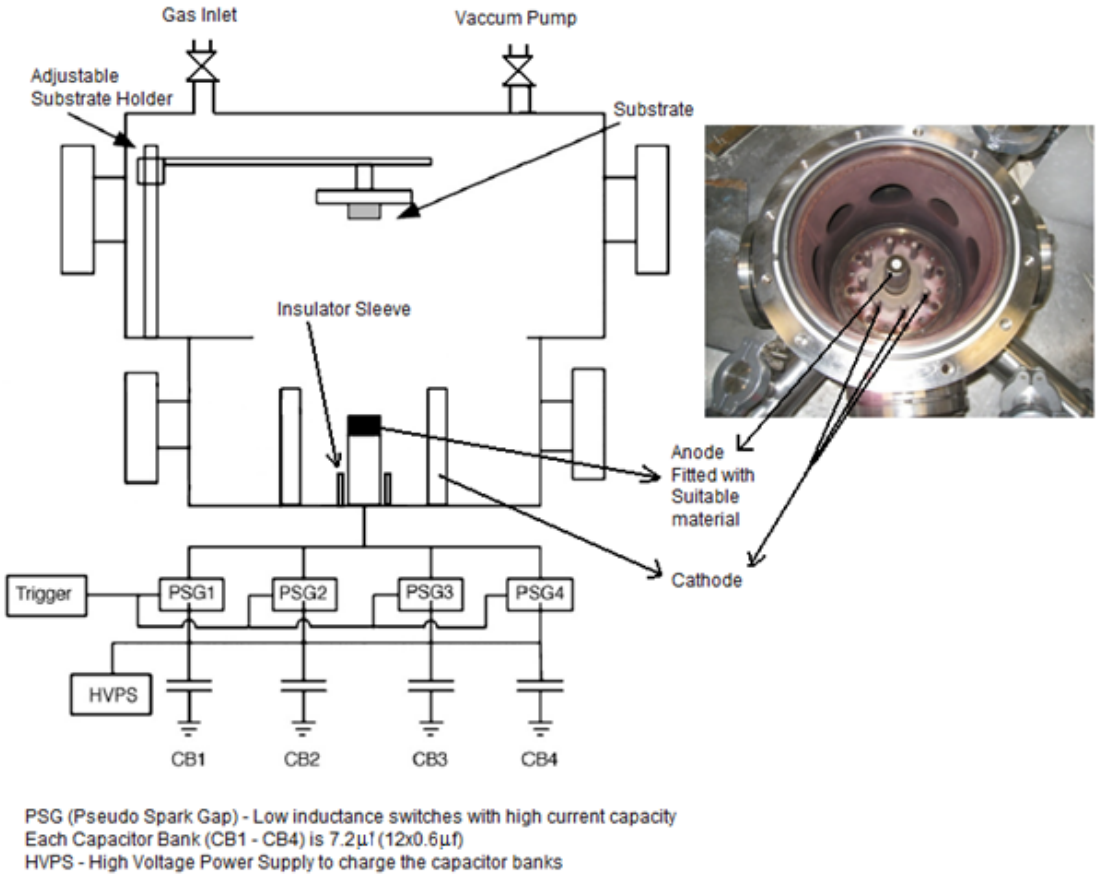

Fig 1. The schematic of NX2 dense plasma focus device with key physical components: (i) the coaxial electrode assembly, (ii) vacuum chamber housing the electrode assembly and the adjustable substrate holder, (iii) pseudo spark gap switches and the triggering module to transfer the electrical energy from capacitor banks to the electrode assembly, (iv) the 4-module capacitor bank and (v) high voltage power supply to charge the capacitor bank..

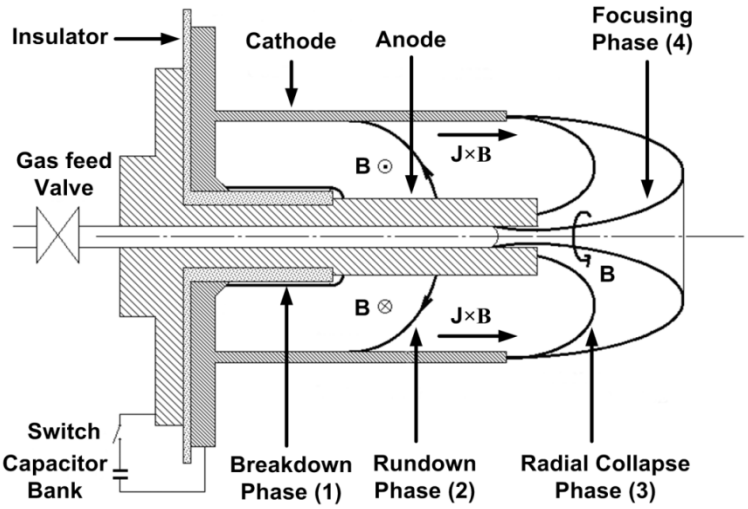

Fig 2. Current sheath dynamics under various phases of plasma focus operation.

2.2 Characteristics of Pinch Plasma and Energetic Charged Particles in DPF device

Irrespective of configuration, the typical parameters of pinch plasma, current sheath dynamics and energetic charged particle characteristics for a wide energy range of plasma focus devices are:

(i) pinch plasma electron/ion densities [11]: $5 \times 10^{24} - 10^{26}$ m^{-3},
(ii) pinch plasma electron temperatures [12]: 200 eV – 2 keV,
(iii) ion temperatures of pinch plasmas [11]: 300 eV – 1.5 keV,
(iv) energies of instability accelerated electrons [12] – tens of keV to few hundreds of keV and
(v) energies of instability accelerated ions [13]- tens of keV to few MeV.

The DPF is a pulsed plasma device and the durations of pinch plasma and energetic particles are of the order of tens of ns to about hundred or several hundred ns. The high energy density plasmas combined with intense flux of instability accelerated charged particles in DPF devices offers a kind of plasma that is very different from other conventionally used low temperature plasmas in plasma-nanoscience for plasma-aided nanofabrications [14].

2.3 DPF Devices for Material Processing and Synthesis: Mechanism and Applications

The first ever application of DPF device for (i) processing of bulk material was reported by Feugeas et al. [15] by nitrogen ion implantation in AISI 304 stainless steel, (ii) processing of thin film was reported by Rawat et al. [16] through crystallization of amorphous lead zirconate titanate thin film by single shot energetic argon ion exposure, and (iii) deposition of thin film, of carbon, was reported by Kant et al. [17].

It may be noted that the materials related work from DPF device can be classified into two broad categories: (i) processing of bulk or thin film target materials by the complex mix of instability accelerated energetic ions, energetic decaying plasma, intense ionization wave and the shock front propagating in the forward direction and (ii) deposition of thin films of metals or alloys (which can be fixed to the anode top) and their nitrides, carbides and oxides using inert gases, hydrogen, nitrogen, methane or oxygen as operating gases.

2.3.1 Processing of Bulk and Thin Films using DPF Device

The instability accelerated energetic ions combined with decaying energetic high energy density plasma and intense shock wave process the bulk or thin film samples that are placed down the

anode stream. The pulse duration of energetic ion beam depends on pinch phase duration of plasma focus device which in turn depends on the characteristic time ($\sim\sqrt{L_0 C_0}$; where L_0 and C_0 are system inductance and capacitance respectively) of the device. In low and mid energy plasma focus the energetic ion beam duration is of the order of several tens to about hundreds of ns while in bigger plasma focus device it might be several hundred ns resulting in transient processing of the exposed/irradiated sample. The ion energy range, however, is not affected, significantly, by the change in stored energy of the device and found to remain in several tens of keV to MeV range.

The ion energy flux, on the sample being exposed, however changes with the storage energy of the DPF device m. The increase/decrease in capacitance (for DPFs of different storage energy) increases/decreases the quarter time period of the discharge current; and then the anode dimension has to be suitably increased/decreased to achieve the maximum compression efficiency in the pinch phase by synchronizing the occurrence of pinch phase (refer figure 2) with current maximum at about the quarter time period of the discharge pulse. The change in anode dimensions changes the size of the pinched plasma column, and hence the number of ions in the pinched plasma column, as x-ray pin hole imaging results have shown that the radius and length of the pinched plasma column are approximately one tenth and equal to radius of the anode, respectively. This basically implies the intensity/degree of processing of the ion irradiated/exposed samples depends on the storage energy of the DPF due to changes in the ion pulse duration and ion energy flux. Sanchez and Feugeas [18], estimated the generation of transient heating slopes and heating speeds as high as ~3600 K μm^{-1} and ~40 K ns^{-1} respectively. They showed that the maximum temperatures reached the material evaporation point at the surface layers and the cooling down process turned out to be fast enough to produce the complete thermal relaxation of the target in only a few microseconds after the end of the ion beam incidence. These intense transient phenomena, with high energy density, can cause extremely high temperature rise rate followed by rapid quenching resulting in changes in several physical properties and compositional characteristics of exposed material surfaces.

A significant amount of work has been done by various research groups across the globe to investigate the effects of the pulsed ion irradiation in DPF device on various bulk and thin film materials. The effects of argon ions irradiation on the amorphous lead zirconate titanate, Sb_2Te_3 and oriented CdI_2 thin films have been reported by Rawat et al. [16, 19, 20]. The amorphization of the crystalline CdS thin film was reported by Sagar and Srivastava [21]. The DPF device has also been used for processing of various bulk and thin films such as: for diode formation on polyanilene thin film [22], to induce phase change from non-magnetic α-Fe_2O_3 to magnetic Fe_3O_4 phase [23], to enhance the T_c of superconducting BPSCCO thick films [24], to irradiate American diamond (high purity zirconia) [25], to implant/irradiate energetic nitrogen ions from DPF device on various materials such as zirconium, aluminum, stainless steel, graphite, ZnO, Ti, nickle ferrite etc [26-28].

2.3.2 Deposition of Thin Films using DPF Device

The DPF device has also been used extensively for the deposition of thin films using the ablation of anode top material (i) by instability accelerated relativistic electrons (which move towards the DPF anode) and (ii) by the high energy density pinch plasma. The ablated anode material plasma moves towards the substrate and is deposited on to it in the form of a thin film. A suitable (inert or reactive) operating gas and anode tip material combination is used for the deposition of various types of thin films. Even though the deposition rate is very high in plasma focus device, we still typically need multiple plasma focus shots for the deposition of thin film of a suitable

thickness. The instability accelerated energetic ions during any given plasma focus shot, transiently process the thin film that has already been deposited before that particular shot resulting in high packing density in the deposited films and simultaneous processing (by transient heating) of thin films during deposition leading to direct synthesis of crystalline thin films without any need for post deposition annealing. Due to these novel features of dense plasma focus device, many groups have used it for synthesis of various thin films. Kant et al. reported the application of it for carbon [17] and fullerene [29] thin film deposition. Rawat et al. have successfully deposited thin films of titanium carbide [30], titanium nitride [31], titanium dioxide [32] and Fe [33] thin films. Many researchers have deposited diamond like carbon thin films using plasma focus device [34-37]. Other thin films that have been successfully deposited using plasma focus device are that of FeCo [38], tungsten nitride [39], aluminium nitride [40], silicon carbide [41], hafnium oxide [42] etc.

3. Hard Coatings Using Plasma Focus

Hard and superhard nanocomposite (nc) coatings with tailored functional properties are suitable for numerous engineering applications ranging from protective coatings for cutting tools and automobile parts to biomedical instrumentation and aircraft engines [43, 44]. The tools are the key of every industrial production. Together with the development of the cutting tool materials, the protective coatings have been developed as well. The common feature of the hard coatings is the protection of the tool they provide by their high hardness and chemical inertness. The combination of bulk material and the suitable hard coating ensures optimal tool properties.

The most common hard coatings are based on transition metal nitrides (TiN, CrN), but in the last decade there has been a vast increase in multicomponent coatings (TiAlN, TiCN), multilayer coatings (TiN/TiAlN) as well as carbon-based coatings (DLC). The newest generation is represented by nanocomposite (TiN+DLC) and lubricating coatings (WC+C).

The most important feature of the hard protective coatings is to reduce wear and in this way to increase the tool lifetime. So it is important to know which mechanism has the highest contribution to the wear (abrasion, adhesion, corrosion, high temperature, material sticking etc.) in order to find the most suitable coating for the desired process. A combination of certain coating properties opens possibilities for new technological procedures, e.g. low coefficient of friction and resistance against high temperatures enables dry machining without use of cooling-lubricating liquids. Aside from the price reduction such a procedure is superior from the ecological standpoint.

3.1 Mechanism of Hard Coating Synthesis using Plasma Focus Device

The research team at Plasma Radiation Source Lab, NIE/NTU has successfully synthesized hard coatings of TiN, TiC, TiCN, AlN, DLC etc using a plasma focus device. These investigations have proved that a plasma focus device can indeed be successfully used for as-deposited crystalline coatings at room temperature substrates with significant hardness. The coatings are dense with nanoparticle surface morphology. The central hollow copper anode was changed to solid titanium or aluminium or graphine for this purpose and suitable background gases were used as the working gas.

The mechanism of synthesis of hard TiN coating is discussed in the paragraph to broadly understand the underlying principle processes that take place in plasma focus device. In a plasma focus device a dense pinched plasma column is formed at the top of the anode during the radial

collapse phase and the plasma temperature is so high that it causes the complete ionization of the filling gas species (nitrogen) resulting formation of nitrogen ions, atoms and molecules. In plasma focus devices, sausage instabilities (m=0) break the focused plasma column by accelerating nitrogen ions, to very high energies, towards the top of the chamber and electrons towards the positively charged anode. The interaction of relativistic electrons and energetic plasma cause the ablation of anode material forming the Ti plasma which reacts with ambient nitrogen plasma resulting in TiN formation on substrate. The energetic nitrogen ions from the next focus shot results in rapid thermal annealing of the deposited TiN layer and also help in increasing packing density. It may be pointed over here that the standard processes for TiN deposition are magnetron sputtering and cathodic arc evaporation, which supply energetic particles for film densification. Using a cathodic arc, with an ionisation rate of nearly 100% and an average charge state of up to 3+, even higher energies per atom are possible. With our high energy density plasma focus system, it is possible to attain much higher ionization states of Ti and N and simultaneous processing of the deposited material by high energy ion can be used to achieve novel tribological properties in TiN coatings.

3.2 Various Hard Coating Synthesis at PRSL using Plasma Focus Device

3.2.1 TiN Thin Films

Successful deposition of as grown polycrystalline TiN thin films onto stainless steel substrates was achieved at different distances from the top of anode and at different angular positions with respect to the anode axis and using different number of focus deposition shots [31]. In addition to TiN and substrate diffraction peaks, the diffraction patterns for films deposited along the anode axis showed the induction of a phase corresponding to Iron Chromium Nickel on the film-substrate interface. SEM pictures confirmed smooth film surface with uniformly distributed TiN grains of nanoscale dimensions. EDX mapping confirmed the uniform distribution of TiN on the film surface. The hardness of TiN film was found to increase from 11 to 14 GPa with the increase in the number of focus deposition shots from 10 to 20 and finally reached the highest value of 24 GPa for film deposited using 30 focus shots. Some of the key features that could be noted in this study were:

1. As-deposited TiN thin films were directly in crystalline phase without any need for post-deposition annealing. This is an advantageous feature as it gives the possibility of depositing hard coating directly in crystalline phase with better tribological properties on soft substrate surfaces such as plastics or polymers.
2. The coatings were essentially nanostructured with nanoparticles and nanoparticle agglomerates with the nanoparticle size depending on the plasma focus deposition shots, angle of deposition and background gas pressure.
3. The films were crack-free and densely packed.
4. The deposition rates were extremely high.

3.2.2 TiC Thin Films

Thin films of titanium carbide (TiC) were deposited on 304-stainless steel substrates, at a distance of 11.5 cm, using different numbers of focus shots, like 10, 20 and 30, at room temperature substrates [30]. The central electrode was composed of high purity solid titanium anode and argon-acetylene mixture was used in 7:3 ratio as background gas. XRD patterns in all three cases were found to have diffraction peaks for (111), (200), (220), and (311) TiC crystalline planes. Surface morphological studies using SEM revealed increasing clustering of

TiC grains with the increase in number of focus deposition shots. EDX spectra confirmed the presence of constituent elements with the gradual increase in TiK_α peak (of the TiC thin film) relative to FeK_α peak (of the substrate) with increasing numbers of focus deposition shots due to increasing film thickness. Growth of TiC layer on Ti substrate by implanting carbon ion from the graphite top fitted anode has also been observed using 100 to 250 focus shots using repetitive NX2 plasma focus device. The key features related to TiC deposition using plasma focus device, mention in section 3.2.1 remain valid.

3.2.3 DLC Thin Films

Successful deposition of DLC (diamond-like carbon) thin films was achieved using the 3.0 kJ mid-energy UNU-ICTP plasma focus device [34]. The device was fitted with high purity graphite on the top of copper anode and neon was used as the operating gas. The DLC thin films were deposited on silicon (100) substrates at 120 mm from the top of anode, at different angular positions with respect to the anode axis and using different numbers of focus deposition shots. The laser shadowgraphic studies were performed to investigate the effect of discontinuity from copper anode to graphite top on the symmetry of the fast moving current sheath in axial and radial collapse phase, and also to outline DLC thin-films deposition process by investigating the ablation of graphite anode top in the post radial collapse phase. The shadowgraphs showed that the symmetry of the current sheath in axial and radial phase was maintained. It was also noticed that the ablation of carbon plasma plume from the graphite anode top last for about 2 μs with angular asymmetry of the ablated ion flux. The observation of Si impurities in the DLC films points to the ablation of silicon substrate by the energetic neon ions that are generated by sausage instabilities during the radial collapse phase. A qualitative understanding of structure, bonding and the chemical compositions of the DLC thin films was presented using Raman and XPS characterization. The observation of D and G peak in Raman spectra confirmed the presence of sp^2 and sp^3 bonded DLC formation in the deposited thin film samples which was also confirmed by XPS results. For the films deposited at the off-center position, the I_D/I_G ratio ranged from 0.27 to 0.58 corresponding to sp^3 content of 77% and 56%, respectively. For the films deposited at the outermost position, the I_D/I_G ratio was found to vary from 0.32 to 0.53 corresponding to sp^3 content of 60%–73%. The observed variation in Raman spectroscopy and XPS results with the variation in the different deposition conditions were explained on the basis of ion emission characteristics of the focus device.

Recently, we have successfully deposited DLC thin films on the silicon substrates using low-energy (220 J) repetitive miniature plasma focus device operated at repetition rate of 1 Hz with 0.25 mbar of hydrogen [37]. XRD patterns exhibited the diffraction peaks related to carbon, silicon carbide and silicon dioxide. The formation of carbide phases of Si, as observed in XRD spectra, was attributed to the chemical reaction of C plasma with the Si ions ablated by energetic ions. The existence of the D and G peaks in Raman spectra obtained from the films deposited with different number of focus deposition shots confirmed the formation of DLC films. The D and G peak positions for 10, 20 and 50 shots move towards lower wave-number and with the further increase in the number of deposition shots to 100 and then 200 the D and G peak positions start to shift towards higher wave-number. This shift in D and G peak positions was attributed to tensile and compressive stress in the samples. Surface morphology showed the samples deposited with 10 and 20 focus shots have relatively smooth film with small and separated nanoparticles and the samples deposited with high number of shots have bigger sized patches or grains which are the agglomerates of smaller sized particles. The observation of Si in XPS scan, which is essentially a surface probe, confirms the observation of Si on substrate

surface and hence verifies the proposed hypothesis of ablation of Si by energetic ions. XPS results also confirm the presence of sp^2 and sp^3 components in the deposited samples. Finally, the average DLC thin film deposition rate of about 250 nm/min makes 220 W miniature plasma focus device a novel high deposition rate facility for DLC.

3.2.4 Ti(C,N) Thin Films

Titanium carbo-nitride shows various kinds of excellent properties, e.g., high melting point, high hardness, erosion resistance, oxidation resistance and high wear resistance, so it is widely used to prepare advanced ceramic-based composites which are applied in metal working, electrical and electronic, automotive and refractory industries. The grain size of Ti(C,N) has important influence on properties of composites, that is, the smaller Ti(C,N) particle are, the better the hardness, wear resistance and toughness. Nanostructured multiphase Ti(C,N)/a-C films were deposited using a 3.3 kJ UNU-ITCP plasma focus device onto silicon (1 0 0) substrates at room temperature [45]. The plasma focus device, fitted with solid titanium anode instead of usual hollow copper anode, was operated with nitrogen and Ar/CH_4 as the filling gas. Films were deposited with different number of shots, at 80 mm from top of the anode and at zero angular position with respect to anode axis. X-ray diffraction results exhibited the diffraction peaks related to different compounds such as TiC_2, TiN, Ti_2CN, Ti and $TiC_{0.62}$ confirming the deposition of multiphase titanium carbo-nitride composite films on silicon. X-ray photoelectron spectroscopy confirmed the formation of Ti–C, C–N, Ti–N, Ti–O and C–C bonds in the films. SEM results revealed that nanostructured grains were not the individual nanoparticles but the agglomerates of smaller sized nanoparticles about 10–20 nm in size. The average size of these agglomerates were estimated to be about 50 ± 9, 95 ± 8 and 120 ± 7 nm for samples deposited using 10, 20 and 30 shots respectively. Raman spectroscopy confirmed different chemical composition onto the surface and also confirmed that amorphous graphite like carbon phase was formed on the samples deposited using 20 or more focus shots. The XPS Ti 2p, C 1s, N1s and O 1s peaks showed that the nitride, carbide, oxide and carbonitride of titanium coatings were formed, respectively. The hardness of Ti(C,N)/a-c, characterized by Vickers microhardness tester, was found to have a maximum value of 14.8 ± 1.3 GPa for 30 shots probably due to increased grain size.

3.2.5 AlN Thin Films

Nanocrystalline AlN films, owing to their wide band gap, low electrical but high thermal conductivity, high optical transmission and high decomposition temperature, are used in microelectronic industry. Due to good piezoelectric properties with high acoustic velocity, they are also used in the fabrication of acoustic devices. We have successfully synthesized the nanocrystalline AlN surface layers by irradiating Al substrates by energetic nitrogen ions in a medium energy plasma focus device [40]. The XRD patterns confirmed the formation of AlN phases. The crystallinity of AlN planes, average crystallite size and stress relaxation were found to increase the increasing number of focus shots which was attributed to the increased repeated rapid thermal of the samples. Improved crystallinity of AlN (111), (200), (220) and (311) planes was observed for low (473 K) annealing temperature while it decreased for high (523 K) annealing temperature except for AlN (220) plane. The AlN (220) plane disappears completely for higher annealing temperature thereby indicating that it was unstable for high annealing temperature. The Raman analysis confirmed the existence of E1 (TO) and A1 (LO) vibrational modes while FTIR study confirmed the presence of E1 (TO) phonon mode (~ 667.8 cm-1) of annealed (473 K) AlN film. Up-shifting in phonon mode indicated the presence of compressive

stresses. SEM microstructures showed rounded grains (~ 20 nm to 70 nm) and few agglomerates (~ 300 nm to ~ 500 nm). A net type microstructure consisting of circular holes of ~ 50 nm diameter were also observed for 25 focus shots.

4. Nanophase Magnetic Materials using Plasma Focus

The nanophase magnetic materials have various promising applications of; ranging from ultra-high density magnetic data storage, biosensors, gas sensor, toner material for high quality colour copier and printer, new generation electric motor and generator, environment friendly refrigerants, biomedicine etc [46]. In addition, due to their comparable size to biological entities (such as 10-100 μm cells and 20-250 nm viruses) nanophase magnetic materials will find applications in bio-medicine and biotechnology [47].

In recent decades, the recording areal density in data storage industry has been increasing at a rate of about a factor of 10 every 10 years. The data areal density limitation on the recording media resulted from super-paramagnetic limit which is well established when the particle size reaches the critical volume. There is a certain amount of energy required to "flip" a magnetic domain on a disk surface from one orientation to the other (representing the flip of data bit from "0" to "1"). When this amount of energy becomes comparable to the thermal energy (= kT; where k is the Boltzmann constant and T the temperature) that a domain has at room temperature, the domains will spontaneously flip orientation at random. This so called "super-paramagnetic limit" puts a ceiling on the areal density that could be achieved. One of the most commonly followed practices, these days, to overcome the super-paramagnetic limit, to increase thermal stability, is to use films of materials, such as CoSm and CoCr, CoPt, FePt and CoCrPtM (M=Ta, Nb, B, C, etc.) alloys, which have higher values of magnetic anisotropy K_u for the magnetic recording media.

The FePt and CoPt binary alloy nanoparticles, containing a near-equal atomic percentage of Fe/Co and Pt, are an important class of magnetic nanomaterials as they are chemical stabile and exhibit the possibility of existing in a phase with high magnetic anisotropy constant K_u. The FePt is known to have two solid phases; CoPt also has exact similar solid structures with Fe simply being replaced by Co. These two phases basically are in two types of crystal structures: (i) chemically disordered face-centered-cubic (*fcc*) structured $A1$ phase and (ii) chemically ordered face-centered-tetragonal (*fct*) structured $L1_0$ phase. The FePt and CoPt exhibit a *fcc* structure with a random distribution of Fe/Co and Pt atoms in corner positions and face centred positions. In this $A1$ phase, FePt and CoPt have lower anisotropy constant K_u with smaller coercivity value and exhibit magnetically soft character. The fully ordered *fct* phase of FePt or CoPt can be viewed as alternating atomic layers of Fe/Co and Pt stacked along the (001) direction (c-axis), which has high anisotropy constant K_u with a high coercivity value and thus exhibits magnetically hard character. The FePt and CoPt in ordered *fct* $L1_0$ phase are found to have high uniaxial magnetocrystalline anisotropy constants of $(6.6\text{-}10)\times10^7$ erg/cm^3 and 4.9×10^7 erg/cm^3, respectively [48]. Due to their exceptionally high K_u value these materials can exhibit ferromagnetic character up to the nanoparticle size of about 3-4 nm.

It may, however, be noted that the as-deposited, when deposited at room temperature, FePt and CoPt show a disordered *fcc* structure which is magnetically soft (low coercivity) and need to undergo a phase transition from the disordered *fcc* structured $A1$ phase to the ordered *fct* structured $L1_0$ phase after post-deposition annealing at an elevated substrate temperature of about 600 to 700 °C to exhibit hard magnetic character required for data storage [49]. However, the high annealing temperature needed for the phase transition, which is reported to be greater than

500 °C, may cause nanoparticle agglomerations or grain growth and hence the particles may no longer stay isolated which lead to the deterioration of magnetic properties and also the increase in particles size is undesirable for ultra-high data storage density. Hence, achieving low temperature phase transition in FePt/CoPt thin films from magnetically soft low K_u *fcc*-structured $A1$ phase to magnetically hard high K_u *fct*-structured $L1_0$ phase is one of the key challenges in ultra-high density magnetic data storage.

4.1 Low Temperature Phase Transition of PLD grown FePt Films using DPF Device

Our group has [50] reported the lowering of the phase transition temperature to 300 °C in FePt:Al_2O_3 nanocomposite thin films synthesized by magnetic trapping assisted pulsed laser deposition. Another approach for lowering down the phase transition temperature is using ion irradiation [51]. However, all of these ion irradiation results are obtained by continuous ion sources with, typically, hours of irradiation duration. The lowering of *fcc* to *fct* phase transition temperature of the PLD grown FePT thin films has also been achieved using the pulsed energetic ion beam from DPF device.

The FePt thin films with two different thicknesses of about 67 and 100 nm were grown on Si (001) substrates at room temperature by pulsed laser deposition (PLD) [52] in vacuum (better than 3×10^{-5} mbar). The Continuum Nd:YAG laser (532 nm, 10 Hz, 10 ns and 80 mJ) was focused on FePt (50:50 at%; Kurt J. Lesker, 99.99%) target disc with energy density of about 1×10^3 J/cm^2, and samples were deposited at the target-substrate separation of 3 cm. The FePt thin films then were irradiated by highly energetic H^+ ions using UNU/ICPT (United Nation University/International Center for Theoretical Physics) DPF device [3]. The samples were placed axially along the anode axis at various distances from the anode top and were also exposed to different numbers of plasma focus irradiation shots. The working gas used is hydrogen, which was kept at a filling gas pressure of 5 mbar. Full details of the experimental setup and irradiation procedures can be found in our papers by Lin et al. [52] and Pan et al. [53, 54]. After exposure, the FePt thin films were heated in vacuum furnace to various temperatures, at the rate of 60 °C/min, and maintained for 1 hour before being cooled down naturally.

4.1.1 H^+ Ion Irradiation on 67 nm FePt Thin Film using DPF Device

The PLD grown FePt samples were irradiated by hydrogen ions from UNU-ICTP DPF device at a distance of the 5 cm from the anode top [52]. The as-deposited FePt thin films were smooth with laser droplets dispersing on the surface. The morphology of FePt thin films changed from that of the smooth uniform film to film with uniform and isolated nanoparticles after a single DPF shot exposure. The average particle size were found to be 9.1±2.3 nm. As the number of ion irradiation DPF shots were increased to two, the morphology of irradiated samples changed to nanoparticle agglomerates of bigger size of about 51.3±7.4 nm. The X-ray diffraction (XRD) spectra of the as-deposited thin films exhibited *fcc* phase with a broad peak of (111) at about 41° which after single shot DPF exposure almost disappeared which might be because of: (i) continuous accumulation of defects which destabilize the crystal structure at some critical levels, and (ii) rapid quenching of irradiation induced liquid thermal spike regions. The XRD spectrum of single shot irradiated sample and later being annealed at 300 °C showed (111) and (002) diffraction peaks of *fcc* phase with slight splitting indicating that some of the FePt nanoparticles might have been converted to ordered *fct* phase. By increasing the annealing temperature to 400 °C, more peaks appeared on the XRD pattern. The appearance of (001) peak at around 24° and the splitting of the fundamental (111) and (002) peaks indicated the phase transition to the long-

range $L1_0$ ordered *fct* phase. The enhancement in (001) and (002) peaks indicates that most of the FePt nanoparticles have their (001) planes parallel to substrate surface, which would give rise to high magnetocrystalline anisotropy and high coercivity in in-plane hysteresis behavior. However, for the samples without ion irradiation, they remained in *fcc* phase after annealing at 400 °C, which would not convert to *fct* phase unless the annealing temperature was raised up to 600 °C. The low phase transition temperature of ion irradiated samples can be explained by the impact of energetic ions and neutral species which provoke significant adatom mobility and a decrease of the activation energy for atomic ordering by increasing point defects such as vacancies and interstitials.

The in-plane hysteresis loops show that (i) as-deposited FePt thin film were weakly ferromagnetic with coercivity of about 75 Oe, (ii) sample irradiated with one shot ion irradiation was almost similar with marginal increase in coercivity to about 96 Oe, (iii) by annealing the ion irradiated sample at 300 °C, the coercivity increased to about 447 Oe which may be due to the partial transition of FePt nanoparticles to $L1_0$-ordered *fct* phase as indicated by the slight splitting of (111) and (002) fundamental peaks, and (iv) a drastic increase in coercivity to about 1563 Oe (with a 16 fold increase) was observed for the sample irradiated by one DPF shot and then annealed at 400 °C. The many fold increase in the coercivity of the last sample was explained by the phase transition from low K_u *fcc*-FePt to high K_u *fct*-FePt nanoparticles.

4.1.2 H^+ Ion Irradiation on 100 nm FePt Thin Film using DPF Device

The changes in surface morphology of ~100 nm FePt thin film samples after exposure to different number of focus shots was similar the one reported for ~67 nm FePt thin film samples as they all changed from smooth thin films to nanoparticles. Single shot ion-irradiation led to the formation of very small and uniform nanoparticles with average particle size of about 8±2.5 nm, along with some bigger sized (~30-40 nm) nanoparticles agglomerates. The two shot irradiation lead to slight increase in the size of particle agglomerates but most of the particles forming the background were still very uniform and small; however with the three shot irradiation uniformity in the particle size distribution was destroyed as the particles with the sizes ranging from about 20 to 100 nm were observed [53].

The XRD results showed that the intensity of diffraction peaks for sample exposed to single DPF irradiation shot, without annealing, (i) increased as compared to that of as-deposited sample and (ii) is almost similar to that of un-irradiated sample annealed at 400 °C implying thereby that single shot of pulsed plasma focus ion irradiation provides almost equal amount of energy that is offered by conventional thermal annealing for 1 hour at 400 °C [53]. Similarly, the samples exposed at the distances of 5, 6 and 7 cm showed enhanced crystallinity after single DPF shot exposure [54]. This was in contrast to results obtained for ~67 nm film exposed to one DPF shot at 5 cm where the irradiated sample became almost amorphous indicating thereby the change in the thickness of the film can significantly affect the degree of transient thermal processing caused by the energetic ions [52]. The annealing of all ion irradiated sample, whether irradiated by different number of DPF shots at 4 cm or irradiated at different distances, at 400 °C lead to the phase transition from disordered *fcc* structured *A*1 phase to chemically ordered *fct* structured $L1_0$ phase indicated by the appearance of the superlattice tetragonal (001), (110) and (002) peaks. The TEM bright-field images confirmed the formation of well separated narrow size distributed FePt nanoparticles with the average particle size of 11.6±3.4 nm and selected area diffraction (SAD) confirmed that they were in polycrystalline *fct* phase. The phase transition at lower temperature, for single focus shot irradiation, had restricted nanoparticles grain size growth and

agglomeration resulting in relatively small (about 11.6±3.4 nm) and well separated magnetically hard *fct* phase FePt nanoparticles which is important for higher magnetic data storage density.
The as-deposited FePt thin film showed weak ferromagnetism, with coercivity of about 78 Oe, which after annealing at 400 °C increases slightly as the coercivity increased to 177 Oe. The samples irradiated by different numbers of focus shots before annealing exhibited soft magnetic property with coercivity similar to that of the as-deposited sample. After annealing at 400 °C the samples irradiated to single DPF shot at different distances from anode top showed an neormous increase in coercivity to values >5000 Oe. The sharp increase in coercivity was due to the transformation from magnetically soft disordered *fcc* to magnetically hard ordered $L1_0$ *fct* phase, and also due to the formation of separated nanoparticles on irradiated sample surface resulting in lower inter-particle exchange coupling.

4.2 Nanophase Magnetic CoPt Thins Film Synthesis using DPF Device

The conventional central hollow copper anode of NX2 plasma focus device was replaced by a high purity (50:50 at%; Kurt J. Lesker, 99.99%) solid CoPt tip fitted copper anode. Two sets of experiments were done [55]: (i) the hydrogen gas pressure was changed from 2 to 8 mbar keeping the other parameters fixed, and (ii) the number of plasma focus deposition shots was changed from 25 to 200 shots for fixed filling gas pressure of 6 mbar hydrogen. The anode-substrate distance was set to 25 cm and the NX2 DPF was operated in sub-kJ energy range with the lower charging voltage of 8 kV.
The morphological features of the nanostructured CoPt thin films were found to depend strongly on the filling gas pressure and the number of DPF deposition shots used. The SEM image of 2 mbar deposition showed a two layered structure with the top layer sintering together to form big island-like structures and a sub layer of some agglomerates between the nanoislands. For 4 mbar deposition only the particle agglomerates with the average agglomeration size of 35±6.0 nm were observed and the island like structures disappeared. With the increase in filling gas pressure to 6 and 8 mbar average size of these nanoparticles/ particle agglomerate was found to decrease to 15±3.0 and 10±2.0 nm respectively. The cross-sectional SEM images that thicknesses of the samples deposited at 2, 4, 6, and 8 mbar are estimated to be about 94.0±4.0, 58.0±3.0, 44.0±2.0 and 22.0±1.0 nm, respectively.
The SEM images of CoPt thin films samples deposited at 6 mbar using different numbers of DPF deposition shots (25, 50, 100, 150 and 200 shots respectively) showed that with the increase in the number of deposition shots, the morphology changes from well separated small sized nanoparticles (for 25 shot deposition with particle size of about 15 nm) to nanoparticle agglomerates of increasing size e.g. the average size of agglomerate is estimated to be 32.8±7.0 nm for the sample deposited with 50 shots. The thicknesses of as-deposited samples, estimated from cross-sectional SEM images, are found to be about 44.0 ±2.0, 72.5±4.0, 208.1±8.0, 294.5±14.0 and 331.7 ±12.0 nm for 25, 50, 100, 150 and 200 shots deposition samples respectively. The average deposition rate of CoPt nanoparticle thin film was about 1.78 nm/shot for NX2 plasma focus device operating at 880 J at 6 mbar hydrogen ambience at the substrate distance of 25 cm from the anode top. This deposition rate is more than 30 times higher as compared to that of conventional PLD which is found to be about 0.50 Å/shot [56].
The structural analysis showed that all of as deposited samples were in *fcc* phase with a broad and weak peak of (111) plane at about 41°. The crystallinity in general improved with one hour annealing at 500 °C, but the sample remained in *fcc* phase. The transition to desirable $L1_0$ *fct* phase was seen to occur only after the annealing temperature was raised to 650 °C. The investigation of magnetic properties of as-deposited samples without annealing showed very weak

coercivity which were in confirmation with the *fcc* phase observed for these samples in structural analysis. The coercivity of the samples after annealing at 650 °C were significantly enhanced to about 1700, 3014, 618 and 696 Oe for samples deposited at 2, 4, 6 and 8 mbar respectively which confirmed the phase transition from disordered *fcc* phase to ordered *fct* phase which exhibits a high magnetic anisotropy.

The XRD analysis of CoPt thin films deposited at 6 mbar of hydrogen as ambient gas using different number of focus shots (25, 50, 100, 150 and 200 focus deposition shots) showed that all of as deposited samples were in *fcc* phase with a broad peak of (111) plane at about 41°. After being annealed at 600 °C, weak *fct* superlattice peaks of (001), (110), and (201) appeared as a result of the phase transition to *fct* phase. The intensity of superlattice peaks increased significantly when the annealing temperature is increased to 700 °C as the samples were converted into a highly ordered $L1_0$ phase. The average crystallite sizes, estimated from diffraction results, for all as-deposited samples were found to be in a very narrow range of 6.1±0.5 nm and did not increase with the increase in number of shots. This was because all these depositions were done at a much bigger distance of 25 cm and simple estimates predict that the temperature rise at this distance will be insignificant to increase the crystallite size.

The hysteresis loops of as-deposited nanostructured CoPt thin film samples synthesized using 25, 50, 100, 150 and 200 shots showed weak ferromagnetic signal as they were in low K_u soft magnetic *fcc* phase. The coercivity of the samples annealed at 500 °C annealed samples though remained low but it increased with the increase in number of DPF shots because the crystallinity of *fcc* phase was enhanced due to annealing even though it was not transformed to *fct* phase. After being annealed at 600 °C, a very significant increase in the coercivity was observed for the most of the samples, except for sample deposited with 25 shots, which can be attributed to the start of phase transition from magnetically soft *fcc* phase to magnetically hard *fct* phase at this temperature. A further increase in annealing temperature to 700 °C resulted in extremely high coercivity, in excess of 6800 Oe for samples deposited using 100 and 150 shots and reaching to about 9000 Oe for 200 shot deposition sample, due to achievement of highly ordered *fct* structure $L1_0$ phase in these samples.

5. Conclusions

The paper reviewed the successful application of dense plasma focus device, a novel pulsed high energy density plasma source, in plasma nanoscience and nanotechnology (i) for synthesis of crack free, nanostructured, ultra dense hard tribological coatings such as TiN, TiC, Ti(C,N), DLC and AlN and also for CoPt magnetic nanoparticle based thin films and (ii) as an energetic ion irradiation facility for processing of magnetic thin films grown by PLD. The DPF device offers a complex mixture of high energy ions of the filling gas species, immensely hot and dense decaying plasma, fast moving ionization wavefront and a strong shockwave that provides a unique plasma and physical/chemical environment that is completely unheard of in any other conventional plasma based deposition or processing facility.

Some of the key features of thin film deposition using plasma focus or processing of thin films deposited by other methods by energetic ions in plasma focus device include:

1. The as-deposited thin films, if deposited at closer distances of 4 to 12 cm, were directly in crystalline phase. This means that post-deposition annealing is not required to achieve the crystalline phase in the deposited films. This is an advantageous feature as it gives the

possibility of depositing hard coatings directly in crystalline phase with better tribological properties on soft substrate surfaces such as plastics or polymers.

2. Though the depositions at high anode-substrate distances were either weakly crystalline or amorphous but these coating become crystalline at much lower post deposition annealing temperatures pointing to the strong role played by high density high temperature plasma and accompanying energetic ion beam irradiation available in plasma focus device.
3. The coatings were essentially nanostructured with nanoparticles and nanoparticle agglomerates. The nanoparticle size can be tailored by changing the number of focus deposition shots, angle of deposition, distance of deposition and background gas type and gas pressure.
4. The films were densely packed probably due to energetic ion assisted deposition and mostly posses novel physical properties as high energy density plasma focus system is able to provide the ablated anode material ions and filling gas species ions in much higher ionization states.
5. The deposition rates are extremely high in plasma focus device compared to most of the other plasma based depositions due intense ablation of anode material by energetic electron beam and high energy density plasma. Though to fully utilize its potential as high deposition rate facility, high repetition rate plasma focus device capable of operating at 10s of Hz will be required.

To conclude, the dense plasma focus is indeed a novel high energy density pulsed plasma device with immense potential for synthesis of nanophase hard coating and hard magnetic materials.

Acknowledgement

Author wish to acknowledge collaborations and scientific discussions with all collaborators and financial support from NIE and NTU for various research projects.

References

[1] J. W. Mather, Physics of Fluids **8,** 366 (1965).
[2] N. V Filippov, T. I. Filippova and V. P. Vinogradov, Nuclear Fusion **2,** 577 (1962).
[3.] S. Lee, T. Y. Tou, S. P. Moo, M. A. Eissa, A. V. Gholap, K. H. Kwek, S. Mulyodrono, A. J. Smith, Suryadi, W. Usada, and M. Zakaullah, American Journal of Physics **56**(1), 62-68 (1988).
[4] L. Soto, Plasma Physics and Controlled Fusion **47**, A361-A381 (2005).
[5] S. Lee, Applied Physics Letters **95**(15), 151503 (2009).
[6] J. H. Lee, L. P. Shomo, M. D. Williams, and H Hermansdorfer, Physics of Fluids **14**(10), 2210 (1971).
[7] L. Rapezzi, M. Angelone, M. Pillon, M. Rapisarda, E. Rossi, M. Samuelli, and F. Mezzetti, Plasma Sources Science & Technology **13** (2), 272-277 (2004).
[8] Rishi Verma, R. S. Rawat, P. Lee, M. Krishnan, S.V. Springham, and T.L. Tan, IEEE Transactions on Plasma Science **38**(4), 652-657 (2010).
[9] P. Lee, X. Feng, G.X. Zhang, M.H. Liu, S. Lee, Plasma Sources Science and Technology **6**(3), 343 (1997).
[10] M. V. Roshan, S. V. Springham, R. S. Rawat, and P. Lee, IEEE Transactions on Plasma Science **38**(12), 3393-3397 (2010).
[11] V. A. Gribkov, et al., Journal of Physics D-Applied Physics **40**(12), 3592-3607 (2007).
[12] A. Bernard, A. Coudeville, A. Jolas, J. Launspach and J. de Mascureau, Physics of Fluids **18,** 180 (1975).
[13] H. Bhuyan, S.R. Mohanty, T.K. Borathakur, R.S. Rawat, Indian Journal of Pure and Applied Physics **39**, 698 (2001).
[14] K. Ostrikov, U. Cvelbar, and A. B. Murphy, Journal of Physics D: Applied Physics **44**, 174001 (2011).
[15] J. Feugeas, E. Llonch, C. O. de Gonz´alez, and G. Galambos, Journal of Applied Physics **64**, 2648 (1988).
[16] R.S. Rawat, M.P. Srivastava, S. Tandon, A. Mansingh, Physical Review B **47**(9), 4858 (1993).
[17] C. R. Kant, M.P. Srivastava, and R.S. Rawat, Physics letters A **226**(3-4), 212 (1997).
[18] G. Sanchez and J. Feugeas, Journal of Physics D: Applied Physics **30,** 927 (1997).

[19] R.S. Rawat, P. Arun, A.G. Vedeshwar, Y.L. Lam, M.H. Liu, P. Lee, S. Lee, A.C.H. Huan, Materials Research Bulletin **35**(3), 477 (2000).
[20] R.S. Rawat, P. Arun, A.G. Videshwar, P. Lee, S. Lee, Journal of Applied Physics **95**(12), 7725 (2004).
[21] R. Sagar and M.P. Srivastava, Physics Letters A **183**(2-3), 209 (1993).
[22] M.P. Srivastava, S.R. Mohanty, S. Annapoorni, and R.S. Rawat Physics letters A **215**(1-2), 63-67 (1996).
[23] P. Aggarwal, S. Annapoorni, M.P. Srivastava, R.S. Rawat, P. Chauhan, Physics Letters A **231**, 434 (1997).
[24] Priti Agarwala, M. P. Srivastava, P. N. Dheer, V. P. N. Padmanaban, A. K. Gupta, Physica C: Superconductivity **313**(1-2), 87-92 (1999).
[25] S.R. Mohanty, N.K. Neog, B.B. Nayak, B.S. Acharya, P. Lee, T.L. Tan, R.S. Rawat, Nuclear Instruments & Methods in Physics Research Section B-Beam Interactions with Materials and Atoms **243**(1), 113 (2006).
[26] I. A. Khan, M. Hassan, R. Ahmad, A. Qayyum, G. Murtaza, M. Zakaullah and R.S. Rawat, Thin Solid Films **516**(23), 8255-8263 (2008).
[27] S. Karamat, R. S. Rawat, T. L. Tan, P. Lee, S. V. Springham, E. Ghareshabani, R. Chen, and H. D. Sun, Applied Surface Science **257**(6), 1979-1985 (2011).
[28] Rakesh Malik, S Annapoorni, S Lamba, S Mahmood, and R S Rawat, Applied Physics A: Materials Science and Processing **105**(1), 233-238 (2011).
[29] C.R. Kant, M.P. Srivastava, R.S. Rawat, Physics Letters A **239**(1-2), 109 (1998).
[30] R.S. Rawat, P. Lee, T. White, L. Ying, S. Lee, Surface and Coatings Technology **138**(2-3), 159 (2001).
[31] R.S. Rawat, W.M. Chew, P. Lee, T. White, S. Lee, Surface and Coatings Technology **173**, 276 (2003).
[32] R.S Rawat, V. Aggarwal, M. Hassan, P. Lee, S.V. Springham, T.L. Tan and S. Lee, Applied Surface Science **255** (5), 2932-2942 (2008).
[33] R.S. Rawat, T. Zhang, K.S.T. Gan, P. Lee, R.V. Ramanujan, Applied Surface Science **253**, 1611 (2006).
[34] L.Y. Soh, P. Lee, X. Shuyan, S. Lee, and R.S. Rawat, IEEE Transactions on Plasma Science **32**(2), 448-455 (2004).
[35] Shaista Zeb, Ghulam Murtaza, and M. Zakaullah, Journal of Applied Physics **101**, 063307 (2007).
[36] Z.P.Wang, H. R. Yousefi, Y. Nishino, H. Ito and K. Masugata, Physics Letters A **373**, 4169–4173 (2009).
[37] E. Gharshebani, R. S. Rawat, R. Verma, S. Karamat, and S. Sobhanian, Applied Surface Science **256**(16), 4977-83 (2010).
[38] T Zhang, K S Thomas Gan, P Lee, R V Ramanujan, and R S Rawat, Journal of Physics D: Applied Physics **39**(10), 2212–2219 (2006).
[39] M.T. Hosseinnejad, M. Ghoranneviss, G.R. Etaati, M. Shirazi and Z. Ghorannevis, Applied Surface Science **257**(17), 7653-7658 (2011).
[40] I.A. Khan, R.S. Rawat, R. Verma, G. Macharaga, and R. Ahmad, Journal of Crystal Growth **317**(1), 98-103 (2011).
[41] Z. P. Wang, H. R. Yousefi, Y. Nishino, H. Ito. and K. Masugata, Physics Letters A **372**, 7179–7182 (2008).
[42] A. Srivastava, R.K. Nahar, C.K. Sarkar, W.P. Singh and Y. Malhotra, Microelectronics Reliability **51**(4), 751-755 (2011).
[43] R.F. Bunshah (ed.), Handbook of Hard Coatings; Deposition technologies, properties and applications, Noyes publications, Park ridge, New Jersey, USA, 2001.
[44] K. Holmberg, A. Matthews, Coatings Tribology: Properties, Techniques and Applications in Surface Engineering, Elsevier, New York, 1994.
[45] E. Ghareshabani, R.S. Rawat, S. Sobhanian, R. Verma, S. Karamat, and Z.Y. Pan, Nuclear Instruments and Methods in Physics Research B **268**, 2777–2784 (2010)
[46] H.S. Nalwa (Ed.), Hand book of Nanostructured Materials and Nanotechnology, Academia Press, San Diago, 1999.
[47] S. Mornet, S. Vasseur, F. Grasset and E. Duguet, Journal of Materials Chemistry **14**(14), 2161-2175 (2004).
[48] D. Weller, A. Moser, L. Folks, M.E. Best, W. Lee, M.F. Toney, M. Schwickert, J.U. Thiele, M.F. Doerner, IEEE Transactions on Magnetics **36**(1), 10 (2000).
[49] C.P. Luo, S.H. Liou, L. Gao, Y. Liu, D.J. Sellmyer, Applied Physics Letters **77**(14), 2225 (2000).
[50] J.J. Lin, T. Zhang, P. Lee, S.V. Springham, T.L. Tan, R.S. Rawat, T. White, R. Ramanujan, J. Guo, Applied Physics Letters **91**(6), 063120 (2007).
[51] T. Devolder, C. Chappert, Y. Chen, E. Cambril, H. Launois, H. Bernas, J. Ferre, J.P. Jamet, Journal of Vacuum Science & Technology, B: Microelectronics and Nanometer Structures--Processing, Measurement, and Phenomena **17**(6), 3177 (1999).
[52] J.J. Lin, M.V. Roshan, Z.Y. Pan, R.Verma, P. Lee, S.V. Springham, T.L. Tan, R.S. Rawat, Journal of Physics D: Applied Physics **41**, 135213 (2008).

[53] Z. Y. Pan, R. S. Rawat, J. J. Lin, T. Zhang, T. L. Tan, P. Lee and S. V. Springham, Applied Physics A **96**(4), 1027 (2009).
[54] Z.Y. Pan, J.J. Lin, T. Zhang, S. Karamat, R.Verma, M.V. Roshan, S. Mahmood, P.Lee, S.V.Springham, T.L.Tan and R.S. Rawat, Thin Solid Films **517**, 2753-2757 (2009).
[55] Z. Y. Pan, R. S. Rawat, M.V. Roshan, J. J. Lin, R. Verma, P. Lee, S. V. Springham and T. L. Tan, Journal of Physics D: Applied Physics **42**(17), 175001 (2009).
[56] J.J. Lin, S. Mahmood, T.L. Tan, S.V. Springham, P. Lee, R.S. Rawat, Nanotechnology **18**(11), 115617 (2007).

Invited Review Paper

Collaborative Research Work-Experiments Using the AECS Plasma Focus Devices (AECS PF-1 and AECS PF-2)

M AKEL[1], Sh AL-HAWAT[1], S H SAW[2, 3] and S LEE[2, 3]

[1]Department of Physics, Atomic Energy Commission, Damascus, P. O. Box 6091, Syria.
[2]Institute for Plasma Focus Studies, 32 Oakpark Drive, Chadstone, VIC 3148, Australia.
[3]INTI International University College, 71800 Nilai, Malaysia.

Abstract

In collaboration with IPFS and INTI International University we adapted the Lee Model code as a branch version RADPF5.15K to gases of special interest to us namely nitrogen and oxygen and applied numerical experiments specifically to our AECS PF-1 and AECS PF-2. We also generalised the numerical experiments to other machines and other gases in order to look at scaling laws and to explore recently uncovered insights and concepts. The required thermodynamic data of nitrogen, oxygen, neon and argon gases (ion fraction, the effective ionic charge number, the effective specific heat ratio) at different temperatures were calculated, the x-ray emission properties of plasmas were studied, and suitable temperature range (window) for generating H-like and He-like ions (therefore soft x-ray emissions) of different species of plasmas were found as follows: nitrogen: 74 - 173 eV; oxygen: 119 - 260 eV; neon: 200 – 500 eV and argon: 1.4 - 5 keV. The code is applied to characterize the AECS-PF-1 and AECS-PF-2, and for optimizing the nitrogen, oxygen, neon and argon SXR yields. We carried out numerical experiments to optimize each device keeping the bank parameters, operational voltage and $c = b/a$ ratio unchanged but systematically changing other parameters to find the combination of p_0, z_0 and 'a' for the maximum SXR yield. Practically it is difficult to change outer radius 'b'. Keeping 'b' constant we carried out practical optimization for neon and argon plasma. We are running experiments to compare our measurements using different anode radii and lengths with those predicted by the numerical experiments on practial optimization. In numerical experiments we also reduced static inductance L_0 showing that it is useful to reduce L_0 to a range of 10–25 nH; but not any smaller since further reduction produces no yield benefit and would be a futile expensive exercise. These yields at diverse wavelength ranges are large enough to be of interest for applications ranging from microelectronics lithography to micro-machining and microscopy of biological specimens. Scaling laws for SXR of argon and nitrogen plasma focus, in terms of energy, peak discharge current and focus pinch current were found. In a collaborative project with INTI IU model parameters are being measured combining the results of INTI PF and AECS PF-2. Radiative cooling effects are studied indicating that radiative collapse may be observed for heavy noble gases (Ar, Kr, Xe) for pinch currents even below 100 kA. The results show that the line radiation emission and tube voltages have huge values near the radiative collapse regime. The creation of the consequential extreme conditions of density and pulsed power is of interest for research and applications.

1. Introduction

Soft x-ray sources of high intensity are required in diverse areas like x-ray spectroscopy [1], lithography for the manufacture of integrated circuits [2], x-ray microscopy [3], x-ray laser pumping [4] and x-ray crystallography [5]. Work is underway to develop such sources by employing geometries like Z-pinch [6], X-pinch [7], vacuum spark [8] and plasma focus (PF) [9–11]. The latter is the simplest in construction and yet provides the highest x-ray emission compared to other devices of equivalent energy [12, 13]. In the last few years various efforts have been made for enhancing the x-ray yield by changing various experimental parameters such as bank energy [14], discharge current, electrode configuration (shape and material) [15, 16], insulator material and dimensions [15], gas composition and filling gas pressure [17]. Thus, soft x-ray yield optimization studies on the plasma focus devices operating over the wide range of bank energies have been one of the actively pursued fields of plasma focus research owing to possible applications in microlithography, micromachining, x-ray microscopy and material science applications [18-31].

Moreover, numerical experiments are gaining much interest. For example, the Institute of Plasma Focus Studies (IPFS) [32] conducted an International Internet Workshop on Plasma Focus Numerical Experiments [33], at which it was demonstrated that the Lee model code [34] not only computes realistic focus pinch parameters, but also absolute values of SXR yield Y_{sxr} consistent with experimental measurements. A comparison was made for the NX2 machine [13], showing good agreement between computed and measured Y_{sxr} as a function of pressure p_0 [33 - 35]. This gives confidence that the code produces realistic results in the computation of Y_{sxr}.

Numerical experiments are also carried out systematically by S Lee et al [14, 36] to determine the neon Y_{sxr} for optimized conditions with storage energy E_0 from 1 kJ to 1 MJ. At low energies $Y_{sxr} \sim E_0^{1.6}$ whilst towards 1 MJ $Y_{sxr} \sim E_0^{0.8}$. Also $Y_{sxr} \sim I_{peak}^{3.2}$ (0.2 – 2.4 MA) and $Y_{sxr} \sim I_{pinch}^{3.6}$ (0.1-1.3 MA). It is pointed out that the distinction of I_{pinch} from I_{peak} is of basic importance [37 – 39]. The scaling with I_{pinch} is the more fundamental consistent and robust one.

The Pease-Braginskii (P-B) current [40] is that current flowing in a hydrogen pinch which is just large enough for Bremsstrahlung to balance Joule heating. It is known that in gases emitting strongly in line radiation, the radiation-cooled threshold current is considerably lowered. S Lee et. al., showed that Lee model code [34] may be used to compute this lowering [41]. Enhanced compression results from such radiation cooling [42]. Z. Ali et. al. [43], reported that self absorption becomes significant when plasma is dense enough to be optically thick.

In this review paper, we discuss the different states of x-ray radiative nitrogen, oxygen, neon and argon plasmas and their corresponding working conditions in plasma focus. We discuss the laboratory measurements to determine model parameters integrated with the comprehensive range of numerical experiments conducted to derive scaling laws on nitrogen and argon soft x-ray yield leading up the study of radiative collapse effect in the plasma focus.

2. Calculations of Plasma Parameters Using Corona Model

The x-ray radiation properties of plasma are dependent on the plasma temperature, ionization states and density. Plasma equilibrium model can be used to calculate the ion fraction α, the effective ionic charge number Z_{eff}, the effective specific heat ratio γ and x-ray emission of the plasma at different temperatures. The ion fraction is defined as the fraction of the plasma which is ionized to the z^{th} ionized state and it can be written as: $\alpha_z = N_z/N_i$ where: N_z is the z^{th} ionized ion number, N_i is the total ion number densities. The effective ionic charge number Z_{eff} is the average charge of one ion [34, 44 - 47]. Based on corona model, we obtained in

nitrogen, suitable temperature range for generating H-like 1s-2p, N2: 24.784 A^o (500 eV), 1s-3p, N2: 21 A^o (592.92 eV) and He-like 1s^2-1s2p, N2: 29 A^o (426 eV), 1s^2-1s3p, N2: 24.96 A^o (496 eV) ions and He-like ions in nitrogen plasma (therefore x-ray emissions) is 74–173 eV (0.86×10^6–2×10^6 K) [46, 48]. It is also noticed that the nitrogen atoms become fully ionized around 800– 1000 eV.

The suitable temperature range for generating H-like 1s-2p, O_2: 18.97 A^o (653.68 eV), 1s-3p, O_2: 16 A^o (774.634 eV) and He-like 1s^2-1s2p, O_2: 21.6 A^o (573.947 eV), 1s^2-1s3p, O_2: 18.62 A^o (665.615) ions in oxygen plasma (therefore soft x-ray emissions) has been calculated to be between 119–260 eV (1.38×10^6-3×10^6 K) with full ionization at around 2000–3000 eV [47].

For neon, temperature of 200 to 500 eV (2.3×10^6 - 5×10^6 K) is suitable for generating H-like 1s-2p, Ne: 12.132 A^o (1022 eV), 1s-3p, Ne: 10.240 A^o (1211 eV) and He-like 1s^2-1s2p, Ne: 13.447 A^o (922 eV), 1s^2-1s3p, Ne: 11.544 A^o (1074 eV) ions in neon plasma (therefore neon soft x-ray emissions) [45, 49–51].

From the reported experimental results [44, 52, 53], the x-ray emissions from argon plasma are mainly He-like alpha line (He_α (1s^2-1s2p, Ar: 3.9488 A^o (3140 eV)) , 1s^2-1s3p, Ar: 3.365 A^o (3684 eV)) and H-like alpha line (Ly_α (1s-2p, Ar: 3.731 A^o (3323 eV)), (1s-3p, Ar: 3.150 A^o (3936 eV)) lines. So the most intense characteristic emissions of argon plasma are Ly_α and He_α lines. The corresponding x-ray emitters in the argon plasmas are mainly H-like and He-like ions. For argon, a focus pinch compression temperature of 1.4 to 5 keV (16.3×10^6–58.14×10^6 K) is suitable for generating H-like and He-like ions. As example of these calculations is shown in Fig 1 and Fig 2.

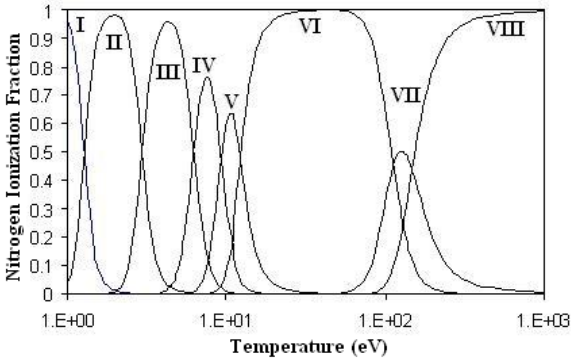

Fig. 1 Nitrogen ion fractions at different temperature, where VIII indicates the ion N^{+7} [46]

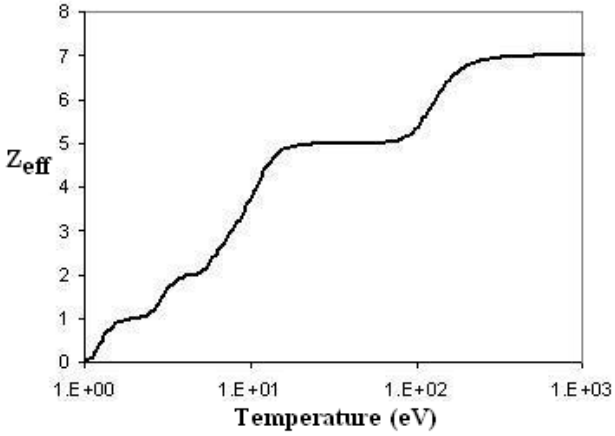

Fig. 2 Effective ionization number Z_{eff} of nitrogen (calculated by corona model) [46]

Based on the above work we take the soft x-ray yield (H-like and He-like ions) from nitrogen, oxygen, neon and argon to be equivalent to line radiation yield i.e. $Y_{sxr} = Q_L$ at a suitable different temperature ranges (T windows) for each gas as follows: 74–173 eV for nitrogen [46], 119–260 eV for oxygen [47], 200–500 eV for neon [49, 51], and for argon is 1.4 to 5 keV [44, 52, 53]. Table 1 presents optimized conditions.

Table 1 Optimization conditions for x-ray radiative plasma of Nitrogen, Oxygen, Neon, Argon

Gas	**Temperature**	**Z_{eff}**	**$E_{ion}=E_i+(3/2)(1+Z_{eff})kT$**
Nitrogen	~ 160 eV	6.48	1.16+1.79 keV [46]
Oxygen	~ 225	7.38	1.59 + 2.82 keV [47]
Neon	~ 420 eV	9.38	2.69+4.36 keV [49]
Argon	~ 3 keV	17.00	11.03+54 keV [52]

3. Numerical experiments using Lee Model

3.1 Soft x-ray yield vs pressure

Numerical experiments have been investigated systematically using Lee model to characterize various low energy plasma focus devices operated with different gases (nitrogen, oxygen, neon, argon) and plasma focus parameters (see Table 2).

Table 2 Tube and electrical parameters for various plasma focus devices

Device (ref.) location	**E (kJ)**	**a (cm)**	**b (cm)**	**Z_0 (cm)**	**L_0 (nH)**	**C_0 (μF)**	**I_{peak} (kA)**	**V_0 (kV)**
UNU/ICTP [51]- INTI	2.7	0.95	3.2	16	110	30	173	13.5
AECS PF-2 [45, 55]-Syria	2.8	0.95	3.2	16	270	35	115	15
AECS PF-1 [46,56-57]- Syria	2.8	0.95	3.2	16	1432	35	50	15
PF-1kJ [30-31,48] Argentina	0.43	1.75	4.9	6.75	65	3.9	90	14.9
UNU/ICTP [26]- Egypt	2.9	0.95	3.2	16	110	30	180	14
APF [58]- Iran	2.6	1.39	2.24	14.8	115	36	220	12
PF [59] -Iran	1.9	1	3	15	126	10	160	19
QAU PF [60]- Pakistan	2.3	0.9	3.5	15.2	80	32	190	12
NX2 [14]- Singapore	1.7	1.9	4.1	4-8	15	28	370	11
SBUPF1 [61, 62]- Iran	2.1	1.1	3.6	12	271	8.6	115	22

For each studied plasma focus device, fitted values of the model parameters were found using the following procedures: The computed total discharge current waveform is fitted to the measured by varying model parameters f_m, f_c, f_{mr} and f_{cr} one by one until the computed waveform agrees with the measured waveform. First, the axial model factors f_m, f_c are fitted until the computed rising slope of the total current trace and the rounding off of the peak current as well as the peak current itself are in reasonable (typically good) fit with the measured total current trace. Then we proceed to adjust (fit) the radial phase model factors f_{mr} and f_{cr} until the computed slope and depth of the dip agree with the measured. These fitted values of the model parameters are used for characterization and soft x-ray optimization of plasma focus at various pressures [55].

For example, experiments have been investigated on the AECS PF-2 with neon at wide range of pressures to get experimental current traces with good focus effect [63] from 0.25 Torr to 1.25 Torr. No focus effect occurs experimentally at higher pressure. To start the numerical experiments we select a discharge current trace of the AECS PF-2 taken with a Rogowski coil at 0.57 Torr (Fig. 3) (time scale 1 μs per large division).

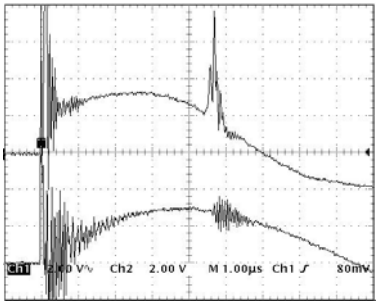

Fig. 3 Voltage (up) and current (down) traces of neon discharge in AECS PF-2, (1vert. div=2 kV for voltage; and 76.8 kA for current); p_0=0.57 Torr, C_0=25 μF, L_0=200 nH, r_0= 14 mΩ, V_0 = 15 kV [63]

We configure the Lee model code (version RADPF5.15K) to operate as the AECS PF-2 plasma focus starting with the above bank and tube parameters.

To obtain a reasonably good fit the following parameters are used:

Bank parameters: L_0 = 280 nH, C_0 = 25 μF, r_0 = 25 mΩ,

Tube parameters: b = 3.2 cm, a = 0.95 cm, z_0 = 16 cm,

Operating parameters: V_0 = 15 kV, p_0 = 0.57 Torr, neon gas,

together with the following fitted model parameters:

$$f_m = 0.1, f_c = 0.7, f_{mr} = 0.2 \text{ and } f_{cr} = 0.7.$$

With these parameters, the computed total current trace agrees reasonably well with the experimental trace (Fig. 4).

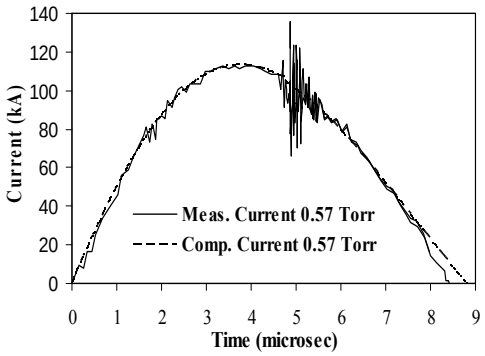

Fig. 4 Comparison of the computed current trace (dotted line) with the experimental one (solid smooth line) of the AECS PF-2 at 15 kV, 0.57 Torr at neon filling gas [63]

These fitted values of the model parameters are then used for the computation of all the discharges at pressures from 0.1 Torr to 2.1 Torr [63]. The results show that the Y_{sxr} increases with increasing pressure until the maximum value 0.42 J at 1.12 Torr (efficiency 0.015%, end axial speed V_a = 4.2 cm/μs, speed factor (SF) is 113.4 kA/cm per [Torr of neon]$^{1/2}$). After which it decreases with higher pressures. As expected as p_0 is increased, the end axial speed, the inward shock speed and the radial piston speed all reduced. The decrease in speeds lead to lowering of plasma temperatures below that needed for soft x-ray production (Table 3). Fig 6 presents the x-ray yield and temperature as functions of the pressure.

Table 3 Variation AECS PF-2 parameters with pressure at: L_0=280 nH, C_0= 25 μF, r_0= 25 mΩ, V_0= 15 kV, *RESF*=0.236, $c=b/a$=3.368, f_m=0.1, f_c=0.7, f_{mr}= 0.2, f_{cr}= 0.7, neon gas [63]

p_0 (Torr)	I_{peak} (kA)	I_{pinch} (kA)	V_a cm/μs	V_s cm/μs	V_p cm/μs	SF	Pinch duration	Ysxr (J)	Efficiency %
2.1	The code unable to run								
1.30	114.4	61.9	3.88	19.9	14.2	105.6	9.2	0.000	0
1.20	114.2	64.4	4.06	21.5	14.7	109.7	8.6	0.000	0
1.15	114.1	65.6	4.16	22.5	15.0	112.0	8.2	0.000	0
1.12	114.0	66.3	4.22	23.2	15.2	113.4	8.0	0.418	0.015
1.10	114.0	66.8	4.27	23.7	15.3	114.4	7.7	0.355	0.013
1.00	113.8	69.0	4.49	24.9	15.8	119.8	7.9	0.247	0.009
0.80	113.2	72.8	5.03	25.8	16.9	133.2	8.2	0.114	0.004
0.70	112.8	74.4	5.36	26.8	17.8	141.9	8.2	0.075	0.0026
0.57	112.2	75.9	5.87	28.7	19.6	156.4	7.9	0.039	0.0014
0.50	111.7	76.4	6.21	30.1	20.9	166.3	7.6	0.026	0.0009
0.40	111.0	76.5	6.80	32.8	23.4	184.7	7.0	0.013	0.0005
0.30	109.5	75.7	7.59	35.9	26.2	210.3	6.5	0.005	0.0002
0.20	105.6	73.2	8.78	41.7	30.0	248.5	5.7	0.001	0.000036
0.10	96.2	66.8	11.04	52.7	36.8	320.1	4.6	0.000	0

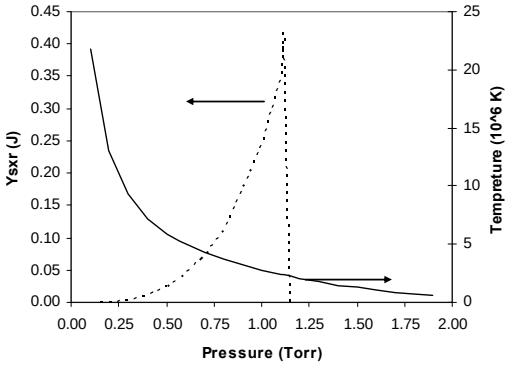

Fig. 6 The x-ray yield and temperature as functions of the pressure from neon AECS PF-2 [63]

It is evident from Table 3 that the peak value of total discharge current I_{peak} decreases with decreasing pressure. This is due to increasing dynamic resistance (rate of change of tube inductance, dL/dt that gives rise to a dynamic resistance equal to $0.5dL/dt$) due to increasing current sheath speed as pressure is decreased. On the contrary, the current I_{pinch} that flows through the pinched plasma column increases with decreasing pressure until it reaches the maximum. This is due to the shifting of the pinch time towards the time of peak current as the current sheet moves faster and faster. As the pressure is decreased, the increase in I_{pinch} may be expected to favour Y_{sxr}; however there is a competing effect that decreasing pressure reduces the number density. The interaction of these competing effects will decide on the actual yield versus pressure [49, 51]. The Lee model code was also applied to characterize the UNU/ICTP PFF Plasma Focus, finding a maximium argon soft x-ray yield (Y_{sxr}) of 0.039 J [63].

3.2 Soft x-ray yield vs electrode geometry

We next optimize Y_{sxr} from various plasma focus devices with different gases. More numerical experiments were carried out; varying p_0, z_0 and 'a' keeping $c=b/a$ constant. The pressure p_0 was slightly varied. The following procedure was used [46, 47, 49, 51, 52, 55]: At each p_0, the anode length z_0 was fixed at a certain value; then the anode radius 'a' was varied, till the maximum Y_{sxr} was obtained for this z_0. This was repeated for other values of z_0, until we found the optimum combination of z_0 and 'a' at the fixed p_0. Then we changed p_0 and repeated the above procedure; until finally we obtained the optimum combination of p_0, z_0 and 'a'.

The optimized results for each value of p_0 showed that as p_0 is increased, z_0 rises and 'a' decreases with each increase in p_0, while the soft x-ray yield slightly increases with increasing p_0 until it reaches a maximum value of 0.0035 J at p_0 = 1.8 Torr; then the Y_{sxr} decreases with further pressure increase [52]. Fig 7 shows x-ray yield and the optimum end axial speed as function of p_0, with the plasma focus operated at the optimum combination of z_0 and 'a' corresponding to each p_0. From the numerical experiments for AECS PF-2 with L_0 = 270 nH, C_0 = 25 μF, r_0 = 35 mΩ, V_0 = 15 kV we have thus found the optimum combination of p_0, z_0 and 'a' for argon Y_{sxr} as 1.8 Torr, 24.3 cm and 0.26 cm respectively, with the outer radius b = 0.9 cm. This combination gives Y_{sxr} = 0.0035 J. We also note that at this optimum configuration I_{peak} = 102 kA, I_{pinch} = 71 kA, and the end axial speed is of 11 cm/μs [52].

Practically it is technically difficult to change b; unless the whole electrode and input flange system is completely redesigned. So, for practical optimization, we wish to [49, 52, 63] keep b=3.2 cm and compute the optimum combinations of (p_0, 'a'), (p_0, z_0) and (p_0, z_0, 'a') for the

maximum Y_{sxr}. This gives us a practical optimum configuration of b = 3.2 cm, a = 1.567 cm, z_0 = 9 cm, giving a practical optimum yield of 0.924 J at 0.58 Torr for neon [63]. These numerical experiments confirmed that reducing c, down to certain limits, increases Y_{sxr} [49, 51, 52, 63].

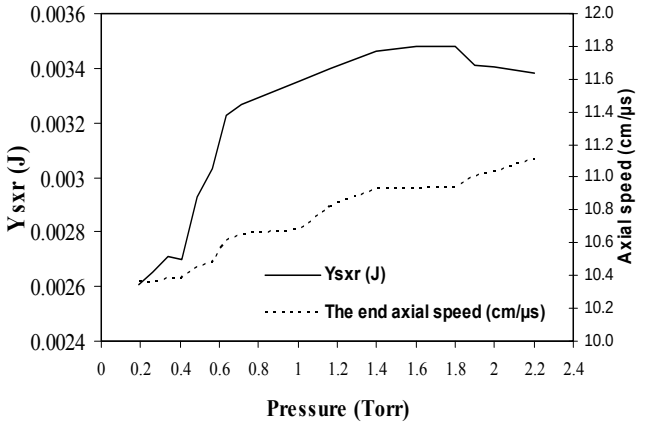

Fig. 7 Y_{sxr} and end axial speed of AECS PF-2 in Ar (Y_{sxr} vs p_0, z_0 and 'a') [52]

3.3 Soft x-ray yield vs inductance

We investigated the effect of reducing L_0 down to 3 nH[38, 39, 48, 49, 52, 63, 64] for different plasma focus devices operated with various gases. For example, it was found that reducing L_0 increases the total current from I_{peak}=115 kA at L_0=280 nH to I_{peak}=410 kA at L_0=15 nH for AECS PF-2 with neon gas [63] (see Table 4).

As L_0 was reduced, I_{peak} increased; 'a' is necessarily increased leading to longer pinch length (z_{max}), hence a bigger pinch inductance L_p. At the same time because of the reducing current drive time, z_0 needed to be reduced. The geometry moved from a long thin Mather-type to a shorter fatter one (see table 4). Thus whilst L_0 and axial section inductance L_a reduced, the pinch inductance L_p increased due to increased pinch length [38, 48, 63].

Table 4 For each L_0 the optimization combination of z_0 and 'a' were found and are listed here. Bank parameters: L_0 =280 nH, C_0 = 25 μF, r_0 = 25 mΩ; tube parameter: $c = b/a$ = 3.368; model parameters: f_m= 0.1, f_c = 0.7, f_{mr} = 0.2, f_{cr} = 0.7; operating at 2.8 Torr neon gas, V_0 = 15 kV

L_0 (nH)	z_0 (cm)	a (cm)	b (cm)	I_{peak} (kA)	I_{pinch} (kA)	a_{min} (cm)	Z_{max} (cm)	V_a (cm/μs)	Ysxr (J)
280	8.00	0.727	2.45	115	79	0.05	1.0	3.45	0.94
200	7.00	0.842	2.84	135	92	0.06	1.2	3.52	1.66
100	4.50	1.125	3.79	186	125	0.08	1.6	3.57	5.16
50	4.00	1.400	4.73	256	158	0.10	2.0	4.02	11.62
25	2.80	1.640	5.52	340	190	0.14	2.4	4.50	18.72
20	2.50	1.693	5.70	369	198	0.16	2.5	4.72	20.35
15	2.40	1.732	5.83	410	205	0.17	2.6	5.15	21.77
10	2.00	1.760	5.93	464	212	0.20	2.7	5.71	21.40
5	1.97	1.749	5.89	556	214	0.25	2.7	7.12	16.14
3	1.96	1.705	5.74	608	211	0.26	2.6	8.16	13.19

Whilst I_{peak} increases with each reduction in L_0 with no sign of any limitation, I_{pinch} reaches a maximum of 214 kA at L_0 = 5 nH, then it decreases with each reduction in L_0. This pinch current limitation effect is not a simple, but it is a combination of the two complex effects: the interplay of the various inductances involved in the plasma focus processes abetted by the increasing coupling of C_0 to the inductive energetic processes as L_0 is reduced [38, 52, 63].

From table 4 it can be seen, that as L_0 decreased, Y_{sxr} increases until it reaches a maximum value of 22 J at L_0 = 15 nH; beyond which Y_{sxr} does not increase with reducing L_0. This confirms the pinch current and Y_{sxr} limitation effect in neon plasma focus. Figure 8 represents I_{pinch} and x-ray limitation effects in neon plasma focus at 2.8 Torr as L_0 is reduced from 280 nH to 3 nH.

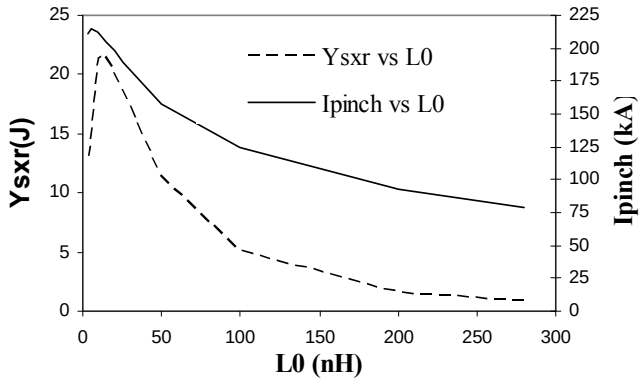

Fig. 8 The x-ray yield and I_{pinch} (computed) vs L_0 (280 nH to 3 nH) at 15 kV, 2.8 Torr of Neon [63]

Based on the results of these numerical experiments on various devices with different gases, to improve Y_{sxr}, L_0 should be reduced to a value around 10-25 nH, which is an achievable range incorporating low inductance technology, below which I_{pinch} and Y_{sxr} would not be improved much, if at all. These experiments confirm the pinch current limitation effect, and consequently the soft x-ray yield for the plasma focus.

3.4 Scaling laws for soft x-ray yield of argon and nitrogen plasma focus

Following above stated procedures numerical experiments were investigated on AECS PF-2 like argon plasma focus at different operational gas pressures (0.41, 0.75, 1, 1.5, 2.5 and 3 Torr) for two different static inductance values L_0 (270 nH and 10 nH) and then after systematically carrying out more than 3000 shots, the optimized conditions are obtained. Table 4 shows optimized configuration found for each E_0 for 10 nH at gas pressure of 1 Torr. From this data, we also plot Y_{sxr} against E_0 as shown in figure 9 to obtain scaling law: $Y_{sxr}=0.05E_0^{0.94}$ in the 1 to 100 kJ regions. The scaling deteriorates as E_0 is increased to $Y_{sxr}=0.32E_0^{0.52}$, and then to $Y_{sxr}=1.01E_0^{0.33}$ Y_{sxr} at high energies towards 1MJ. We then plot Y_{sxr} against I_{peak} and I_{pinch} and obtain Fig 10 which shows $Y_{sxr}=7\text{x}10^{-13}I_{pinch}^{4.94}$ and $Y_{sxr}=2\text{x}10^{-15}I_{peak}^{5.47}$ [53]. We also conclude that the I_{pinch} scaling is the more universal and robust one [53].

Table 4 Optimized configuration found for each E_0; $RESF$=0.337, c=3.368, L_0=10 nH and V_0=15 kV and f_m, f_c, f_{mr}, f_{cr} are fixed at 0.05, 0.7, 0.15 and 0.7 respectively, v_a is the peak axial speed at 1 Torr.

E_0 (kJ)	C_0 (μF)	a (cm)	z_0 (cm)	I_{peak} (kA)	I_{pinch} (kA)	v_a (cm/μs)	Y_{sxr} (J)	Efficiency (%)
1.1	10	0.70	4	251.4	148.8	13.60	0.05	0.0045
2.8	25	0.90	6	329.5	193.1	13.98	0.13	0.0046
4.5	40	1.01	8	370.7	217.1	14.08	0.22	0.0048
5.6	50	1.07	9	390.4	229.0	14.08	0.26	0.0046
11.3	100	1.24	15	448.8	264.3	14.03	0.52	0.0046
22.5	200	1.41	23	503.5	300.1	13.79	1.01	0.0045
45.0	400	1.58	37	551.9	333.6	13.46	1.85	0.0041
67.5	600	1.68	43	578.3	354.5	13.30	2.52	0.0037
90.0	800	1.74	57	594.5	366.1	13.11	3.15	0.0035
112.5	1000	1.80	61	607.3	377.2	13.03	3.72	0.0033
450.0	4000	2.07	133	669.8	432.4	12.48	7.67	0.002
900.0	8000	2.18	177	692.4	454.9	12.30	9.66	0.001
1012.5	9000	2.20	209	695.7	457.8	12.24	10.03	0.0001

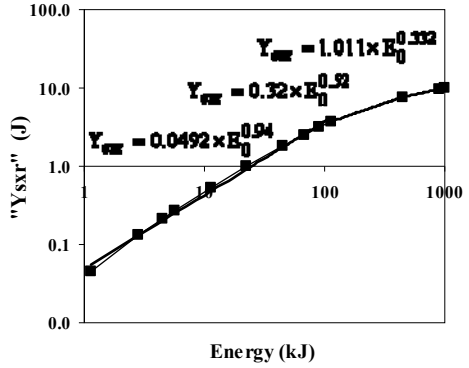

Fig. 9 Y_{sxr} vs E_0. The parameters kept constants are: *RESF*=0.337, c=3.368, L_0=10nH, p_0 = 1 Torr and V_0=15 kV and model parameters f_m, f_c, f_{mr}, f_{cr} at 0.05, 0.7, 0.15 and 0.7 respectively [53].

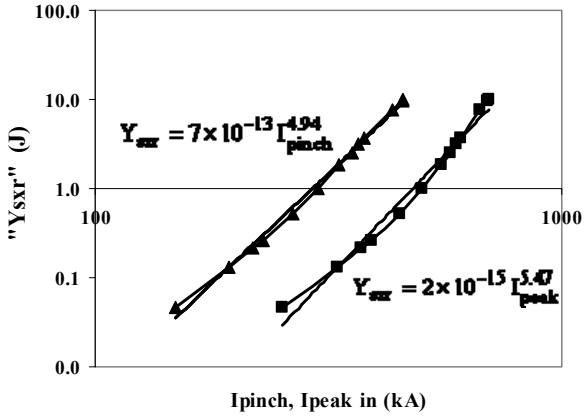

Fig. 10 Y_{sxr} vs I_{pinch}, I_{peak}. The parameters kept constants are: *RESF*=0.337, c=3.368, L_0= 10nH, p_0 = 1 Torr and V_0=15 kV and model parameters f_m, f_c, f_{mr}, f_{cr} at 0.05, 0.7, 0.15 and 0.7 respectively [53].

Scaling laws for nitrogen [65] and neon soft x-ray yields [14, 36], in terms of storage energies E_0, were found to be best averaged as $Y_{sxrN}=1.93E_0^{1.21}$ and $Y_{sxrNe}=11E_0^{1.2}$ (yield in J, E_0 in kJ), respectively at energies in the 2 to 400 kJ regions. By comparing our recent results for nitrogen plasma focus with argon and neon soft x-ray yields over this studied storage energy ranges, it is seen that the neon soft x-ray yield of plasma focus is the most intense one (Fig. 11). So considering all these numerical experiments, we find that the plasma focus is a powerful source of X-rays with wavelengths which may be suitably selected for microlithography, micromachining and microscopy simply by selecting the working gas (Neon or Argon or Nitrogen correspondingly) and choosing corresponding design and operating parameters of the device.

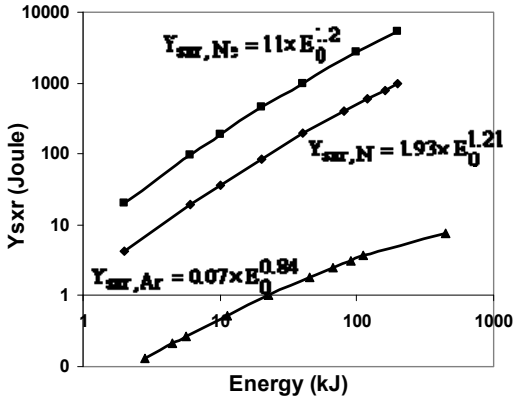

Fig. 11 Soft x-ray yields versus storage energy for neon, nitrogen and argon plasma focus [65]

3.5 Model Parameters versus Gas Pressure in Two Different Plasma Focus Devices Operated in Argon and Neon

Using Lee model code, the computed and measured currents are fitted for varying pressure, with the purpose to find the proper model parameters versus pressure for AECS PF-2 and INTI PF devices operated with argon and neon, respectively. For these two devices, we obtained a good fit of all features from the start to the end of the axial phase. The results show a value of $f_m = 0.05 \pm 0.01$ (± 20%) over the whole range of pressure 0.2–1.2 Torr in Ar; and $f_m = 0.04 \pm 0.01$ (± 25%) over 0.7–4.1 Torr in Ne. The value of $f_c = 0.7$ was fitted for all cases. Combining these results with those published for several other small machines, it would appear that, where measured current waveforms are not available for example in designing new machines, a good compromise would be to take a guideline value of $f_m = 0.05$ and $f_c = 0.7$ for both argon and neon. We have designed another current measurement system based on numerically integrating a *dI/dt* waveform measured with a Rogowski coil of a few turns. This will allow measurements to be made of the radial phase model parameters [55].

3.6 Radiative Collapse in Plasma Focus Operated with Heavy Noble Gases

Numerical experiments have been investigated on plasma focus device parameters to study radiative collapse phenomena. For this purpose, several numerical experiments have been carried out with different gases. To start the numerical experiments we configure the Lee model code (version RADPF5.15K) to operate as the plasma focus device and then the fitting procedures of the experimental and numerical current traces reported in the recent publication

[55] have been used. To obtain a reasonably good fit for different gases the tabulated parameters are used (see table 5).

Table 5 Parameters of interested plasma focus devices: L_0, C_0, r_0 are Inductance, Capacitance, and resistance of the Capacitor bank respectively; V_0–tube voltage, Axial phase: f_m (mass swept up factor), f_c(plasma current factor); Radial phase: f_{mr} (mass swept up factor), f_{cr} (plasma current factor).

Device (ref.)	**L_0 (nH)**	**C_0 (μF)**	**r_0 (mΩ)**	**V_0 (kV)**	**gas**	**f_m**	**f_c**	**f_{mr}**	**f_{cr}**
ICTP PFF [64]	110	30	12	13.5	Argon	0.044	0.7	0.1	0.85
AECS PF-2 [52]	270	25	35	15	Argon	0.05	0.7	0.15	0.7
AECS PF-2 [63]	280	25	25	15	Neon	0.1	0.7	0.2	0.7
AECS PF-1[46]	1600	25	80	15	Nitrogen	0.1	0.7	0.15	0.7

Fig 12 shows variations of radial trajectories versus pressures on AECS PF-2 device. For AECS PF-2, at 0.1 Torr the radial inward shock wave starts at 9.5 mm and is driven to the axis after 50 ns with the driving magnetic piston trailing it by some 1.1 mm as the shock front hits the axis. A reflected shock (RS) goes outwards and after some 8 ns hits the incoming piston. At this time the pinch starts and the column compresses inwards a little, as is typical computed data indicates that even in this shot the radiation power emitted (mostly line) already exceeds the Joule heating power with the pinch temperature in this shot reaching 300 keV. This means that there is already net power loss (or radiation cooling) but the radiation cooling is insufficient to perceptibly affect the dynamics at the pinching power provided by the available pinch current at that time. At 0.85 Torr and a pinch temperature of 190 eV with a pinch current of just under 66 kA, radiative collapse is obvious with the radius collapsing in a few ns to the cut-off radius of 0.1mm set in the model. At 1 Torr with a pinch temperature of 154 eV, the collapse does not reach the cut-off radius. In this case the model maintains a small radius (0.2 mm) pinch for about 5 ns. These are the conditions (high density, relatively long pinch duration 12.2 ns) which produce huge line yields of more than 22.5 J. At 1.2 Torr and pinch temperature of 130 eV with a pinch current of just 57 kA, the speeds are much slower now and the pinch occurs late so the current has dropped considerably reducing the pinching force; the radiative collapsed radius is now bigger (0.3 mm). Finally at 1.7–2 Torr, the column blows out instead of pinching in as the RS hits the piston.

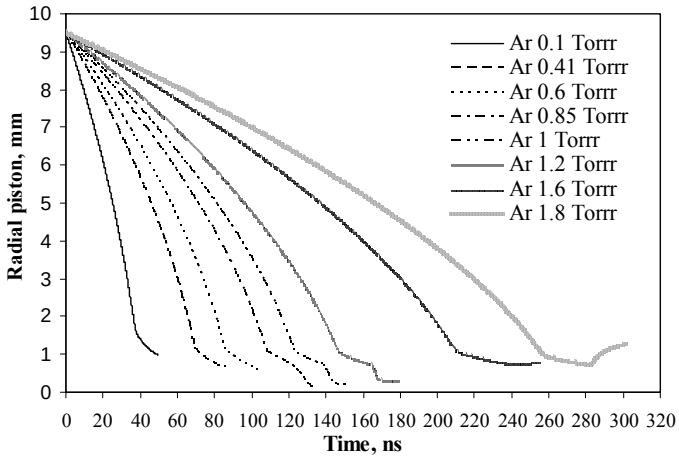

Fig. 12 Variations of radial piston trajectories on AECS PF-2 versus argon pressure [66]

From these numerical experiments, it is noticed that tube voltage has a high maximum value of 100 kV, corresponding to a maximum value of ion density about 60×10^{23} m^{-3} at 0.85 Torr for plasma focus operated with Argon gas, and even higher tube voltages for Krypton and Xenon plasma focus. In addition to that, many sets of numerical experiments using Lee model code on parameters of different plasma focus devices (NX2 [14], PF1000 [37]) were carried out. Radiative collapse phenomena have also been observed at higher pressure with heavy noble gases. From numerical experiments with neon, oxygen and nitrogen plasma focus, it can be said that no radiative collapse phenomena has been noticed under a wide pressure range. Finally, based on obtained results by 5-phase Lee model code, we can say that type and pressure of the plasma focus play an important role in radiative collapse creation. This phenomenon produces an extreme increase in tube voltage and generates huge line radiations in the plasma focus [66].

4. Conclusions

The Lee model code has been adapted to gases of special interest to us namely nitrogen and oxygen and applied the numerical experiments specifically to our AECS PF-1 and AECS PF-2. Numerical experiments have been generalised to other machines and other gases in order to look at scaling and scaling laws and to explore recently uncovered insights and concepts. The required thermodynamic data of nitrogen, oxygen, neon and argon gases at different temperatures were calculated, the x-ray emission properties of plasmas were studied and suitable temperature range (window) for generating H-like and He-like ions.

The Lee model code version RADPF5.15K is used to characterize the AECS-PF-1 and AECS-PF-2, and for optimizing the nitrogen, oxygen, neon and argon SXR yields. Numerical experiments have been carried out to optimize each device. In each case we found optimum set of parameters that increased the SXR yield of our plasma focus several-fold from its present typical operation; without changing the capacitor bank, merely by changing the electrode parameters and the operating pressure. We also carried out practical optimization in which cathode radius b is kept constant.

Numerical experiments show the big influence of L_0 for improving the soft x-ray yield; that it is useful to reduce L_0 to a range of 10–25 nH; but not any smaller since further reduction produces no yield benefit and would be a futile expensive exercise. For our machines, reduction of L_0 would give the optimum soft x-ray yields from N_2, O_2, Ne and Ar of 6 J, 10 J, 22 J, and 0.1 J respectively. These yields at diverse wavelength ranges are large enough to be of interest for

applications ranging from microelectronics lithography to micro-machining and microscopy of biological specimens.

Scaling laws for SXR of argon and nitrogen plasma focus, in terms of energy, peak discharge current and focus pinch current were found. For the plasma focus device AECS PF-2 operated in Ar and INTI PF in Ne, model parameters of mass and current in the axial phase of plasma focus were found by matching the measured and calculated current waveforms over a range of pressures. The results showed a good compromise would be to take a guideline value of f_m=0.05 and f_c=0.7 for both Argon and Neon. Together with IPFS and INTI IU we have planned another experiment to independently test the value of f_c. These are crucial experiments as the Lee model code depends on reliable values of these model parameters particularly for designing new machines when there is no measured current trace to fit model parameters.

Numerical experiments were carried out on different plasma focus devices with different filling gases to show that radiation cooling and radiative collapse may be observed for heavy noble gases (Ar, Kr, Xe) for pinch currents even below 100 kA. The results show that the line radiation emission and tube voltages have huge values near the radiative collapse regime. The creation of the consequential extreme conditions of density and pulsed power is of interest for research and applications.

Acknowledgments

The authors would like to thank Director General of AECS, for encouragement and permanent support. The authors would also like to express thanks to Mrs. Sheren Ismael and Mr. Suleiman Shaban, who collaborated going through all the numerical experiments using Lee model code and experiments on AECS PF2, respectively.

References

1. J S Pearlman and J C Roirdan, J. Vac. Sci. Technol. **19,** 1190, (1981)
2. R Feder, J S Pearlman, J C Riordan and L J Costa, J. Microsc. **135,** 347, (1984)
3. B. Niemann et. al., Optik **84,** 35, (1989)
4. J L Porter et. al., Phys. Rev. Lett. **68,** 796, (1992)
5. J J Rocca et. al., Phys. Rev. Lett. **73,** 2192, (1994)
6. V L Kantsyrev et. al., Proc. 3rd Int. Conf. on Dense Z-pinches (London, UK) vol 299, ed M Haines and A Knight (New York: AIP) p 226, (1993)
7. D A Hammer et. al., Appl. Phys. Lett. **57,** 2083, (1990)
8. A Ikhlef et. al., Proc. 3rd Int. Conf. on Dense Z-pinches (London, UK) vol 299, ed M Haines and A Knight (New York: AIP) p 218, (1993)
9. C S Wong and S Lee, Rev. Sci. Instrum. **55,** 1125, (1984)
10. J W Mather, Phys. Fluids **8,** 366, (1965)
11. M Zakaullah et. al., Phys. Plasmas **6,** 3188, (1999)
12. M Zakaullah et. al. Appl. Phys. Lett. **78,** 877, (2001)
13. S Lee et. al., IEEE Trans. Plasma Sci. **26,** 1119, (1998)
14. S. Lee, et al., Plasma Phys. Control. Fusion, **51,** 105013 (2009)
15. M. Zakullah et. al., Plasma Sources Sci. Technol. **11,** 377 (2002)
16. H. Bhuyan et. al., J. Appl. Phys. **95,** 2975 (2004)
17. F. N. Beg et. al., J. Appl. Phys. **88,** 3225 (2000)
18. M. Zakaullah et. al., IEEE Trans. Plasma Sci., **30**, 6, 2089, (2002)
19. M Zakaullah et. al., Plasma Sources Sci. Technol. **9**, 592–596 (2000)
20. D. Wong et. al., IEEE Trans. Plasma Sci., **32**, 6, (2004)
21. V. A. Gribkov et. al., IEEE Trans. Plasma Sci., **30**, 3, (2002)
22. M. Shafiq, et al., Modern Physics Letters B, 16, 9, 309 (2002).
23. M. Shafiq, et al., Journal of Fusion Energy, 20, 3, 113, September 2001 (q 2002).
24. N. K. Neog, et al., Journal of Applied Physics, 99, 013302 (2006).

25. A. Roomi et. al., Jounal of Fusion Energy, DOI 10.1007/s10894-011-9395-2, (2011)
26. M. A. I. Elgarhy, M. Sc. Thesis, Plasma Focus and its Applications, Cairo (2010).
27. R. Lebert, D. Rothweiler, A. Engel, K. Bergmann, W. Neff, Optical and Quantum Electronics, **28**, 241-259 (1996)
28. F. Richer, et al., Dense z-pinches. Second International Conference (1989), New York/N.Y.: AIP, (AIP Conference Proceedings 195) (1989).
29. R. Lebert, A. Engel and W. Neff , J of Applied Physics, 78, 11, 6414-6420, (1995)
30. L. Rico, B.J. Gomez, J.N. Feugeas, O.de Sanctis, Appl. Surf. Sci. 254, 193–196 (2007)
31. L. Rico, B.J. Gomez, M. Stachoitti, N. Pellegri, J.N. Feugeas, O.de Sanctis, Braz. J. Phys. 36(3), 1009–1012 (2006)
32. Institute for Plasma Focus Studies http://www.plasmafocus.net
33. Internet Workshop on Plasma Focus Numerical Experiments (IPFS-IBC1), 14 April–19 May (2008)
34. S. Lee, "Radiative Dense Plasma Focus Computation Package: RADPF", http://www.intimal.edu.my/school/fas/UFLF/ . http://www.plasmafocus.net/IPFS/modelpackage/File1RADPF.htm, (2011)
35. S. Lee et. al., J. Appl. Phys. **106,** 023309 (2009)
36. S. H. Saw, S. Lee, Energy and Power Engineering, **2** (1), 65-72 (2010)
37. S. Lee et. al., Appl. Phys. Lett., **92,** 111501 (2008)
38. S. Lee et. al., Appl. Phys. Lett., **92,** 021503 (2008)
39. S. Lee et. al., Plasma Phys. Control. Fusion, **50,** 065012 (2008)
40. K. N. Koshelev, V. I. Krauz, N. G. Reshetniak, R. G. Salukvadze, Yu. V. Sidelnikov, E. Yu. Khautiev. J. Phys. D: Appl. Phys. **21** 1827 (1988).
41. S. Lee, S. H. Saw and Jalil Ali, Journal of Fusion Energy DOI: 10.1007/s10894-012-9522- 8 (2012)
42. S. Lee and S. H. Saw. "Multi-radiation modelling of the plasma focus", 5th International conf. on fronties of plasma physics and technology, 18-22 April 2011, Singapore.
43. Z. Ali, S. Lee, F.D. Ismail, Saktioto, J. Ali and P.P. Yupapin. Physics Procedia **8**, 393 – 400 (2011).
44. S. Bing, "Plasma dynamics and x-ray emission of the plasma focus", PhD Thesis NIE ICTP Open Access Archive: http://eprints.ictp.it/99/, (2000)
45. M. H. Liu, "Soft X-Ray from Compact Plasma Focus". PhD Thesis, School of Science, Nanyang Technological University, December (1996)
46. M. Akel, Sh. Al-Hawat, S. Lee, Journal of Fusion Energy, **28**, 4, 355-363 (2009)
47. M. Akel et. al., Journal of Fusion Energy, **29**, 3, 223-231 (2010)
48. M. Akel, Sh. Al-Hawat, S. Lee, J. of Fusion Energy, **29**, 1, 94 (2010)
49. M. Akel, Sh. Al-Hawat, S. Lee, Journal of Fusion Energy, **30**, 1, 39 - 47 (2011)
50. M. H. Liu et. al., IEEE Trans. Plasma Sci., **26,** 135–40 (1998)
51. S. H. Saw, et al., IEEE Trans. Plasma Sci., **37**, NO. 7, 1276-1282 (2009)
52. M. Akel and S. Lee, Journal of Fusion Energy, **31**, 2, 122 – 129, (2012)
53. M. Akel and S. Lee, Journal of Fusion Energy, **31**, 2, 143 – 150, (2012)
54. Sh. Al-Hawat, M. Akel, C. S. Wong, Journal of Fusion Energy, **30**, 6, 503 – 508, (2011)
55. Sh. Al-Hawat, M. Akel, S H Saw, S Lee, Journal of Fusion Energy, **31**, 1, 3 – 20, (2012)
56. Sh. Al-Hawat. IEEE Transactions on Plasma Science, **32**, 2, 764-769 (2004).
57. Sh. Al-Hawat, et. al., Vacuum, **84**, 907–912 (2010).
58. M. Habibi et. al., J Fusion Energ, DOI 10.1007/s10894-008-9159- 9, (2008)
59. R A Behbahani et. al., Plasma Phys. Control. Fusion **52**, 095004 (2010)
60. M. Zakaullah et. al., Journal of Fusion Energy, **19** (2), June 2000 (q 2002)
61. N. D. Farahani et. al., Jounal of Fusion Energy, DOI 10.1007/s10894-011-9409-0, (2011)
62. Z. Shahbazi rad et. al., Jounal of Fusion Energy, DOI 10.1007/s10894-011-9405-4, (2011)
63. Sh. Al-Hawat, M. Akel, S Lee, Journal of Fusion Energy, **30**, 6, 494 – 502 (2011)
64. M. Akel, Journal of Fusion Energy, DOI 10.1007/s10894-011-9499-8
65. M. Akel and S. Lee, "Scaling Laws of Nitrogen Soft X-Ray yields from 1 – 200 kJ Plasma Focus", manuscript submitted for publication in Journal of Fusion Energy (2012).
66. M. Akel and S. Lee, "Radiative Collapse in Plasma Focus Operated with Heavy Noble Gases", manuscript submitted for publication in Journal of Fusion Energy (2012).

Notes

Notes

Notes

Institute for Plasma Focus Studies

IPFS *Melbourne KL Singapore*

IPFS Conference

Bangkok 30 March to 1 April 2012

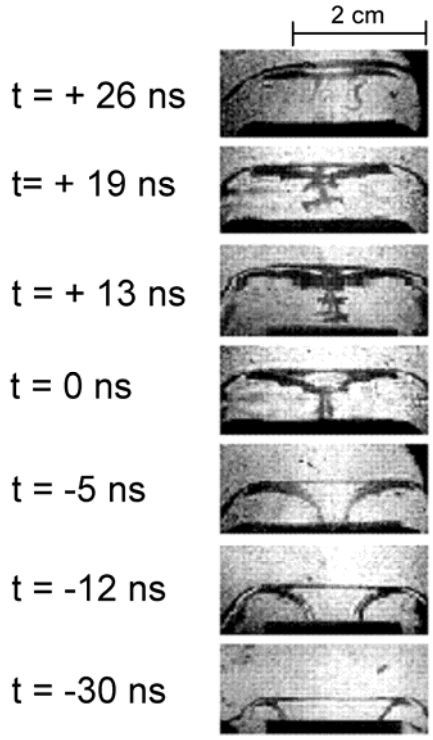

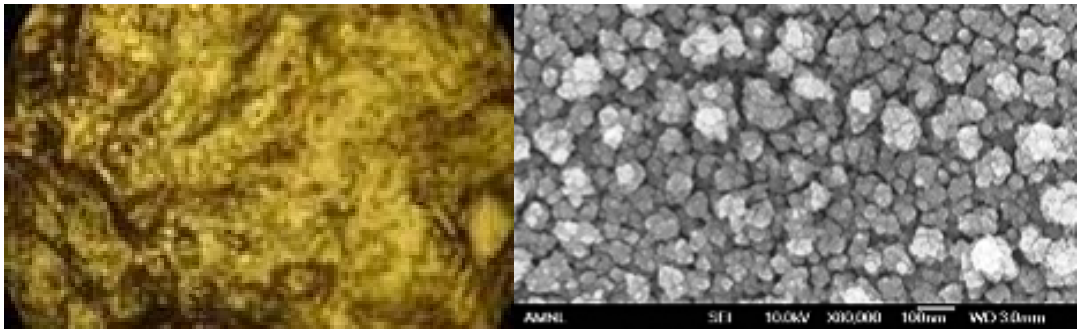

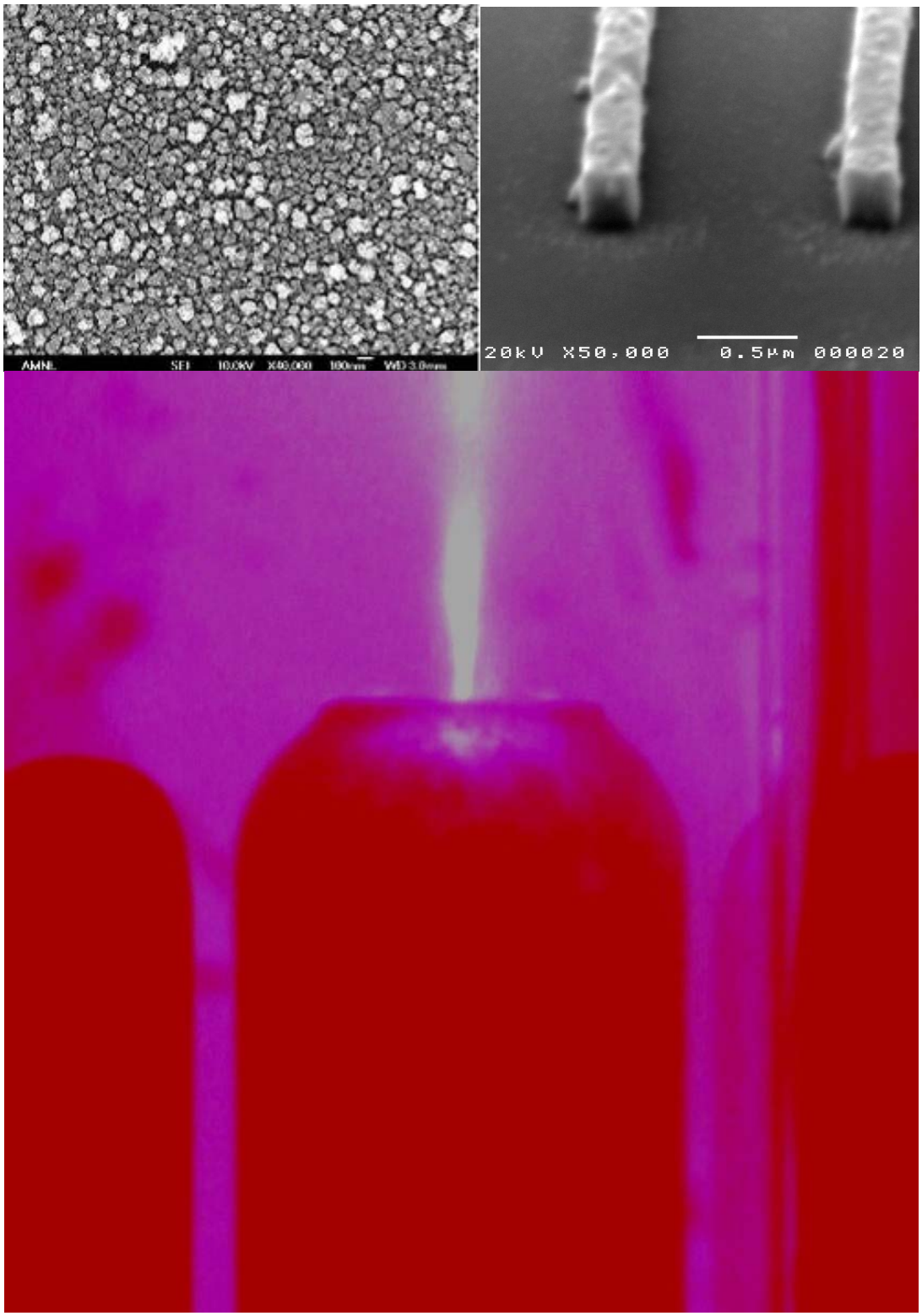
20kV X50,000 0.5µm 000020